APERTURE SYNTHESIS OBSERVATIONS OF NEUTRAL HYDROGEN IN THREE GALAXIES

Thesis by

Gerson Seth Shostak

In Partial Fulfillment of the Requirements
For the Degree of
Doctor of Philosophy

California Institute of Technology
Pasadena, California
1972
(Submitted December 6, 1971)

ACKNOWLEDGEMENTS

Customarily, by the time one has arrived at the point of writing the acknowledgements for a thesis, the concomitant euphoria manifests itself in an effusive orgy of thanks to virtually every acquaintance of the author. Departing somewhat from this brotherly gesture, I shall attempt to limit myself to no more than half the Astronomy Department, although I am indebted to practically all its members.

I first wish to thank G. J. Stanley, Observatory Director. His generous provision of telescope and computer time allowed completion of a thesis currently holding the record for required observing days.

My deepest appreciation goes to A. T. Moffet for his meticulous reading of the text, and to M. Schmidt for many helpful discussions and suggestions.

Much of what one learns, or finds out he does not know, occurs in the company of fellow grad students. The following gentlemen have been particularly helpful: Eric Greisen, Robert O'Connell, Valdar Oinas, Richard Sramek, Kurt Weiler, and Ka Bing Yip.

Post-doctoral fellows are men-of-learning still sympathetic to the ignorant student. I have profited greatly from talks with Steve Gottesman, Ellen Hardebeck, and Leonid Weliachew.

Gustav Tammann gave generously of his time in helping me learn about the distances to galaxies.

Finally, my deepest gratitude and personal thanks go to Dave Rogstad, the man who started me on this project and patiently taught me about interferometers.

This thesis is dedicated to NGC2403 and all its inhabitants, to whom copies will be furnished at cost.

ABSTRACT

Aperture synthesis techniques have been used to study the three galaxies NGC2403 (Scd), NGC4236 (SBdm), and IC10 (Irr) in the 21-cm line of neutral hydrogen and off-line continuum. Spatial resolution was 2 minutes of arc; velocity resolution was 21 km-s^{-1}. The data yield information on the distribution of the HI, and its associated velocity field.

Hydrogen extent of the objects agrees well with their optical size, and evidences a lumpy structure. HI peaks occur away from the nuclei for NGC2403 and NGC4236, and are suggestive of a ring structure for the former galaxy. The hydrogen distribution of IC10 is similar in appearance to that of the Small Magellanic Cloud. In all objects HI peaks show good positional agreement with major HII regions.

Velocity fields are derived for all objects, and rotation curves obtained for NGC2403 and NGC4236. These curves evidence differential rotation but do not include Keplerian tails, implying that the mass distributions are considerably extended and the total masses poorly determined. The velocity field of IC10 suggests rotation.

Non-circular motions of ~10 km-s^{-1} are seen in NGC2403, and these agree well with the streaming motions predicted by the density-wave theory of spiral structure.

A comparison of NGC2403 with the late-type spirals M33 and M101 reveals a progressive deepening of the central HI depression with increasing mass. Rotation curves for these three galaxies are similar, and consequently all are expected to have mass-to-light ratios which increase rapidly with radius. All have similar maximum HI surface densities ($\sim 10^{21}$ atoms-cm^{-2}) and observed fractional hydrogen masses (~9%).

TABLE OF CONTENTS

INTRODUCTION

Neutral hydrogen studies of external galaxies provide fundamental information on the distribution of gas and the nature of the velocity field in such objects. Because of the observational mixing of these quantities, they cannot be separately determined for our own Galaxy, and this fact is a principal impetus for the external studies.

Velocity information obtained from 21-cm work is complemented by considerable optical data (for a review of the relevant literature, see Burbidge and Burbidge 1971). Rotation curves have been determined by observation of the Doppler shift of various emission or stellar absorption lines. Recently, use of a Fabry-Perot interferometer (Courtes 1960) has allowed relatively high velocity resolution in studies of extragalactic HII regions. However, these measures are generally confined to the central regions of the galaxy, and a substantial amount of data is required to average out peculiar motions. Detailed HI studies provide a better picture of galactic rotation if sufficient spatial resolution can be obtained.

Until recently, only relatively large beamwidths ($\geq$ 10 arcmin) were available for 21-cm studies. Consequently investigations were confined to integral properties such as HI mass and spectral shape (see Epstein 1964), or to the very nearby objects such as M31 and the Magellanic Clouds. The use of interferometric techniques for synthesizing small beams, coupled with improved receiver sensitivity, allows rather detailed two-dimensional study of a larger range of objects. The present work covers the use of a 2 arcmin synthesized beam for studying the three galaxies NGC2403, NGC4236, and IC10. Velocity resolution was 21 km-s^{-1}. We address ourselves principally to the following questions:

--- What is the distribution of HI in the galactic disks, and how is it correlated in position and density with other material.

--- What is the shape of the rotation curve, particularly in the generally inaccessible outer regions, and what is the implied total mass distribution.

--- How important are deviations from the general rotation law, and to what extent are they in agreement with theories of spiral structure.

Additionally we obtain several integral properties which are useful in statistical studies of galaxies.

NGC2403 is a late Sc spiral according to the Hubble classification and is very similar to M33 (Sandage 1961). It belongs to the M81 group, as does NGC4236 below. Because of its importance in the fixing of the galactic distance scale, NGC2403's cepheid content has been studied in detail (Tammann and Sandage 1968). The distance given by these authors is 3.25 Mpc. A large angular size (29 arcmin) and favorable inclination (60°) encouraged early HI studies; the first reported detection was with the Harvard 60-foot telescope (Cooper *et al*. 1960). These latter data were extended and reported by Roberts (1962a) in the form of a 21-cm spectrum. Included were estimates of the HI and total mass. Roberts (1967) later claimed that the hydrogen distribution in NGC2403 had a central depression, and rose to a maximum at 9 arcmin radius. This was similar to the well-established "ring" distribution of M31 (Burke *et al*. 1964; Roberts 1966a; Brundage and Kraus 1966; Gottesman *et al*. 1966). However the relative resolution for NGC2403 was much poorer, and the existence of a central depression was soon disputed by Guelin and Weliachew (1969) in their fan-beam study. They argued in favor of a Gaussian HI distribution. A recent re-analysis of Roberts' 300-foot data by Burns and Roberts (1971) suggested that a central deficiency in the HI surface density, if it existed at all, was slight. The present high resolution study is consistent with most of these previous investigations. The HI surface density is seen to be relatively flat over the central 8-10' (diameter), thereafter dropping slowly with radius (Chapter 5). At 4' radius, several strong concentrations appear, which if seen with lower resolution might give the appearance of a ring.

The overall hydrogen extent is coincident with the optical object.

An early attempt to determine a rotation curve for NGC2403 was based on a single-spacing interferometer measurement (Seielstad and Whiteoak 1965; also see Rogstad, Rougoor, and Whiteoak 1967). Due to complications induced by the unknown HI distribution, this curve was subject to considerable interpretive variation. Model analysis was used to fit rotation laws of the Brandt (1960) form to this data, and subsequently to that of Guelin and Weliachew and Burns and Roberts. These analyses generally assumed axisymmetric rotation laws and HI distributions. In Chapter 6 we derive a two-dimensional radial velocity map which shows a great deal of symmetry. The resultant rotation curve rises sharply near the center, in good agreement with the HII data of Deharveng and Pellet (1970), and then flattens out. The maximum rotational velocity, 127 km-s^{-1}, fixes the observed mass of NGC2403 at about twice that of M33. Peculiar (non-circular) motions occuring at the location of some of the spiral arms are in accord with the predictions of the density-wave theory of spiral structure.

An extended continuum source of low intensity is shown in Chapter 4.

NGC4236 is a highly inclined (75°) spiral which has been frequently classified Sc (Hubble 1926; Shapley and Ames 1932). Baade (1931) was the first to suggest that it might in fact be barred. The Reference Catalogue (1964) lists the galaxy as SBdm on the basis of a 200-inch photograph; we adopt this classification for the present work. The structure of the galaxy is rendered uncertain by reason of the high inclination, low luminosity (m_{pg}=10), and the orientation of the bar very nearly in the sky plane. For these same reasons, NGC4236 has received little study, particularly at optical wavelengths. However the practically edge-on aspect enhances its apparent 21-cm surface brightness to values similar to those found in NGC2403. An early claim to detection was made by Volders and Van de Hulst (1959), and an HI mass of $\geq 10^9$ $M_\odot$ was estimated. The only other published observations are included in the single-spacing interferometric survey of Rogstad et al. (1967). A radial velocity range of ~ 200 km-s^{-1} centered* near 0 km-s^{-1} was found. Due to the high inclination, the phases plotted against radial velocity provided a rotation curve in the central regions which agrees moderately well with that found here (Chapter 6). Over the region of the bar, rotation is that of a solid body; outside this region a turnover in the rotation curve occurs.

---

*Radial velocities are always given with respect to the sun.

The hydrogen distribution peaks at the ends of the bar in regions containing considerable HII emission (Chapter 5). The bar itself has a high (20%) fractional hydrogen content. The constraint of the HI to the disk of NGC4236 allows an upper limit of 8 x 10^{19} cm^{-2} to be placed on the halo surface density at an average z-distance of 3.5 kpc.

A small, essentially unresolved, continuum source is also seen (Chapter 4). The distance to NGC4236 is assumed to be the same as to NGC2403 (Tammann, private communication).

IC10 appears as a small (4' x 5') nebulosity at a Galactic latitude of 3°. It was shown to be extragalactic by Mayall (1937) who, recognizing the probable presence of obscuration, speculated that what was seen was merely a portion of a spiral. This suggestion was reiterated by Hubble (1936) and Mayall himself (1941) when the latter published spectroscopic measurements establishing a systemic velocity of ~ -400 $km\text{-}s^{-1}$. Without further evidence to support the spiral hypothesis, investigators tentatively classified IC10 as Irr. Once again using the Harvard telescope, Roberts (1962b) obtained a Gaussian-shaped 21-cm line profile whose centroid agreed within observational error with IC10's optical position. Although these data strengthened the Irr classification, they could not be considered conclusive, particularly in view of the large beamwidth (53') employed.

The present study reveals an integrated hydrogen distribution (Chapter 4) very similar to that of the Small Magellanic Cloud (Hindman 1967). Three major concentrations are evident, the principal peak coinciding with the brightest optical condensation and an 8°K continuum source. The hydrogen distribution has a generally elliptical boundary. At one point the HI surface density drops to zero in a region of optical emission. The cause of this "hole" is not certain, but it is taken as evidence that IC10, despite its convincingly Irr appearance, is a flattened system. The distance to IC10 is taken to be 3.0 Mpc (Tammann, private communication).

Rotation of this object was established by Rogstad et al. Unfortunately the narrow line profile (~ 100 km-s^{-1}) allows only a coarse definition of the radial velocity field with the present filter widths. The gradient of this field (Chapter 6) is in reasonably good positional agreement with the apparent HI major axis, thereby strengthening the belief that IC10 is, at least to first approximation, a rotating disk.

HI and total mass estimates were made for all the above objects. These, and other integral properties, are summarized in Chapter 7.

An extensive description of the synthesis technique is given in Chapters 1, 2, 3 and the Appendix.

I. APERTURE SYNTHESIS

1. The Interferometer

The Owens Valley interferometer consists of two 90-foot-diameter antennas with superhetrodyne receivers. The receivers share a common local oscillator and feed a multiplier output. The response of this system to a point source is described by Read (1963) using a straightforward analysis in the time domain. However, since the interferometer is virtually by definition a correlator, it is more general and hopefully more lucid to describe its operation by considering the correlation of two signals. Such a treatment is given in the Appendix. It is shown (equation A.20) that the single sideband response may be written

$$R(\tau_1,\tau_2) = GA(\tau_1+\tau_2)\cos\left[(\omega_{LO}+\omega_{IF})\tau_1+\omega_{IF}\,\tau_2\right] \qquad (1.1)$$

where τ_1 and τ_2 are differential delays respectively before and after the mixer in the two branches of the interferometer. $A(\tau_1+\tau_2)$ is the Fourier transform of the product of the source power spectrum and IF bandpass. G is the system gain. The principal time dependence is contained in

$$\tau_1 = \frac{d}{c}\sin\theta + \text{constant.}$$

In this expression θ is the angle between the source position vector and a plane perpendicular to the interferometer baseline. The length of the baseline is d. Since $A(\tau_1+\tau_2)$ is maximized for $\tau_1+\tau_2 = 0$, it is usually the practice to approximate this condition by switching in delaying cables in the IF line. Because of the discrete nature of these cables, however, continuous tracking of the delay would cause small jumps in the interferometer phase. Since the observations were short (15 minutes), it was feasible to hold τ_2 constant at a mean value of $-\tau_1$ during the observation, thereby avoiding the discontinuities in phase. Setting, then

$$\tau_1 + \tau_2 = \frac{d}{c}\sin\theta - \frac{d}{c}\langle\sin\theta\rangle$$

$$= \Delta\tau(t),$$

equation (1.1) becomes

$$R = GA(\Delta\tau)\cos\left[(\omega_{LO}+\omega_{IF})\frac{d}{c}\sin\theta - \omega_{IF}\frac{d}{c}\langle\sin\theta\rangle + \Psi\right]$$

Because $A(\Delta\tau)$ is negligibly different from $A(0)$ we have succeeded in maximizing the fringe amplitude as effectively as if we had tracked delay. Note that it is imperative to record the value of τ_2 during the observation if the phase of the fringes is to be determined.

If we define the baseline length in wavelength units

$$2\pi S = (\omega_{LO} + \omega_{IF})\frac{d}{c}$$

then

$$R = GA(\Delta\tau)\cos\left[2\pi S\sin\theta + \Psi\right]. \tag{1.2}$$

To the extent that the receiver is stable over time periods greater than the observation time, G and Ψ are constants. This point is covered further in the section on calibration. Note that had we been able continuously to track delay the effective baseline length in wavelengths would have been reduced by the factor $\frac{\omega_{LO}}{\omega_{LO}+\omega_{IF}}$.

The analysis given in the Appendix does not deal with the problem of system noise. As a practical matter noise arises primarily in the first stages of the receivers. It can thus be added to the input noise y(t) at each antenna. The interferometer will only sense that fraction of the noise for which the cross-correlation is non-zero. The result is simply to add the instantaneous cross-correlated noise power to A(0). If this noise power is comparable to that due to the source, the fringes described by equation (1.2) can be obscured. The effect of uncertainty in fringe amplitude on the measurement of the fringe phase is treated in the section on errors (Chapter 3).

2. Response to Extended Sources

Equation (1.2) gives the single sideband interferometer response to a point source. The motion of the source at the sidereal rate across the sky causes θ to increase and produces the interference fringes. To obtain the response to an extended source, we must integrate the source distribution over the fringe pattern.

It is convenient to refer the source to a Cartesian coordinate system with one axis parallel to a circle of declination, increasing to the east, and the other increasing to the north. The term S sinθ is similarly broken up into components u and v along these axes. The integral becomes

$$R(u,v,t) = \iint GA \cos \{2\pi [u(x-\Omega t)+vy]+\Psi\} B(x,y)\ dxdy,$$

where x and y are in radians, and Ω is the sidereal rate. Note that the relation

$$S \sin\theta = u(x-\Omega t) + vy$$

is valid only over a small region, but it is assumed that outside this region the brightness distribution B(x,y) is zero. The baseline projections u and v are readily expressed in terms of the interferometer geometry (see for example Moffet 1962).

The solution of the integral is available upon inspection if we use exponential notation

$$R(u,v,t) = \mathrm{Re}\ GA\ e^{i\Psi}\ e^{-2\pi i u\Omega t} \iint B(x,y) e^{2\pi i(ux+vy)} dxdy.$$

The integral term is just the (complex) Fourier transform of the brightness distribution, defined to be the visibility function $\hat{V}$

$$\mathrm{F.T.}[B(x,y)] = \hat{V}(u,v) = Ve^{i\Phi}. \qquad (1.3)$$

(Frequently in the literature V is normalized to 1 at zero spacing.) With this definition

$$R(u,v,t) = GAV \cos\left[2\pi u\Omega t - \Phi - \Psi\right]. \qquad (1.4)$$

Thus an extended source also produces fringes, but with amplitude and phase determined by the visibility function.

Equation (1.4) is the fundamental equation of aperture synthesis. It shows that by measuring the amplitude and phase of the interferometer fringes, we may recover the value of $Ve^{i\Phi}$ at (u,v). By rearranging the configuration of the instrument, samples can be made over an extended range of u and v after which equation (1.3) is invoked to recover B(x,y). It is obvious that no practical interferometer can fully sample the (u,v) plane, however, and this fact limits the fineness of the synthesis. There are really two classes of limitations; the first, dictated by the maximum separation of the instrument, causes $\hat{V}$ to be completely unsampled outside a given area. The maximum spacing can be dictated by signal-to-noise considerations as well as physical constraints. Lack of measurements at high spatial frequencies causes loss of definition in the inverted brightness map. The second kind of limitation arises because the interferometer elements can only be placed in certain configurations. This results in discontinuous sampling of $\hat{V}$ and places restrictions on the size of sources that can be synthesized.

Let S(u,v) be a sampling function and W(u,v) its support. By support is meant a function equal to one within the bounds of the measured visibility plane and zero outside. S(u,v) is generally some sort of two-dimensional "spikey" function. Then the measured visibility function $\hat{V}$ is given by

$$\hat{V} = WS\hat{V}_o. \qquad (1.5)$$

Taking the transform, and using the convolution theorem[1]

$$B = w*s*B_o. \qquad (1.6)$$

---

[1] The * indicates convolution and lower-case letters denote transformed quantities.

The term $s*B_o$ is the true brightness distribution repeated on s(x,y), the grating response pattern. This is particularly evident if the sampling function S(u,v) is a regular, rectangular "bed-of-nails" function

$$S(u,v) = \sum_{mn}\sum \delta(u - m\Delta u)\ \delta(v - n\Delta v).$$

Then its transform is also a "bed-of-nails" function with reciprocal spacing

$$s(x,y) = \sum_{kl}\sum \delta(x - \frac{k}{\Delta u})\ \delta(y - \frac{l}{\Delta v}),$$

and B will be repeated at each of these lattice points. It is these repetitions that are meant when one speaks of grating response. Another way of looking at this is to note that by regularly sampling $\hat{V}$ we have made a Fourier series of B, rather than an integral transform

$$B(x,y) = \iint_{-\infty}^{\infty} \hat{V}(u,v) e^{-2\pi i(ux + vy)} dudv, \tag{1.7}$$

$$\begin{aligned} B'(x,y) &= \iint_{-\infty}^{\infty} \sum_{mn}\sum \delta(u - m\Delta u)\ \delta(v - n\Delta v) \\ &\qquad \cdot\ \hat{V}_o(u,v) e^{-2\pi i(ux + vy)} dudx, \\ &= \sum_{mn}\sum\ \hat{V}_o(m\Delta u, n\Delta v) e^{-2\pi i(m\Delta ux + n\Delta vy)} \Delta u\Delta v. \end{aligned} \tag{1.8}$$

The series repeats with a frequency given by its lowest order term. The coefficients of the series are the measured values of $\hat{V}$. In order, then, that the inverted map not be confused with its grating responses we must satisfy the conditions

$$X \leq \frac{1}{\Delta u}, \quad Y \leq \frac{1}{\Delta v}, \tag{1.9}$$

where X and Y are the maximum (angular) dimensions of the source in the x and y directions. This is simply a statement of the sampling theorem. For sources for which the relations (1.9) are equalities, values of the visibility function at the lattice points are independent. For smaller sources, these points contain some redundancy.

It should be remembered that while equations (1.9) are useful in assessing whether a given source can be synthesized, practical interferometers generally do not sample on rectangular lattices. The actual sampling lattice for NGC4236 is shown in Figure 1. A similar lattice obtains for NGC2403. For IC10, the coverage is less complete and is shown in Figure 2. The only way to determine the grating response s(x,y) for such an irregular pattern is by a numerical transform. This is discussed in Chapter 3.

Returning to equation (1.6), the repeated brightness distribution is convolved with w(x,y), the transform of the support function. w(x,y) is the synthesized beam pattern, or point source response, and acts as a spatial filter in eliminating detail from the synthesized brightness distribution. It is customary to taper the support function W(u,v) to reduce the sidelobes of the beam pattern. This is done by appropriately weighting the measured visibility. The penalty for this procedure is a slightly wider beam.

The discussion so far has assumed interferometer elements with isotropic response. In fact, of course, the final brightness distributions have been multiplied by the power pattern of an individual antenna, or, if the two antennas have unequal gains, by $\sqrt{A_1(x,y)A_2(x,y)}$. A_1 and A_2 are the individual patterns. Correction for this attenuation of the outer edges of the maps is easily performed once the composite beam is known. One could include this effect in the formalism of equations (1.5) and (1.6) by convolving the sampling function S with the transform of the

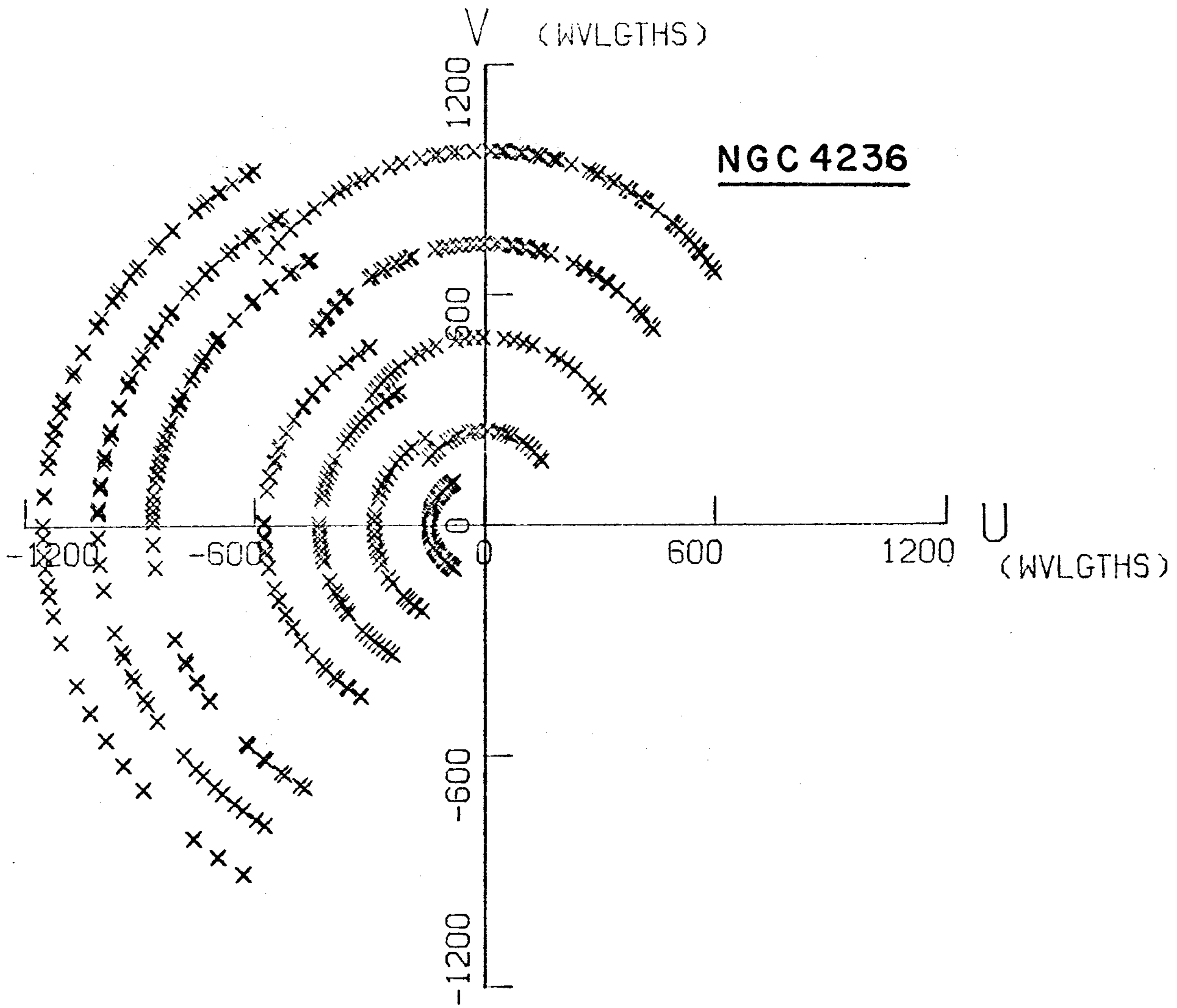

Figure 1. Data coverage in the visibility plane for NGC4236. Each cross represents a fifteen-minute observation. Total number of observations is 582.

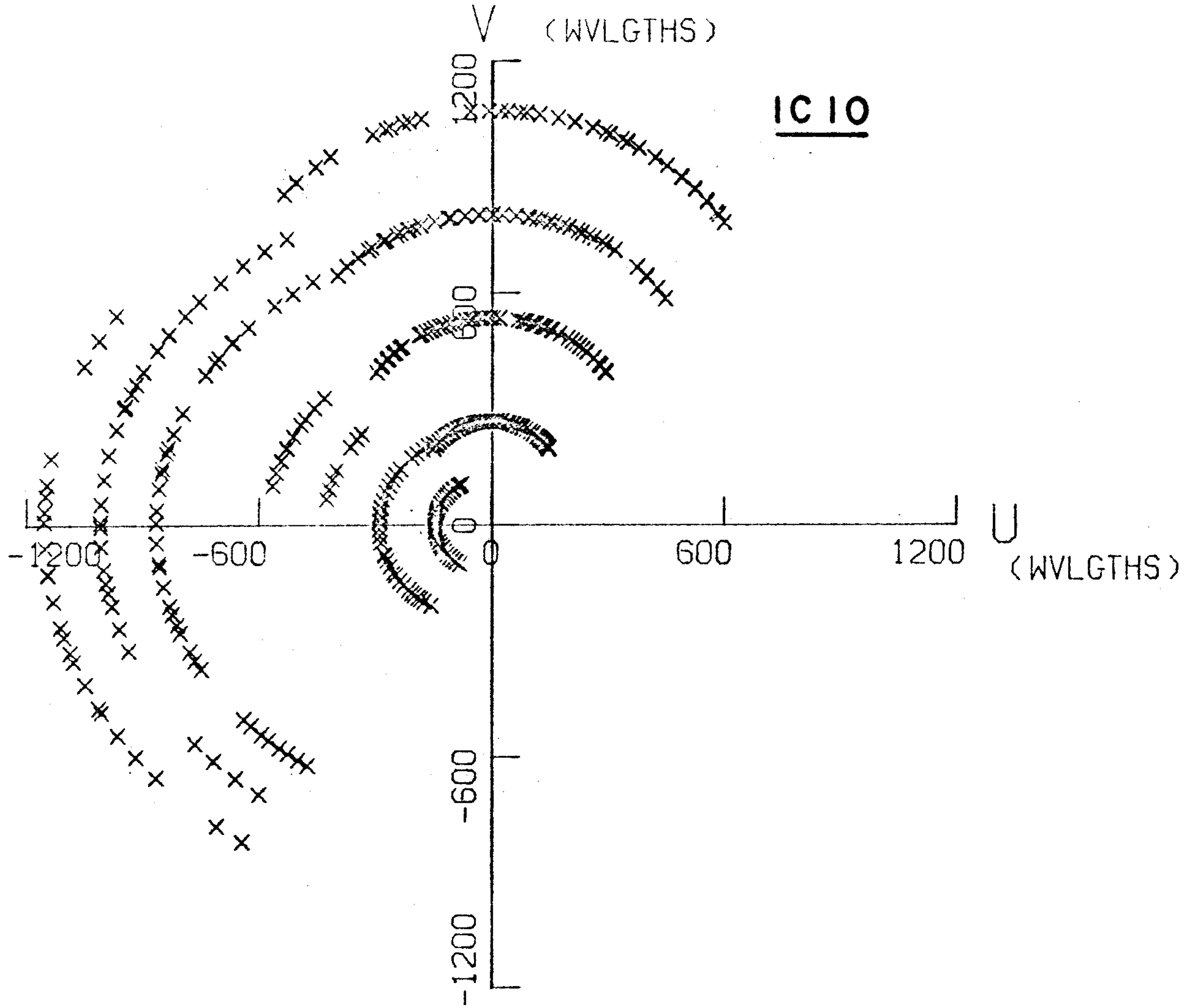

Figure 2. Data coverage in the visibility plane for IC10. Each cross represents a fifteen-minute observation. Total number of points is 442.

composite primary beam. To this visibility "smearing" function one might add the small arc swept out in (u,v) space during the finite integration time of a single observation.

II. OBSERVATIONS

1. Selection of Sources

Because of the extensiveness of the observations, it was early realized that only a very few objects could be synthesized. Nevertheless, the choice of these objects was still largely dictated by instrumental limitations. The more important considerations were:

1) The object should, of course, have detected HI emission, and stronger sources are evidently preferred. The term "stronger" refers here to surface brightness.

2) Source size should be a good match to the instrument's capabilities. It should be large compared with the synthesized beamwidth (2 arcmin). On the other hand, with spacings only available every 100 feet east-west and every 200 feet north-south, grating responses appear outside an area of dimensions 24' x 12'. This condition is somewhat ameliorated by the close spacing of the observations in hour angle (see Chapter 3). An ultimate size limitation is imposed by the primary antenna response of approximately 35' x 35'.

3) The velocity spread of the galaxy should be sufficient to ensure that filter smearing would not become comparable with beam smearing. For this reason, face-on galaxies were to be avoided. Velocity spread should not

exceed the maximum coverage of the filter bank (480 km-s^{-1}).

4) Full coverage in the visibility plane can only be accomplished for sources north of 52° declination without resort to skewed baselines.

5) For sources near the galactic plane, the systemic velocity should be well away from zero to avoid confusion by local hydrogen.

6) Sources should be free of confusion-causing companions and strong continuum sources.

The more important surveys of HI in external galaxies began with Epstein (1964) and Roberts (see Roberts 1966b). Other work using narrower beams on the brighter objects was done by Roberts (summarized in Roberts 1970), Volders and Hogbom (1961), Heidmann (1961), Van Damme (1966), Shobbrook and Robinson (1967), and Lewis (1968). M31 has been the subject of several investigations including Roberts (1966a) and Gottesman _et_ _al_. (1966). Thirty galaxies were studied with a single-spacing interferometer by Seielstad and Whiteoak (1965) and Rogstad _et_ _al_. (1967). A very extensive effort at Nancay has detected emission in many smaller galaxies (Bottinelli _et_ _al_. 1968; Gouguenheim 1969). At the time of this writing, approximately 130 galaxies had been observed in the hydrogen line.

A sifting of these objects was undertaken with regard to those properties of particular relevance to the restrictions discussed above. This was done in collaboration with

D. Rogstad, as observations out to the 400-foot spacing were to be taken jointly. An effort was made to include objects of various morphological type, but was largely frustrated by the overwhelming preponderence of late-type spirals in the lists of detected galaxies. Due to the clustering of galaxies near 12 hours right ascension, further compromise was necessary to obtain a source list which could be efficiently observed.

The combined observing list is shown in Table 1, along with those properties relevant to their selection. Columns (2), (3) and (4) give the 1950.0 coordinates and morphological type from de Vaucouleurs (1964); column (5) the dimensions from Holmberg (1958) or, in the case of the IC objects, from de Vaucouleurs or Epstein (1964a). Column (6) gives the inclinations to the sky plane from Danver (1942) or Epstein; column (7) the velocity profile widths from Rogstad _et_ _al_. (1967), Seielstad and Whiteoak (1965), and Epstein. The average flux and HI systemic velocity as taken from Epstein or Rogstad _et_ _al_. are listed in columns (8) and (9). Several comments regarding this list should be made: NGC224 (M31) was not originally part of the observing program due to its very large size. It was later included with the anticipation that by careful choice of filter values a small section of the galaxy could be synthesized. It was similarly hoped that IC342 and NGC5457

TABLE 1

Combined Observing List

NAME NGC (*IC) (1)	α (1950) (2)	δ (1950) (3)	TYPE (4)	SIZE (5)	i (6)	ΔV (km/sec) (7)	$\overline{S}\nu$ (flux units) (8)	V_{HI} (km/sec) (9)	DISTRIBUTION†
*10	$00^h17.6^m$	59° 02'	Irr	4'.0 x 2'.8		125	3.1	-350	S
224	00 40.0	41 00	Sb	197 x 92	75	500	65	-300	R
*342	03 41.9	67 57	Scd	40 x 33	35	110	22	56	R
2403	07 32.0	65 43	Scd	29 x 15	55	300	3.8	128	S
4236	12 14.3	69 45	SBdm	26 x 8.7	75	225	2.5	5	S
5457	14 01.4	54 35	Scd	28 x 28	27	200	12	235	R
6946	20 33.9	59 58	Scd	14.4 x 12.6	31	275	2.9	45	R

†S indicates Shostak, R Rogstad. Information is from references cited in text.

(M101) would also prove to be of manageable size within the velocity increment of the filters. IC10, although of small optical dimensions, was suspected of being partially obscured by the plane of the Milky Way. The possibility existed that HI observations might show it to be a much larger Sc galaxy. If not, it at least provided the source list with one irregular object.

When, in April, 1969, the observations to 400 feet had been completed, a division of the data was made. Rogstad assumed responsibility for the four objects so listed in Table 1, leaving NGC2403 and NGC4236 as subjects for this thesis. Choice of these two objects was based on their suitability for further observations to 800 feet. This was determined by the strength of the fringe visibilities at 400 feet and expected velocity gradients. IC10, which earlier had been displaced from the program by the inclusion of M31, was later observed at all the larger spacings. A special observing run was used to fill in the more important of the missing short spacings for this object.

2. Observational Procedures

It is generally appreciated that two-dimensional synthesis with a two element interferometer is a time consuming project. The current undertaking required 85 days of observing time, although it should be mentioned that this includes those observations done jointly with Rogstad. For those whom it might interest, the chronology of the observations is given in Table 2.

Front and rear-end equipment for all observations (save the zero-spacing measurements) was unchanged with spacing. Parametric amplifiers followed by tunnel diode amplifiers preceeded crystal mixers at the front end. The 10 MHz IFs so produced were amplified by broad-band (nominally 5 MHz) amplifiers and then sent to a bank of 23 filters. The filter outputs were multiplied and fed to d.c. amplifiers with an approximately 12 second time constant. The 23 narrow-band and one broad-band channel outputs were sequentially sampled and recorded on magnetic tape for later analysis. Filters inserted before the mixers ensured response to only one sideband.

Repeated single dish measurements of the system temperatures for each antenna showed them to be about 130°K, assuming the dish efficiency to be 43%. One of the calibrator sources (3C48) was interferometrically observed to obtain the composite single dish beam pattern, shown in Figure 3.

The integration time per observation was fifteen minutes. For sources near the poles, the apparent source rotation with respect to the projected baseline of the interferometer is about $-\frac{\pi}{12}\sin\delta$ radians per hour. The

TABLE 2

Chronology of Observations

OBSERVATION DATES	SPACING	OBJECTS†
1968		
JUL 19 - JUL 25	100' E/W	GSS, DHR (less NGC224)
JUL 27 - JUL 30	200' E/W	GSS, DHR (less NGC224)
DEC 4 - DEC 7	100' E/W	NGC2403, NGC4236, DHR
DEC 8 - DEC 12	200' E/W	NGC2403, NGC4236, DHR
DEC 13 - DEC 16	200' N/S	NGC2403, NGC4236, DHR
1969		
MAR 12 - MAR 18	400' E/W	GSS, DHR
MAR 19 - MAR 25	300' E/W	GSS, DHR
MAR 27 - APR 1	400' N/S	NGC2403, NGC4236, DHR
AUG 13 - AUG 19	600' E/W	GSS, NGC6946
AUG 20 - AUG 24	700' E/W	GSS, NGC6946
AUG 24 - AUG 29	800' E/W	GSS, NGC6946
SEPT 13 - SEPT 17	800' N/S	GSS, NGC6946
OCT 29 - NOV 3	600' N/S	GSS, NGC6946
1970		
AUG 14 - AUG 17	400' N/S	IC10
AUG 18 - AUG 24	200' N/S	IC10
SEPT 3 - SEPT 8	ZERO SPACING	GSS

†GSS indicates synthesis objects NGC2403, NGC4236 and IC10. DHR indicates Rogstad sources IC342, NGC5457, NGC6946, and NGC224.

outer regions of a 30' diameter, high declination source therefore rotate through roughly 3' per hour. In order to keep this "rotational smearing" small compared with the synthesized beam, the quarter-hour integration time was adopted. Another way of stating this is to say that measurements of the visibility function should not be smeared over an area comparable with a unit cell. (A unit cell is defined as the area $\Delta u \Delta v$ where Δu and Δv satisfy the equalities of equation 1.9). A given source was generally observed for eight hours at a time, the maximum tracking range of the instrument. Except at the shortest baselines, a minimum of two eight-hour observations was made per spacing for each source.

The twenty-three narrow-band channels employed conventional double-tuned filters with 100 KHz (21.1 km-s^{-1}) nominal halfwidth. A typical filter response is shown in Figure 3. The center frequencies of the filters were spaced 100 KHz apart, thereby providing complete velocity coverage over 480 km-s^{-1}. Several times during the two year period of observations the filter positions and shapes were measured as a check on their constancy. In some cases center frequencies suffered long term shifts of as much as 30 KHz. Such shifts will naturally cause some distortions in the narrow-band maps, although the principal effect is simply to broaden the effective filter widths by, at most,

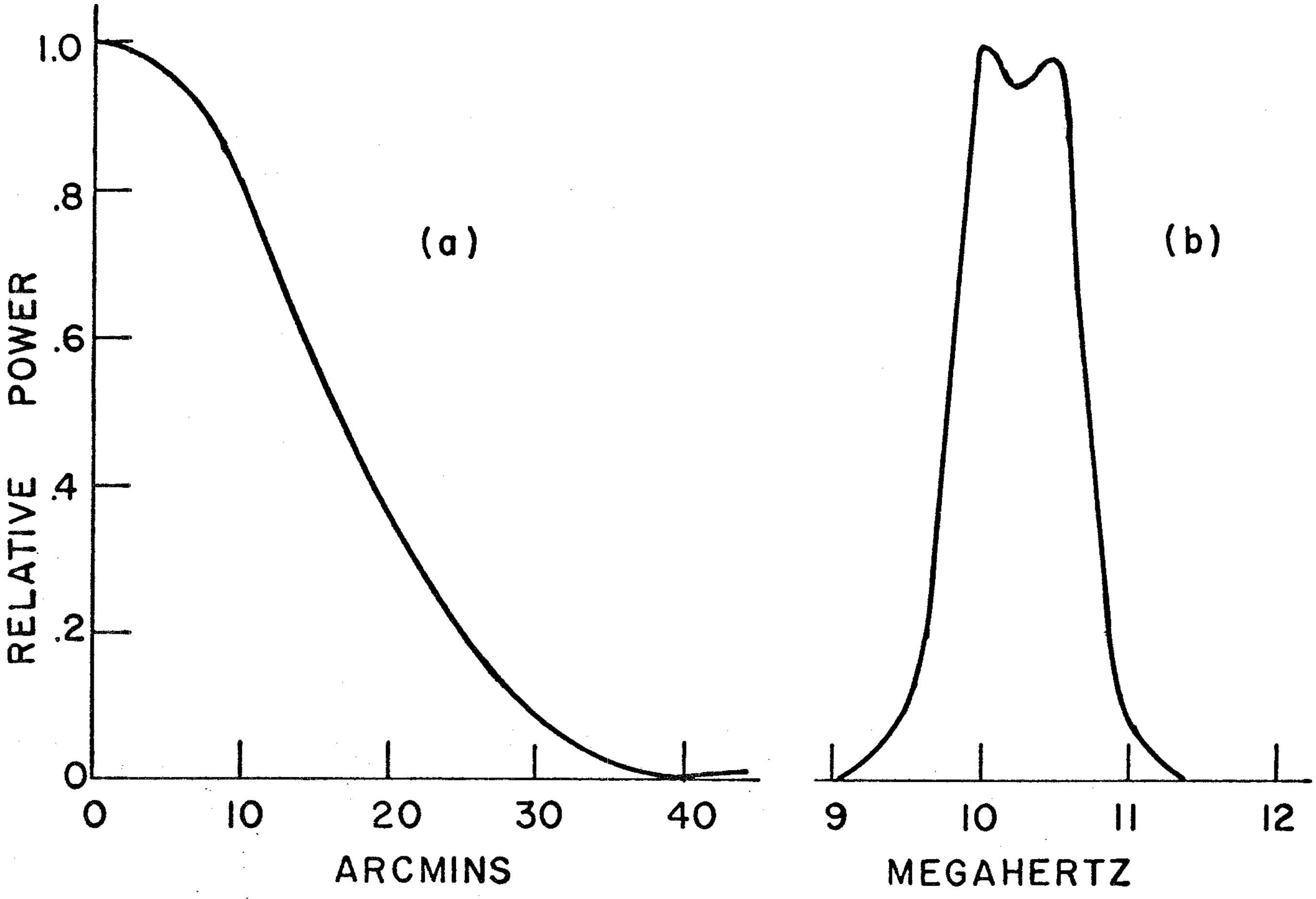

Figure 3. (a) Composite single antenna response. (b) Typical narrow-band filter response.

15%. Such an effect is generally negligible in comparison with beam smearing.

3. Reduction and Calibration

The digitized interferometer records were reduced on the Caltech I.B.M. 360/75 computer using the standard Owens Valley programs, written by E. Fomalont, F. Bartlett and D. Rogstad. The output of these programs consisted of uncalibrated amplitudes and phases for each observation. A description of the reduction technique has been given by Fomalont, Wyndham and Bartlett (1967). Correction of these quantities to their true values involves removing long-term instrumental phase and gain variations and an additional phase adjustment due to incorrectly estimated baseline parameters.

Instrumental changes were determined by observations of standard sources (calibrators) approximately once each hour. Since the positions and fluxes of the calibrators are known, their observed phases (after baseline correction) give the instrumental phase function directly. Dividing amplitudes by fluxes produces an instrumental gain function. These data were interpolated for use in calibrating the observations by convolution along the time axis with an exponential function. The width of the smoothing function was several hours in order that excessive weight might not be attached to a single observation. Deviations of the data from the interpolated curves were used to estimate the amount of calibration error being introduced into the source observations.

The above procedure was employed solely with the broad-band channel. Since the narrow-band and broad-band equipments are identical until after the IF amplifiers, by which point most instrumental variations have already been introduced, separate hourly calibration of each channel is unnecessary. Instead, for each eight-hour galactic observation the average phase and gain differences between each channel and the broad-band values were ascertained. It was assumed that these differences were systematic and, except for such offsets, the narrow-band instrumental phase and gain curves were the same as the broad-band. The net effect of the calibration procedure was to introduce additional uncertainties in the narrow-band observations of approximately 5% in gain and 0.02 lobes in phase. The determination and implication of these numbers is discussed in Chapter 3.

The calibrators used for the source observations are listed in Table 3. For each galaxy the primary calibrator, generally used for 80% or more of the calibration, is listed first. The tabulated positions and fluxes are those actually used in the calibration procedure. They were largely taken from Fomalont (1967) and Fomalont, Wyndham

TABLE 3

Source Calibrators

	α (1950)	δ (1950)	FLUX
NGC2403			
3C196	08 09 59.39	48 22 08.0	14.25
3C147	05 38 43.53	49 49 43.1	22.24
3C268.1	11 57 45.70	73 17 32.0	6.68
3C48	01 34 49.82	32 54 20.2	15.63
3C119	04 29 07.84	41 32 08.7	8.55
NGC4236			
3C268.1	11 57 45.70	73 17 32.0	6.68
3C280	12 54 41.70	47 36 38.0	5.19
3C196	08 09 59.39	48 22 08.0	14.25
3C295	14 09 33.44	52 26 13.6	22.40
IC10			
3C48	01 34 49.82	32 54 20.2	15.63
3C468.1	23 48 25.90	64 23 30.0	4.72
3C147	05 38 43.53	49 49 43.1	22.24
3C438	21 53 45.50	37 46 14.0	6.75
3C119	04 29 07.84	41 32 08.7	8.55
NGC6946			
3C418	20 37 07.40	51 08 35.0	5.90
3C401	19 39 38.82	60 34 31.5	4.90
3C468.1	23 48 25.90	64 23 30.0	4.72
3C438	21 53 45.50	37 46 14.0	6.75
3C380	18 28 13.40	48 42 39.3	14.50
CTA102	22 30 07.71	11 28 22.8	6.80
3C295	14 09 33.44	52 26 13.6	22.40
NGC5457			
3C295	14 09 33.44	52 26 13.6	22.40
3C286	13 28 49.74	30 45 59.3	15.42
3C401	19 39 38.82	60 34 31.5	4.90
3C380	18 28 13.40	48 42 39.3	14.50
3C280	12 54 41.70	47 36 38.0	5.19

Table 3 (continued)

IC 342			
3C119	04 29 07.84	41 32 08.7	8.55
3C401	19 39 38.82	60 34 31.5	4.90
3C48	01 34 49.82	32 54 20.2	15.63
CTA102	22 30 07.71	11 28 22.8	6.80
3C91	03 34 03.80	50 36 03.0	3.35
3C147	05 38 43.53	49 49 43.1	22.24
NGC 224			
3C48	01 34 49.82	32 54 20.2	15.63
3C409	20 12 18.10	23 25 43.0	13.80
3C468.1	23 48 25.90	64 23 30.0	4.72
3C401	19 39 38.82	60 34 31.5	4.90

and Bartlett (1967). Comparison with more recent studies (Fomalont and Moffet 1971; Wade 1970) suggest that the positions of the principal calibrators are correct to within about 2 arcsec. At worst, this could cause a maximum of 0.01 lobe variable phase error (with hour angle) at the largest spacing. The uncertainty in the fluxes is 2%, a negligible amount.

Early observations revealed absorption by local hydrogen in several of the calibrators. When this was discovered, the absorbed source was no longer used in the calibration of the narrow-band channels. In a few cases it was necessary to determine the absorption profile to correct observations already taken. For the case of 3C418, an absorption profile was kindly supplied by M. Hughes (1969). Other sources in which absorption occurred in the observed velocity range were 3C147, 3C119 and 3C468.1.

Because of inaccuracies in the setting down of the antennas after a baseline change, a calibration procedure was required to accurately determine the interferometer pole. The pole is defined by the line connecting the vertices of the two parabolic antennas. Although in principle this can be done by observing just three sources, as a practical matter instrumental phase changes would make such a determination unreliable. In order to successfully remove such changes, and at the same time minimize the effect of inaccuracies in the source positions, at least a dozen sources are observed. A least-squares fit, which allows for the time-dependent instrumental phase, is then made to the baseline configuration. The sources used for this calibration, along with their adopted positions, are listed in Table 4. The fluxes are relevant only insofar as they influence slightly the accuracy of the phase measurements. Typical baseline corrections would be 30 arcsec angular and 0.5 inch linear change from the nominal values.

One further possible source of error in the measurements should be mentioned. In obtaining raw phases from the digitized records, the reduction program subtracts all the non-constant terms from the cosine argument of equation (1.1). To do this, the program requires values for ω_{LO} and ω_{IF}. The former is accurately known, but the latter, which is in fact the centroid of the IF bandpass (see Appendix), may be significantly different from the nominal 10 MHz value. Note that we are speaking here of the broad-band channel only, since the narrow-band IF frequencies are determined by the filters and therefore are accurately known. The amount of phase error so introduced is easily estimated: Assume for the moment that the instrumental phase is zero. Let the IF frequency be

$$\omega_{IF} = \omega_{IFo} + \Delta\omega_{IF},$$

TABLE 4

Baseline Calibrators

	α (1950)	δ (1950)	FLUX
3C48	$01^h\ 34^m\ 49.82^s$	32° 54' 20.2"	15.63 f.u.
P0405-12	04 05 27.40	-12 19 32.0	3.35
3C133	04 59 54.30	25 12 12.0	5.60
3C181	07 25 20.36	14 43 47.2	2.35
P0736+01	07 36 42.40	01 44 00.0	2.50
3C268.1	11 57 45.70	73 17 32.0	6.68
3C273	12 26 32.90	02 19 38.0	43.0
P1256-19	12 45 45.30	-19 42 57.0	5.40
3C279	12 53 35.94	-05 31 08.0	11.0
3C286	13 28 49.74	30 45 59.3	15.42
3C295	14 09 33.44	52 26 13.6	22.40
3C298	14 16 38.82	06 42 21.6	5.85
3C309.1	14 58 58.20	71 52 09.0	8.50
P1510-08	15 10 08.90	-08 54 48.0	3.95
3C317	15 14 17.00	07 12 16.7	5.45
3C318	15 17 50.74	20 26 53.5	2.65
3C345	16 41 17.70	39 54 11.1	7.0
NRA0530	17 30 13.55	-13 02 50.0	5.0
3C371	18 07 18.44	69 48 56.6	1.4
3C380	18 28 13.40	48 42 39.3	14.50
M19-1/11	19 38 24.30	-15 31 34.0	6.80
3C401	19 39 38.82	60 34 31.5	4.90
3C409	20 12 18.10	23 25 43.0	13.80
3C418	20 37 07.40	51 08 35.0	5.90
3C424	20 45 44.40	06 50 10.2	2.20
P2115-30	21 15 11.00	-30 31 53.0	2.55
P2127+04	21 28 02.61	04 49 04.1	3.0
P2145+06	21 45 35.90	06 43 43.0	2.90
3C438	21 53 45.50	37 46 14.0	6.75
3C446	22 23 11.05	-05 12 17.0	5.90
CTA102	22 30 07.71	11 28 22.8	6.80
P2259-37	22 59 37.30	-37 34 20.0	2.60
3C459	23 14 02.30	03 48 56.9	4.40

where ω_{IFo} is the nominal value. The computer will subtract the quantity

$$(\omega_{LO} + \omega_{IFo})\tau_1 + \omega_{IFo}\ \tau_2$$

from the cosine term of equation (1.1), leaving

$$R = GA \cos[\Delta\omega_{IF}(\tau_1 + \tau_2)].$$

As described in Chapter 1, it was a standard procedure during the course of the observations to set τ_2 equal to the mean value of $-\tau_1$ (within an additive constant). If, however, the value of τ_2 is incorrectly set by the amount $\Delta\tau$, then a residual phase of $\frac{\Delta\omega_{IF}\Delta\tau}{2\pi}$ lobes is introduced. Since the mis-setting of delay τ_2 is unsystematic, this residual phase is not removed in the instrumental phase calibration. However, experience shows the inaccuracy in the delay setting to average less than 2 nanoseconds. With even as much as a 1 MHz error in the value of ω_{IF}, this causes only 0.002 lobes phase error.

4. Zero-Spacing Observations

The minimum interferometer spacing used in this work was 100 feet (144λ), the same baseline used by Seielstad and Whiteoak (1965) and Rogstad et al. (1967). These authors, whose observations included the sources under study here, noted that most objects were substantially resolved at this spacing for certain hour angles. As indicated in Chapter 3, preliminary inversions of the interferometer data alone produced spectra which had systematically lower fluxes than those published for NGC2403 (Roberts 1962a) and IC10 (Epstein 1964a; Roberts 1962b). No spectra, other than the interferometric data of Rogstad et al., exist for NGC4236. Since the very low spatial components of the source structure had evidently been resolved even at the minimum baseline, it was clear that a zero-spacing measurement had to be included in the inversions. The lack of an existing zero-spacing spectrum for one of the principal objects, plus the fact that the published spectra had been taken with filters slightly wider than those used in the present study, prompted an independent zero-spacing measurement.

The Owens Valley 130-foot antenna was employed, equipped with a parametric amplifier similar to those used with the interferometer. The back end consisted of a 100-channel autocorrelation receiver with a 2.5 MHz bandwidth. Effective spectral resolution was 25 KHz. A description of the autocorrelator has been given elsewhere (Weinreb 1963; Riegel 1966). The receiver operates in a switched mode, subtracting a comparison frequency spectrum from the one being observed. Unfortunately the front end passband was not flat over the necessary 5 MHz, and the resulting spectra were superimposed on a very large instrumental profile. It was necessary to observe blank sky to determine the profile.

Complications arising from this procedure include the possibility of a slow change in the receiver response over the course of the source-blank sky switching period (one hour). Additionally, confusing local hydrogen could now be introduced in both observations. Difficulties with the electronics invalidated many of the observations.

After the spectra had been obtained by subtracting blank sky from source spectra, they were further corrected for any residual baseline drift as judged by their emission-free regions. The scaling of the spectra was initially done by comparison with a noise tube, itself calibrated against Cygnus A. The flux of this object was taken to be 1590 flux units (Kellermann *et al*. 1969). The resulting spectra, however, were systematically too high as judged by published observations, perhaps due to uncertainties in the attenuators which followed the noise tube. In this circumstance the only recourse was to adopt a scaling factor. This was done by assuming that the interferometer channels for NGC4236 having the most spatially compact emission regions were unresolved at some point along the eight-hour track of the 100-foot baseline. To the extent that this is so, the maximum amplitude interferometrically observed is equal to the zero-spacing flux. Justification for this procedure derives from the fact that the channels used for the scaling produced maps of less than 5' extent in the east-west direction. The probability of low-level emission of a size comparable to the 24' fringe spacing seems small given the well-ordered velocity field and high inclination of this object (see Chapter 6). Broadening of the channel by random motions is of negligible importance.

The spectra for NGC2403 and NGC4236 are shown in Figures 4 and 5, in which the ordinates have been scaled according to the above procedure. Also shown are the spectra convolved to a 21 km-s^{-1} velocity resolution and sampled at the nominal velocities of the narrow-band channels. Where Galactic hydrogen has caused a disruption of the spectrum, the convolved values are omitted. Since the primary beam of the 130-foot telescope has a half-power width of 24', slight reductions in amplitude at the extreme velocities occurred for the larger objects. This was corrected in the case of the convolved spectra by multiplication with a restoring function determined from the centroids of emission at each velocity.

A more recent measurement of IC10's line radiation by W. Wright (1971) was used in the scaling of its spectrum, shown in Figure 6. Wright claims a scaling uncertainty of only a few percent. The profiles given by Roberts (1962b) and Epstein (1964a) for this object are about 50% higher in flux than the one shown here, which is perhaps indicative of the difficulties inherent in an absolute measurement of this kind. Indeed, Roberts (1969) has considered systematic differences in measured integrated HI profiles between observatories, finding, for example, that hydrogen masses derived at Green Bank are almost always greater than those found for the same objects at Nancay. Perhaps it is comforting to note that the profile found in the present study yields for NGC2403 a neutral hydrogen mass which lies between the values given by these two institutions (see Chapter 5). However, with due respect to the uncertainties involved, it is estimated that scaling inaccuracies could produce as much as a 20% error in the profiles given here when integrated over velocity.

In Figure 7 are shown the convolved profiles for all three objects together with the narrow-band fluxes obtained by integrating B(x,y) for a map inverted without a zero-spacing datum. It should be apparent that only mild resolution has occurred at the shortest baseline in many cases. IC10 shows the greatest disparity between the total fluxes measured interferometrically and with a single antenna. This is surprising in view of its small size both optically and in HI (see Chapter 4). An extended region of low-level emission is implied. Note that the dotted regions on the profiles, occurring where Galactic hydrogen was present in the single dish measures, are interpolated on the basis of the interferometric data.

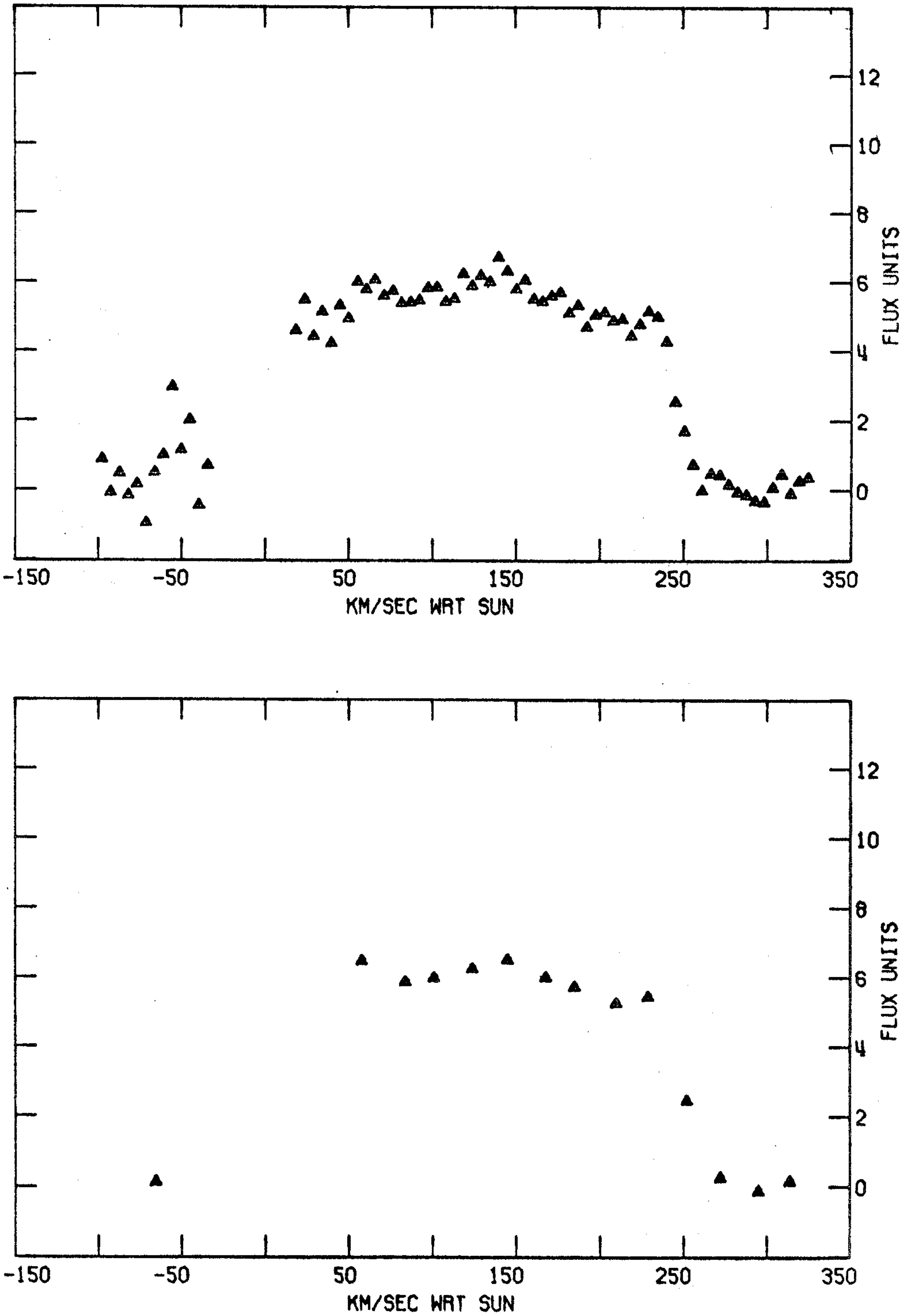

Figure 4. (a) Spectrum of NGC2403. (b) Corrected spectrum convolved to 100 KHz and sampled at the frequencies of the narrow-band channels.

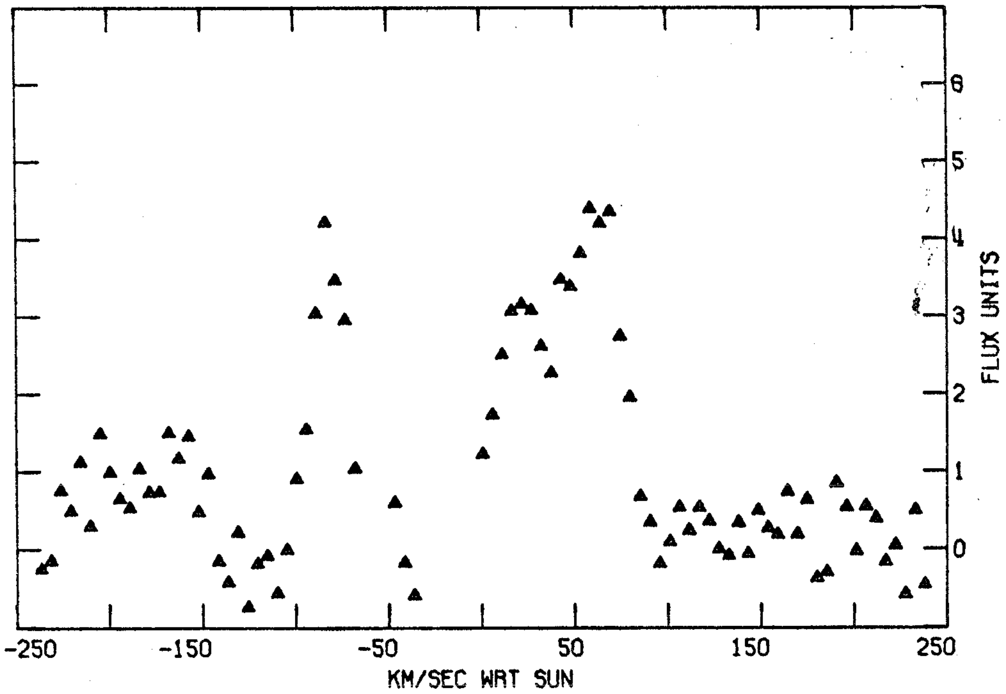

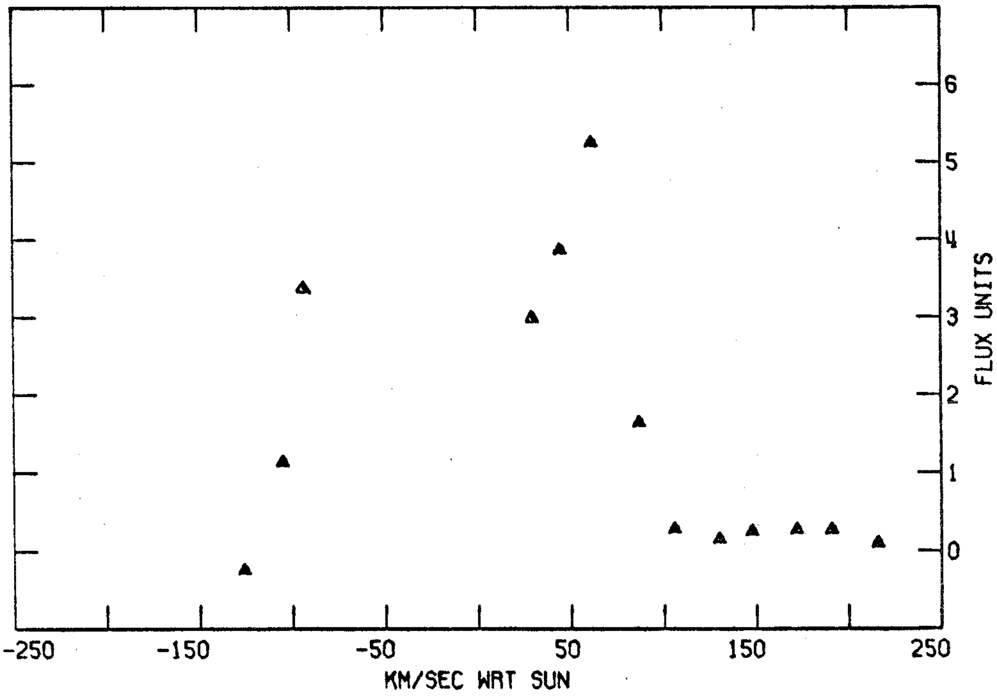

Figure 5. (a) Spectrum of NGC4236. (b) Corrected spectrum convolved to 100 KHz and sampled at the frequencies of the narrow-band channels.

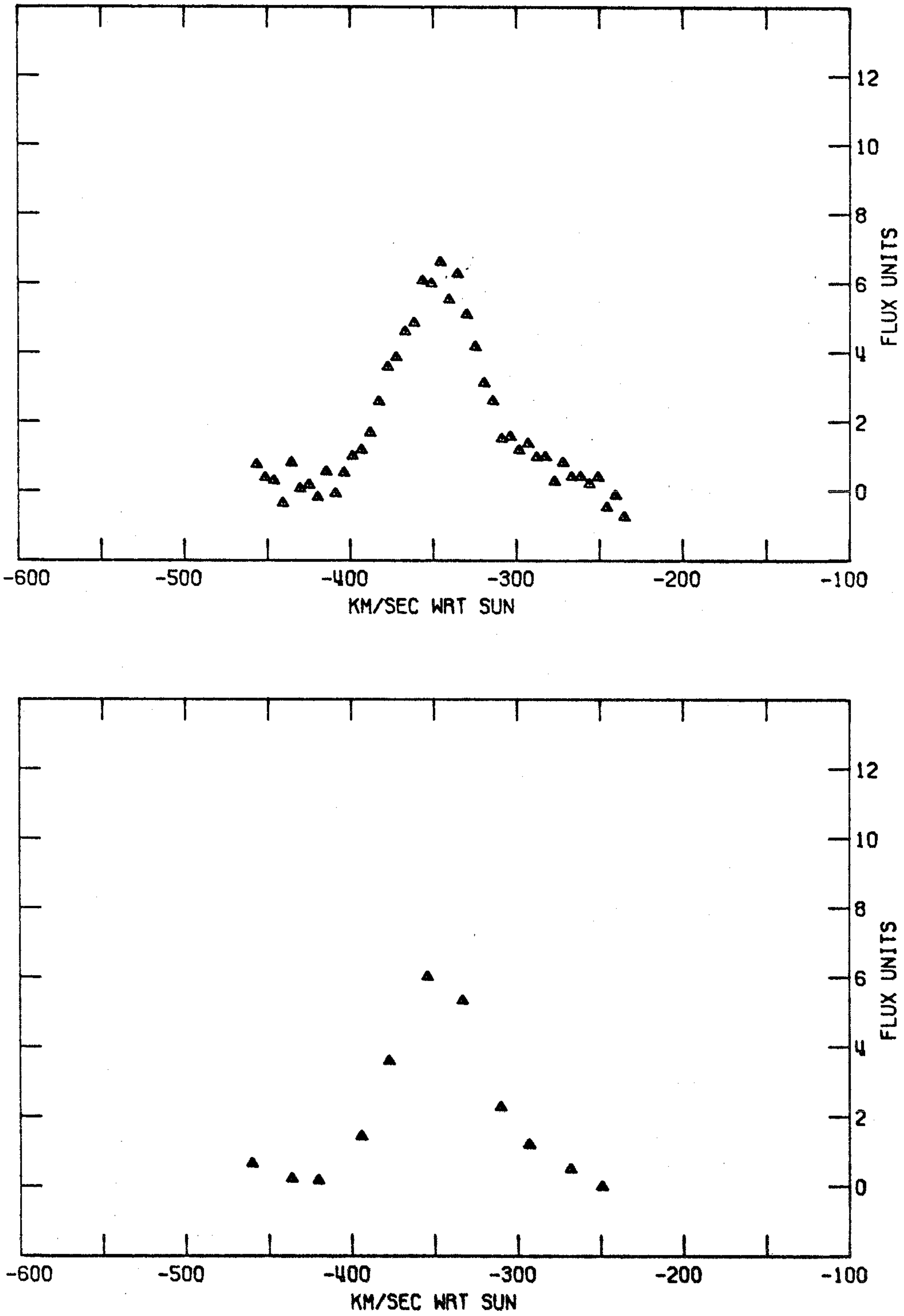

Figure 6. (a) Spectrum of IC10. (b) Corrected spectrum convolved to 100 KHz and sampled at the frequencies of the narrow-band channels.

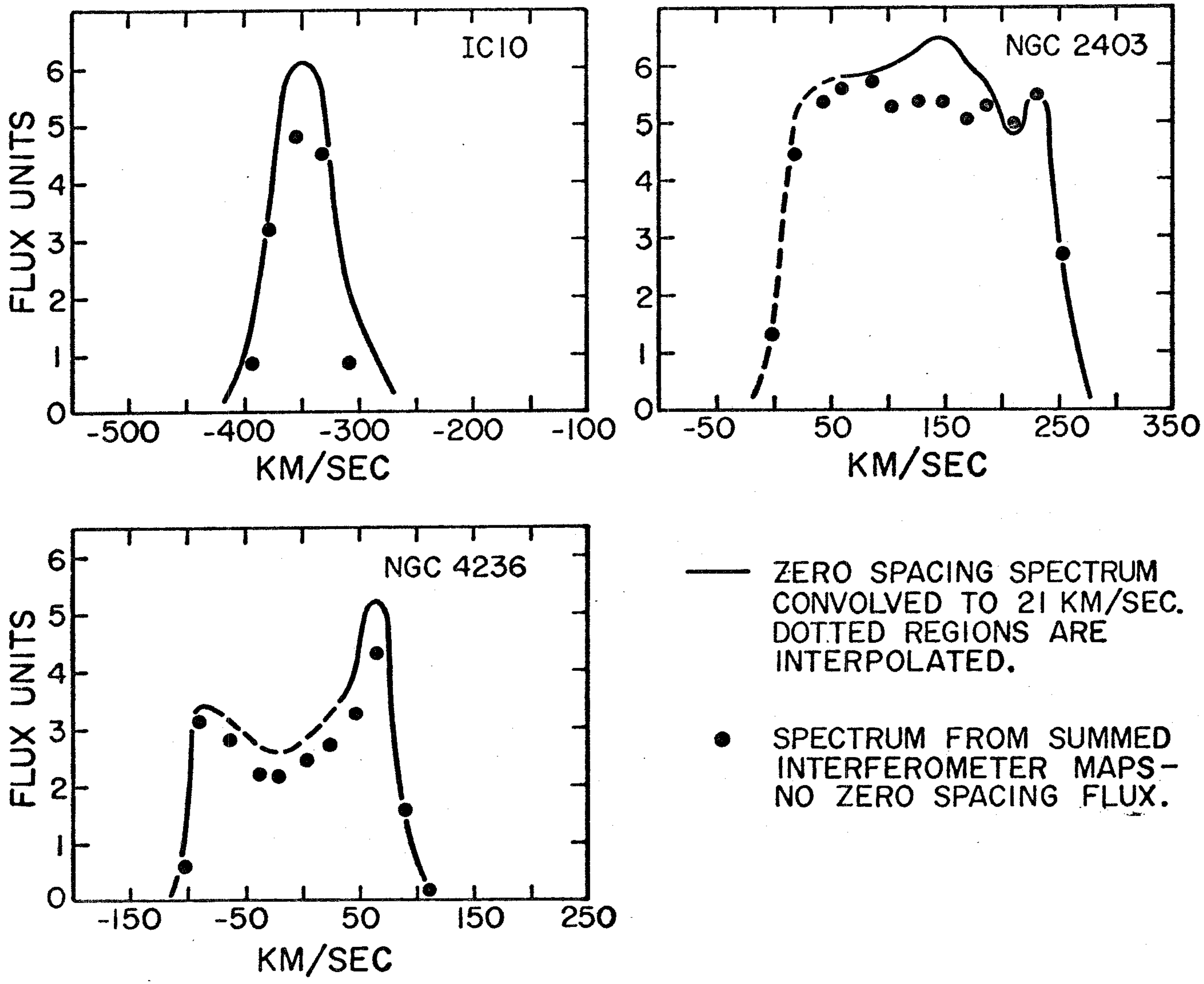

Figure 7. Spectra observed interferometrically and with a single dish.

III. INVERSION

1. Inversion Method

Several methods were considered for Fourier transforming the measured visibility function. The irregular spacing of the data makes formal integration impossible and numerical integration unwieldy. One approach is to fit the data with a sum of two-dimensional functions. Because of the Hermitian property of the visibility function, an even sum is fitted to Re $\hat{V}$ and an odd sum to Im $\hat{V}$. Once the fit is made, the transform is trivially obtainable since the transforms of the individual functions are known analytically. This method was tried using Cartesian prolate spheroidal wave functions, a complete set of functions which have the computationally convenient property of being eigenfunctions of the finite Fourier transform (Slepian and Pollak 1961; Landau and Pollak 1961). As a consequence, they contain relatively the greatest fraction of low-frequency energy of any functions, making them particularly efficient in the fitting of visibilities of extended sources. The method was discarded when it was found that the (least-squares) fitted functions invariably "blew up" in areas of low data density. Several other functions were tried with similar results.

A second approach is to interpolate the data onto a regular grid more amenable to numeric integration. By use of an elliptical coordinate system, Weiler (1969) reduced the necessary interpolation to one dimension but required a relatively complicated integration procedure. More common is the use of a rectangular lattice in which case the transform is immediately available as the Fourier series of (1.8). Gridding also has the advantage of reducing redundancy where large numbers of data points are involved, thereby speeding up computational procedures. The maps of the present study were produced by first smoothing the data onto a Cartesian lattice.

2. Interpolation to Lattice

Interpreting data to the grid is done by forming some sort of average of the data about the grid point. The real and imaginary parts of $\hat{V}$ are averaged separately as they are both continuous functions. This follows from the analyticity of $\hat{V}$, itself a consequence of the source distribution being bounded. As data spaced one unit cell apart (as defined by the source distribution) are independent, the averaging should only include points within one-half cell radius of the grid point. Furthermore, these relevant data points may be weighted differently depending on their signal-to-noise, distance from grid point, etc. In general, then, we may write the interpolated visibility function at lattice point n as

$$\hat{V}'_n = \sum_i G_i \hat{V}_i, \qquad (3.1)$$

where $\hat{V}_i$ are the visibility points sampled by the interferometer and G_i are associated interpolation weights. Since all data points had the same integration time, it was considered reasonable to make the G_i solely a function of the distance between the lattice point and the sampled visibilities. As discussed in Chapter 1 (equation 1.5), the measured data is simply the product of the true visibility and a sampling function

$$\hat{V} = S\hat{V}_o, \qquad (3.2)$$

where S(u,v) now includes the support function. We may then rewrite the visibility at lattice point n as

$$\hat{V}'_n = \iint_{-\infty}^{\infty} S(u',v')V_o(u',v')G(u_n - u', v_n - v')du'dv'. \qquad (3.3)$$

Because of the "spikey" nature of S, this integral representation is identical to the summation of (3.1). In order to get the best estimate of the visibility at the lattice point, we form a weighted average

$$\hat{V}_n = \frac{\iint_{-\infty}^{\infty} S(u',v')V_o(u',v')G(u_n - u', v_n - v')du'dv'}{\iint_{-\infty}^{\infty} S(u',v')G(u_n - u', v_n - v')du'dv'} . \qquad (3.4)$$

When the denominator, which is clearly the convolution of S and G, vanishes, $\hat{V}_n$ is defined to be zero. We may conveniently regard the reciprocal of the denominator as a weighting function C(u,v)

$$C(u,v) = (G*S)^{-1}$$

Let the new rectangular lattice be $E(u_n,v_n)$; the interpolated visibility becomes

$$\hat{V}'(u,v) = E(u_n,v_n)C(u,v)\iint_{-\infty}^{\infty} S(u',v')\hat{V}_o(u',v')G(u'-u,v'-v)du'dv'.$$

The integral is once again a two-dimensional convolution, so in simplified notation

$$\hat{V}' = E\cdot C\left[(S\cdot V_o)\star G\right], \tag{3.6}$$

showing that the measured visibility points are smoothed, a weighted average formed, and then re-sampled onto the desired lattice. The symmetry of the lattice permits an exact transform to be taken:

$$B' = e\star c\star\left[(s\star B_o)\cdot g\right]. \tag{3.7}$$

The above two equations define the actual transformed quantities used in inversion. They are analagous to equations (1.5) and (1.6), and apply to any interpolation scheme in which the same smoothing function G is used over the entire visibility plane. Note that the true brightness distribution has suffered several modifications: 1) It has been smoothed by the synthesized beam and repeated on the interferometer grating pattern $(s*B_o)$. Subsequently it is 2) tapered by g, the Fourier transform of the smoothing function. This is a result of the smoothing of the visibility by G(u,v). Next it is 3) convolved with the weighting transform c(x,y). The effect of this operation is simply to correct for any non-uniformities in the sampling function S(u,v). This may be seen by considering C(u,v) to be the sum of an infinitely extended constant function of unity height plus a lumpy function, confined to the measured region of the visibility, whose amplitude at any point is the reciprocal of the (smoothed) local density of data samples. Its transform c(x,y) is then a delta function at the origin plus the transform of the lumpy function, which serves to de-convolve reciprocal lumps in the maps. To the extent that the sampling function is uniform, all weights are the same, and c(x,y) is of no importance. Finally, the modified brightness is 4) repeated on the new grating pattern e(x,y) caused by the regular lattice.

To avoid undue complications, the primary (single dish) beam attenuation of the source structure has not been considered here. However, since the effect of the dish is simply to smear the measured visibility points, it may be included in the smoothing function G. Also, in order to eliminate systematic phase shifts in the interpolation process, the visibilities are heterodyned so that the centroids of the brightness distributions are at x=0, y=0. After interpolation they are shifted back the same amount.

In order that the distortions effected on B_o be minimal, judicious choice of the interpolation parameters is required. In particular, to preclude severe tapering of the outer areas of the maps, the interpolation of the visibility should not include measured data far from the lattice points. Indeed, averaging should only occur over an area smaller than a unit cell. The smoothing function used was a Gaussian of 76 wavelengths full width at half height. (For comparison, the width of a 90-foot antenna is 130 wavelengths.) Secondly, the interpolation lattice E should be fine enough that the new grating pattern it introduces does not seriously contaminate the maps. The only limit on the fineness of E is computational efficiency. The grid used was square with points spaced 85 wavelengths apart, corresponding to a grating pattern of 40 arcmin extent. In general then, since the narrow-band sources are less than 20', adjacent lattice points contained some redundant information. Emphasis is placed on the fact that the original grating response due to discrete sampling by the interferometer remains, and is now repeated on the new grating pattern $e(x,y)$.

The alignment of the grid was somewhat unconventional. The usual arrangement is to have a lattice point at $u=0$, $v=0$. With this sampling, the total power, or d.c., information about the source is completely contained in the origin point. The source structure, or a.c. information, is determined by the remainder of the grid. Therefore in order to determine the total flux, the zero-spacing visibility must be measured or estimated. Small sources ameliorate this difficulty since 1) their visibilities fall off more slowly allowing reliable extrapolation to zero spacing, and 2) the region surrounding the source can be used to define a zero level. This grid alignment, although conventional, is not unique. If the lattice point separation is Δu, the completeness of the circular functions $\exp 2\pi i x \Delta u(n+p)$ for n integral and p any fraction ensure full representation of any source within the bounds $X=1/\Delta u$. Nonetheless, since data over half the (u,v) plane is obtained by invoking the Hermitian nature of the visibility, the only other alignment acceptable from the standpoint of symmetry is for $p=\frac{1}{2}$. However, for all arrangements other than $p=0$ the separation of a.c. and d.c. information no longer occurs. Since it was not anticipated at the beginning of this work that a zero-spacing spectrum would be available, the $p=\frac{1}{2}$ grid was adopted. In this way it was hoped that the zero level (necessary for the iteration procedure described in the next section) could be defined from the interferometer data alone. This would have been precisely true had the sources been small enough that data could have been taken at spacings of 100', 300', 500', etc. The d.c. content of the lattice points drops off from the center as $\frac{\sin\pi(n+p)}{\pi(n+p)}$. Therefore the largest contribution to the d.c. level arises from those lattice points closest to the origin, as one would expect. These points, at a radius of 60 wavelengths, are only poorly determined by the data, since a unit cell has a typical radius of 80 wavelengths. The result was that although a zero level was defined for the maps, it was missing much of the very low spatial frequency components. This became evident when the maps were integrated to produce spectra of the sources. The spectra fell below those published for NGC2403 (Roberts 1962a) and IC10 (Roberts 1962b; Epstein 1964a). For this reason the zero-spacing measurement described in the previous chapter was made, and the data reinverted.

3. Inversion and Iteration

In the inversion process it was decided to make use of the fact that the brightness distribution is positive. Several schemes to incorporate this information in the transform procedure have been tried (Biraud 1968; Dixon and Kraus 1968). The method employed here is similar to that described by Hogbom (1969) and is based on a program written by Rogstad (1970).

The interpolated visibility is first tapered and then inverted using the series (1.8). A section of the map containing the source is then examined for negative brightness temperatures below a test value (-1° K). These areas are reduced in amplitude (towards zero), and the modified brightness reinverted to produce a new visibility function. The weighted difference between this new visibility and the interpolated one is generated. Formation of the weighted difference is accomplished by multiplying the actual difference at the lattice points by the reciprocal of the function C(u,v) (equation 3.5). In this "difference visibility" function, only values exceeding measurement noise are kept. The difference function is reinverted to produce a "difference brightness" which is added to the original map. This process is repeated as often as desired. Intent of the procedure is to produce an almost-positive map whose visibility function differs from the one obtained from the data by amounts that are within the noise. At each iteration the average difference between the visibility being used at that point and the original visibility is computed and displayed.

It has not been possible to show that this procedure is always convergent. Experience has shown, however, that only in cases of very poor signal-to-noise does the iterated visibility diverge from the original (interpolated) function. For the maps produced in this work, all of which generated converging visibilities, the average difference at a lattice point was 0.05-0.07 flux units after five iterations. This should be compared with the 0.2 flux unit error in each measurement.

Once the final iteration is performed, a correction is made for the smoothing in the interpolation procedure. Referring to (3.7), it can be seen that if the artificial grating pattern $e(x,y)$ is a lattice of delta functions 40 minutes apart, and if the data has been uniformly sampled, then the corrected map (which is less than 40 arcmin in extent) is simply obtained by dividing the inverted map by $g(x,y)$. The correction, which is Gaussian, amounts to about a 20% increase 10 arcmin from the source centroid. Correction for the primary beam (see Figure 3) is then applied, amounting to about 50% for sources 10 arcmin from the origin of the maps (zero-phase point).

The smoothing correction described here is only an approximation because, even disregarding the new lattice responses $e(x,y)$, we must still contend with the convolution by $c(x,y)$. Dividing the maps by $g(x,y)$ is valid only to the extent that $c(x,y)$ is close to the delta function which obtains for a uniform data sampling. This simply reflects the intuitively obvious fact that in gridding we are sacrificing information which cannot later be recovered.

The correctional procedure was applied and is justifiable because 1) we have sufficient data that the smoothing function G can be made narrow, and consequently the correction is small, and 2) the data is relatively uniformly sampled (see Figures 1 and 2).

Unlike the transform relations given by (1.5) and (1.6), the practical relations (3.6) and (3.7) are no longer linear. In the idealized case, inversion of a synthetic point source visibility (for example, ones at all data points, phases all zero) gives s(x,y), the instrumental transfer function. The true brightness is merely convolved with this function. Similar procedure produces from (3.7) $e*c*(s\cdot g)$, a transfer function which is not simply an operator on the true brightness. This is to say that the transfer function is position dependent, a situation further aggravated by the iteration procedure. In order to estimate the variation of the transfer function over the map, several synthetic point sources were inverted, with and without iteration. These are shown in Figures 8 and 9. Position of the data points was the same as that of the observations. Beams in several locations are shown to demonstrate the nonlinearity of the transform procedure, i.e. the variation of the transfer function over the (x,y) plane. Since the data coverage for IC10 was substantially different from the other objects, synthetic beams for it are shown separately. A slight

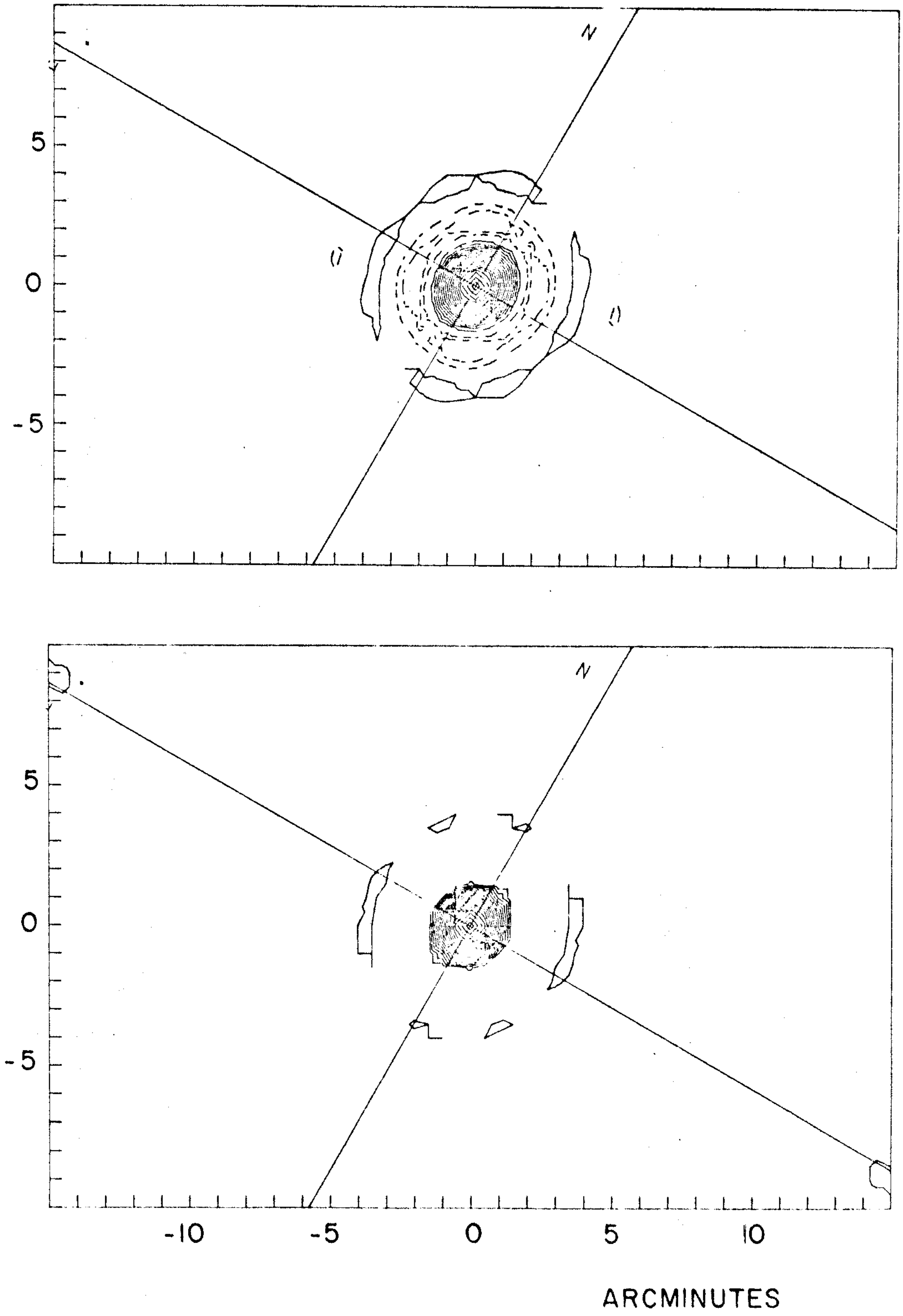

Figure 8. Synthetic beam pattern for NGC2403. (a) Without iteration. (b) With iteration. Contours are 5%.

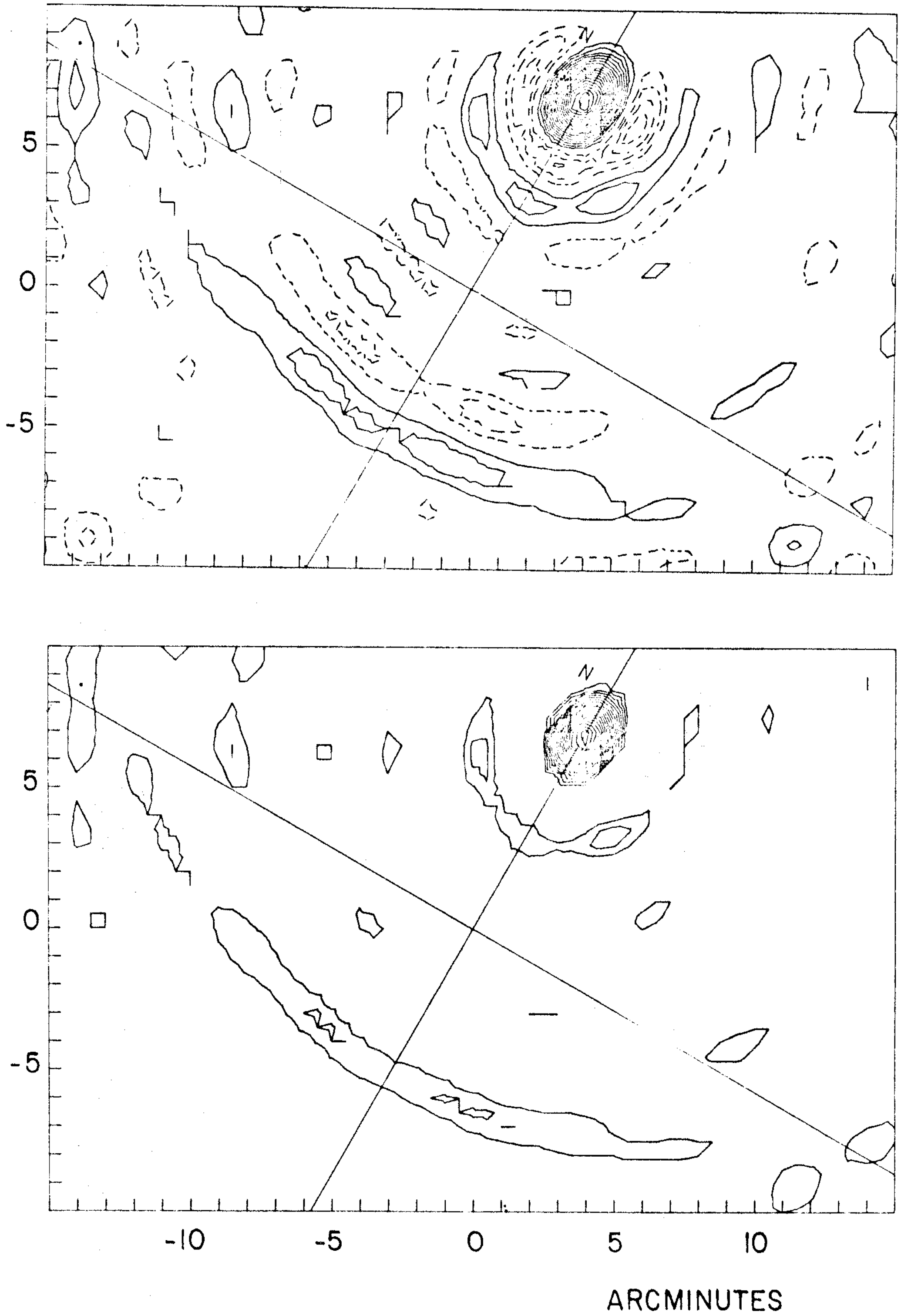

Figure 8 (continued). Synthetic beams for NGC2403 displaced 8' north. (a) Without iteration. (b) With iteration. 5% contours.

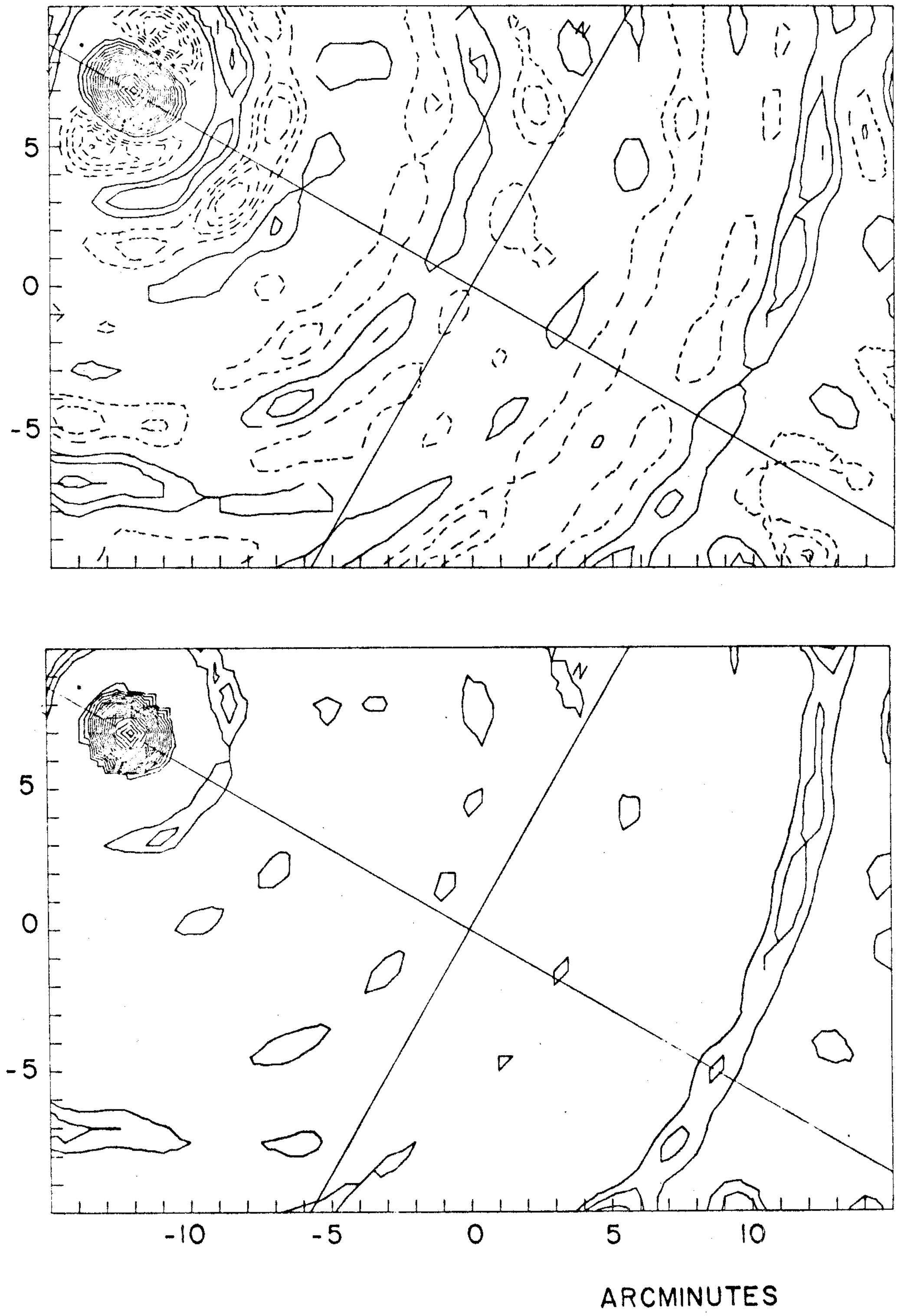

Figure 8 (continued). Synthetic beams for NGC2403 displaced 14' east. (a) Without iteration. (b) With iteration. 5% contours.

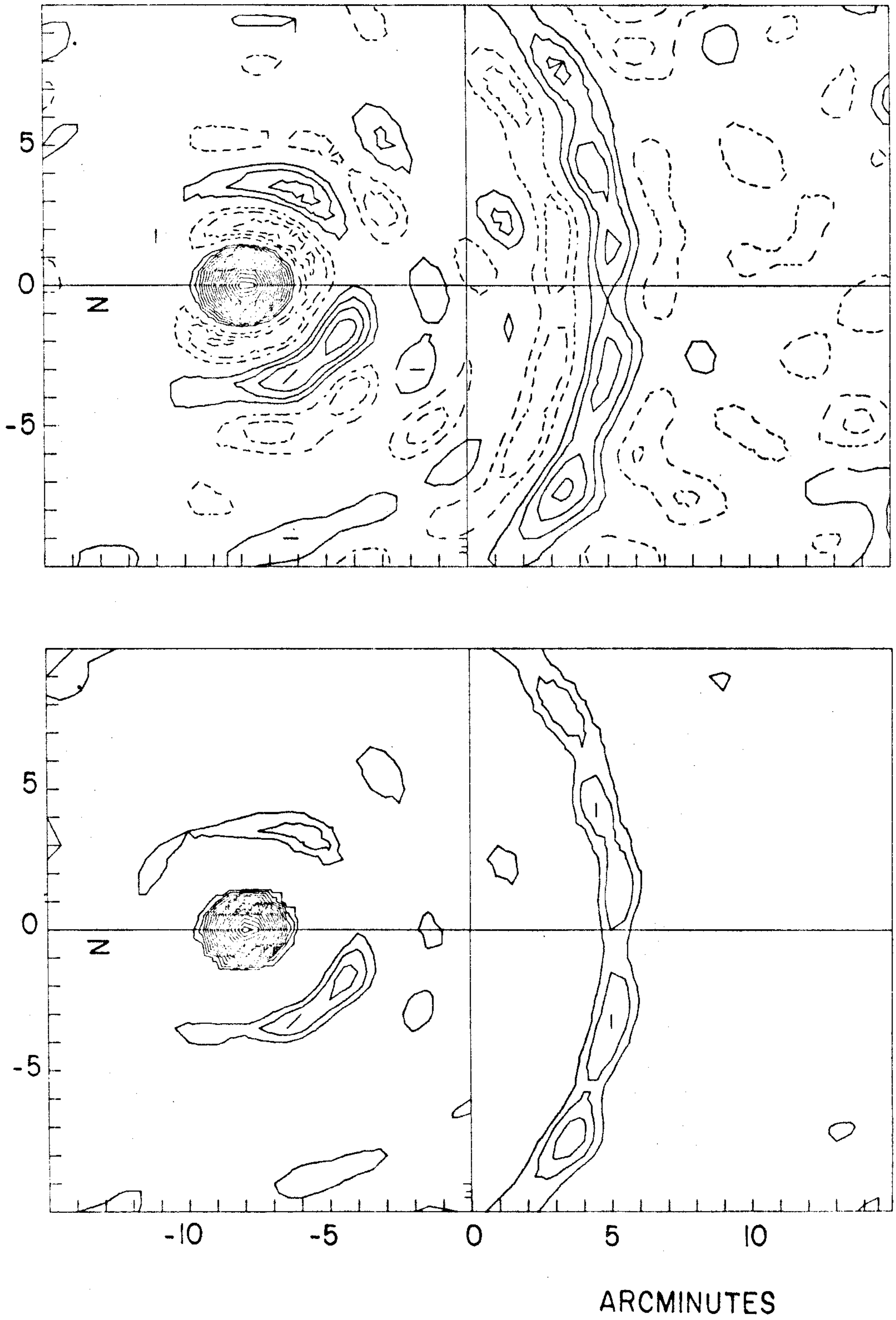

Figure 9. Synthetic beam patterns for IC10 displaced 8' north. (a) Without iteration. (b) With iteration. Contours are 5%.

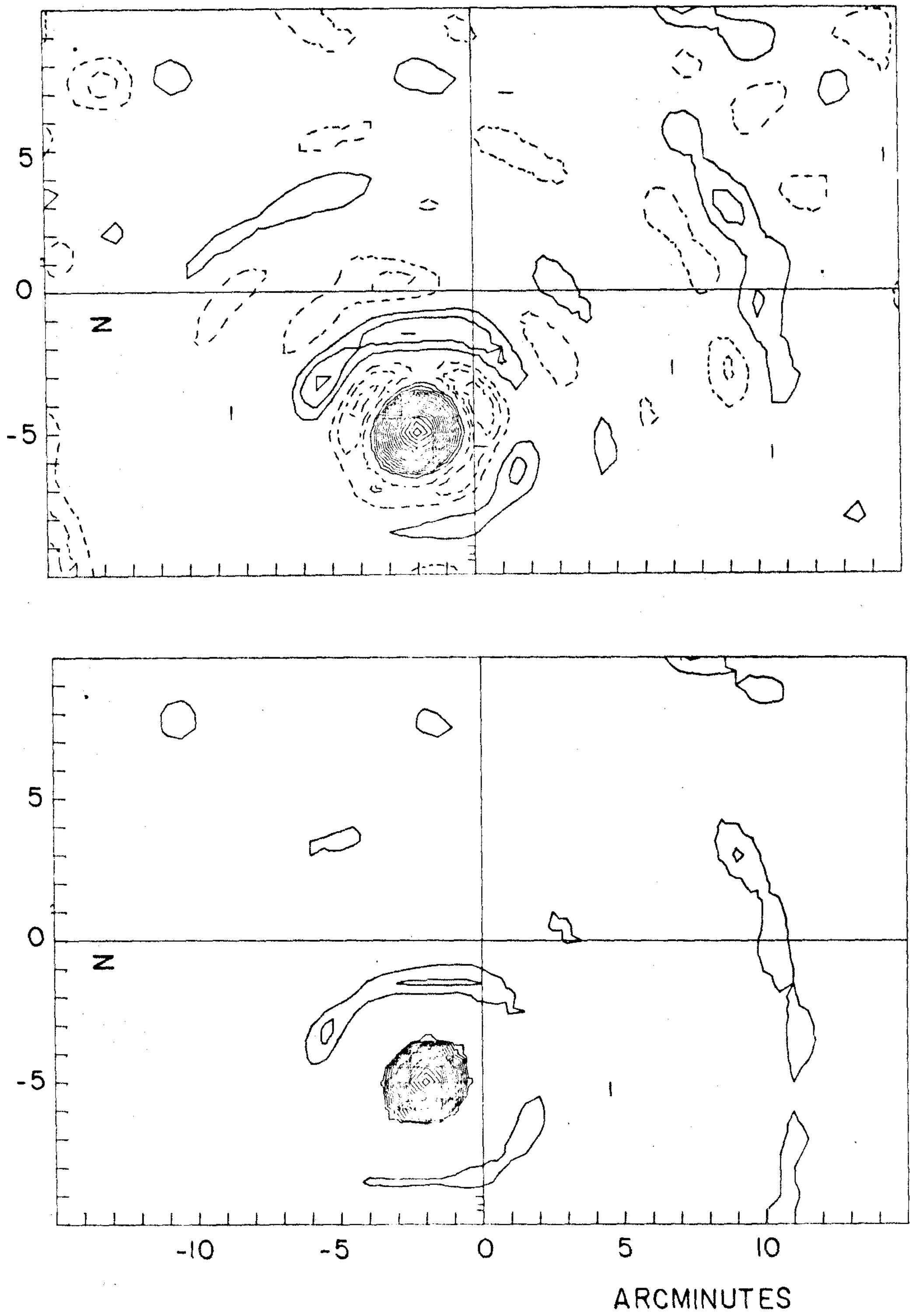

Figure 9 (continued). Synthetic beams for IC10 displaced 2' north and 5' east. (a) Without iteration. (b) With iteration. 5% contours.

tendency toward "squareness" in the patterns is caused by the plotting program. The relative invariance of the beams reflects the good data coverage in the (u,v) plane. Recall that the sources are phase-shifted before the interpolation procedure, so that the origin of these patterns corresponds to the centroids of the narrow-band maps. No taper has been used. The iteration procedure is seen both to sharpen resolution somewhat and to clean up the beams. Positive as well as negative sidelobes are reduced in amplitude.

4. Errors in the Maps

Contributors to errors in the synthesized maps may be categorized as 1) receiver noise, 2) calibration errors, 3) sidelobes, 4) accidental observation error, 5) systematic errors and long-term equipment changes, and 6) computation noise. The first two of these are most fundamental, and their effects were investigated in some detail.

We wish to determine the effect of uncertainties in the visibility function on the inverted map. For a single measurement the error in antenna temperature ΔT_a is

$$\Delta T_a = \frac{T_r}{\sqrt{\beta\tau}} \frac{1}{\sqrt{2}} , \qquad (3.8)$$

with T_r as the system noise temperature, β and τ the bandwidth and integration time respectively. Designating the primary dish beam area (steradians) by A_{dish}, this may be rewritten as an error in the measured flux

$$\Delta S = \frac{2k}{\lambda^2} \frac{T_r}{\sqrt{B\tau}} \frac{A_{dish}}{\sqrt{2}} . \tag{3.9}$$

Relating such errors in the measured visibility to uncertainties in the brightness is done by Fourier transforming an error visibility $\Delta\hat{V}(u,v)$. Using (1.8), the mean-square-error in the brightness is given by

$$\langle \Delta B^2 \rangle = \sum_{mnpq}\sum\sum\sum \langle \Delta\hat{V}^*(p\Delta u, q\Delta v)\, \Delta\hat{V}(m\Delta u, n\Delta v) \cdot e^{-2\pi i \left[(m-p)\Delta ux \;+\; (q-n)\Delta vy\right]} \rangle (\Delta u \Delta v)^2 . \tag{3.10}$$

We assume that the errors at different lattice points are uncorrelated in the mean. The brightness error reduces to a sum over the errors at the lattice points

$$\langle \Delta B^2 \rangle = \sum_{mn}\sum \langle \Delta\hat{V}^2(m\Delta u, n\Delta v) \rangle (\Delta u \Delta v)^2 . \tag{3.11}$$

Further simplification occurs if the lattice point errors are characterized by a single error $|\Delta\hat{V}|_{rms}$

$$\Delta B_{rms} = \sqrt{N}\; |\Delta\hat{V}|_{rms}\; \Delta u \Delta v , \tag{3.12}$$

where N is the total number of (measured) lattice points. Noting that the synthesized beam is

$$A_{synth} = \frac{1}{N\Delta u \Delta v} ,$$

and substituting ΔS as given by (3.9) for $\Delta \hat{V}_{rms}$ we have

$$\Delta B_{rms} = \frac{2k}{\lambda^2 E} \frac{T_r}{\sqrt{2\beta\tau N}} \frac{A_{dish}}{A_{synth}} . \qquad (3.13)$$

The additional factor E is the aperture efficiency, included to account for the fact that the measured data are not distributed exactly on the lattice points. An estimate of E was made assuming uniform distribution of data with Gaussian weighting to the lattice points, the resultant value being 0.6. If the visibility function had been tapered, some modification of E would be necessary.

Defining, then, the total observing time $t = N\tau$ and taking $\sqrt{2}\,E = 1$, we have

$$\Delta T_{B_{rms}} = \frac{T_r}{\sqrt{\beta\tau}} \frac{A_{dish}}{A_{synth}} , \qquad (3.14)$$

for the expected variation in brightness temperature. The total observing times for NGC2403 and NGC4236 were approximately 140 hours per object, that for IC10 being somewhat less. With a 150° receiver temperature and 100 KHz filters, the predicted noise is $T_{B_{rms}}=0.2°K$. Generally, features are considered real if they exceed four or five times the r.m.s. value.

The estimate derived from (3.14) is expected to be low, as it includes only receiver noise. In an attempt to ascertain the precision of the final measurements used in the inversions, the amplitudes and phases of the calibrator sources were examined. Since these amplitudes and phases are known (more precisely, are defined to be known), estimates of the inaccuracies in the calibrated data could be derived. A basic datum in the procedure was the fact that the uncalibrated uncertainty in amplitude for a 15 minute observation was 0.2 flux units. This is close to the 0.15 value predicted by (3.8). Any additional deviations from the calibrator's nominal flux must be ascribed to calibration error or accidental causes such as pointing error. It was assumed that accidental errors were infrequent and the principal effect was instrumental gain error, of magnitude proportional to the flux of the source. The effects of amplitude noise on phases can be obtained by considering the flux uncertainty to be normally distributed and of random phase. The resulting rather complicated distributions in measured phase can be found in Davenport and Root (1958). A useful approximation formula for that phase error for which the probability is one-half is

$$\Delta\phi_{\frac{1}{2}} = \frac{a}{1+a^2} + \frac{a^2}{\frac{2+a^2}{\pi}} \qquad \text{lobes,} \qquad (3.15)$$

where a is the fractional flux error. Use of this formula allows separation of noise-dependent and calibration-dependent errors in phase.

With these procedures the several contributors to uncertainty in the measurements could be untangled. In Table 5 are given typical values for these errors.

TABLE 5

Typical Errors in a Single Measurement

	Flux Error	Phase Error
Intrinsic:	0.2 f.u.	0.040 lobes at 1 f.u. 0.007 lobes at 5 f.u. (formula 3.15)
Calibration:	4% (proportional to flux)	0.020 lobes

Clearly calibration error is of no importance to amplitude values, but can be the dominant contributor to phase error at small spacings. Because of long term changes in equipment stability and configuration, calibration errors varied by as much as a factor of two from spacing to spacing.

To verify the accuracy of the estimate of ΔB_{rms} as predicted by (3.14), a Monte-Carlo type experiment was performed. The data from one channel for each galaxy, now defined to be "noise-free", had synthetic noise added to both fluxes and phases. The distribution of this noise was Gaussian with widths appropriate to the sum of the intrinsic and calibration errors for that spacing (c.f. Table 5). The modified data was then inverted in the usual way. Ten such maps were produced for each source and an average map generated. A distribution of the deviations of each map from the average was calculated. Mean value of the deviations was ~0.6°K. This is three times the value predicted by (3.14), and reflects the non-negligible effects of calibration and computational noise. As a further check, inspection of the off-line channels (with continuum sources removed) indicated average brightness variations of a similar magnitude. We adopt 0.6°K as the r.m.s. noise in the narrow-band maps.

The severity of beam sidelobes may be judged from Figures 8 and 9. The sidelobe level is typically $\lesssim$10%. Returning to the other sources of uncertainty, it seems reasonable to assume that the effects of gross observational errors are negligible in view of the large number of observations. The scaling uncertainty in the zero-spacing spectra discussed in Chapter 2, while substantially altering the integrated hydrogen in a given map, makes very little difference in the structure. Systematic errors in the measured visibilities could arise due to uncertainties in the fluxes and phases of the calibrators, particularly in view of the relatively small number of calibrators used for each object. However, as discussed in the previous chapter, comparisons with recent work indicate such uncertainties are substantially less than those due to receiver noise.

Short term shifts in the filter center frequencies will simply act to slightly increase their effective width. The relatively long-term drifts mentioned in Chapter 2 will cause some shifting of the high spatial frequency structure relative to the low, although this effect is small since the maps were almost always limited by spatial, rather than frequency, resolution. Computational noise, arising from gridding and iterating the data, is included in the sidelobe patterns of Figures 8 and 9.

In conclusion, then, receiver noise, calibration error and beam sidelobes are the major components of error in the narrow-band maps. The first two cause r.m.s. brightness variations of ~0.6°K, while sidelobe responses are $\leq$10% for NGC2403 and NGC4236 and $\leq$15% for IC10. All values refer to regions near the centers of the galaxies and must be increased by the primary beam restoring correction outside these regions. At 10' radius, the restoring factor is 1.5.

IV. THE MAPS

1. Positions of Galactic Centers

The optical galactic center positions were estimated by inspection of Palomar Sky Survey prints. The adopted values, listed in Table 6, are close to those found by others (c.f. de Vaucouleurs 1964). In any event, their accuracy is of little importance as they are merely used to define the zero-phase points of the present observations. The scales on the narrow-band maps found later in this chapter have these positions as their origins.

TABLE 6

Adopted Zero-Phase Positions

Object	(1950)	(1950)
NGC2403	07^{h} 32^{m} $05\overset{s}{.}4$	65° $42'$ $42\overset{''}{.}0$
NGC4236	12 14 24.2	69 44 40.0
IC10	00 17 36.0	59 02 40.0

2. Subtraction of Continuum Sources

Several previous studies (Epstein 1964a; Heeschen and Wade 1964; Rogstad <u>et al</u>. 1967) have revealed the existence of continuum radiation from all three synthesis objects. Since this radiation is present in the hydrogen channels, some procedure was necessary to remove it. The broad-band channel (~5MHz width) was rather substantially contaminated by the line radiation, and it was therefore decided to determine the continuum sources by use of the off-line channels. Because of the wide frequency coverage of the filter bank (2.3 MHz), 8 to 12 channels could be averaged to define the continuum visibility. The real and imaginary parts of this visibility were subtracted from the corresponding parts of the hydrogen channel visibilities before the latter were transformed.

There is an approximation inherent in this procedure; namely that interaction of continuum and line radiation is negligible. The source obtained by averaging the off-line channels is obviously unabsorbed, but if some attenuation of this source occurs in the line, the narrow channel maps obtained by the foregoing procedure will be depressed by the amount of the absorption. One can easily see from the transfer equation (Chapter 5) that the fractional depth of this depression is $\sim T_{BC}/T_s$, where T_{BC} is the continuum brightness temperature and T_s is the harmonic mean hydrogen spin temperature. The depression is inconsequential since the observed values of T_{BC} are $\leq 2.5°K$ for NGC2403 and NGC4236, and $\leq 8°K$ for IC10, much less than the expected spin temperatures. For the latter two objects the continuum emission is confined to a small central region, and therefore most channels are not even affected by the small absorption effect discussed here.

The averaged continuum visibilities were inverted to produce the maps shown in Figures 10, 11 and 12. For NGC2403 and NGC4236 the contour interval is 0.5°K; for IC10 it is 1.0°K. It was shown in Chapter 3 that the r.m.s. brightness variation in a 100 kHz channel due to receiver and calibration noise was ~0.6°K. Using this value, the confidence level (five times r.m.s.) in the continuum maps is ~1.0°K. (Note that approximately 10 narrow-band channels are averaged to produce the continuum maps.) Many bumps of approximately this value can be seen in the maps and, of course, should be disregarded. For NGC2403, which is the only object with substantially extended continuum emission, several of the bumps appear to be connected with the stronger central regions and their reality therefore remains an open question. De Jong (1966) has noted the presence in several spirals of "satellite" continuum sources which he suspects are associated with the galaxies.

The integrated continuum flux, useful for determining spectral indices when measurements at other frequencies are available, was obtained for each object by integrating the respective maps. (No zero-spacing continuum fluxes

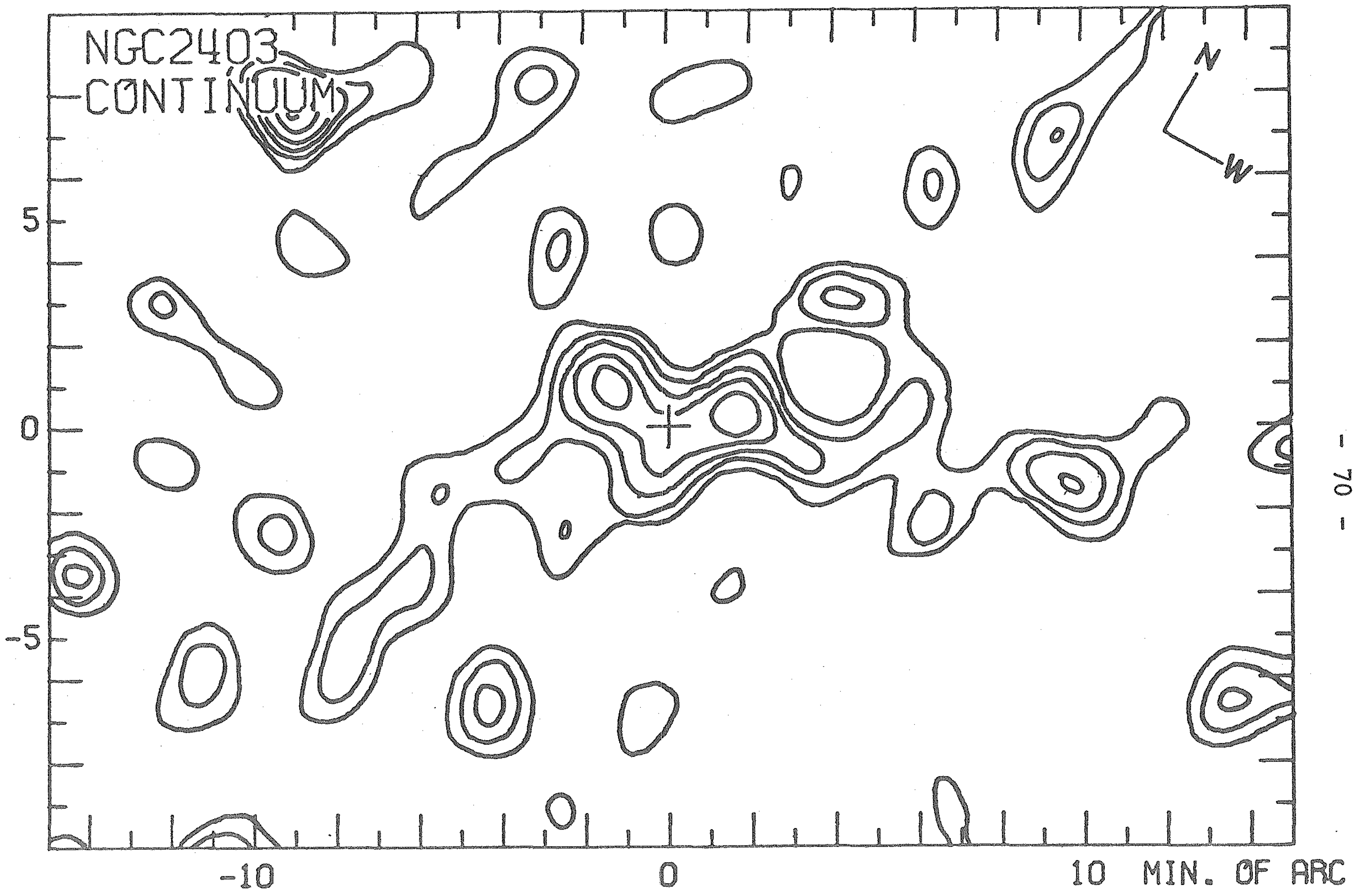

Figure 10. Continuum map for NGC2403. Contour interval is 0.5°K.

Figure 11. Continuum map for NGC4236. Contour interval is 0.5°K.

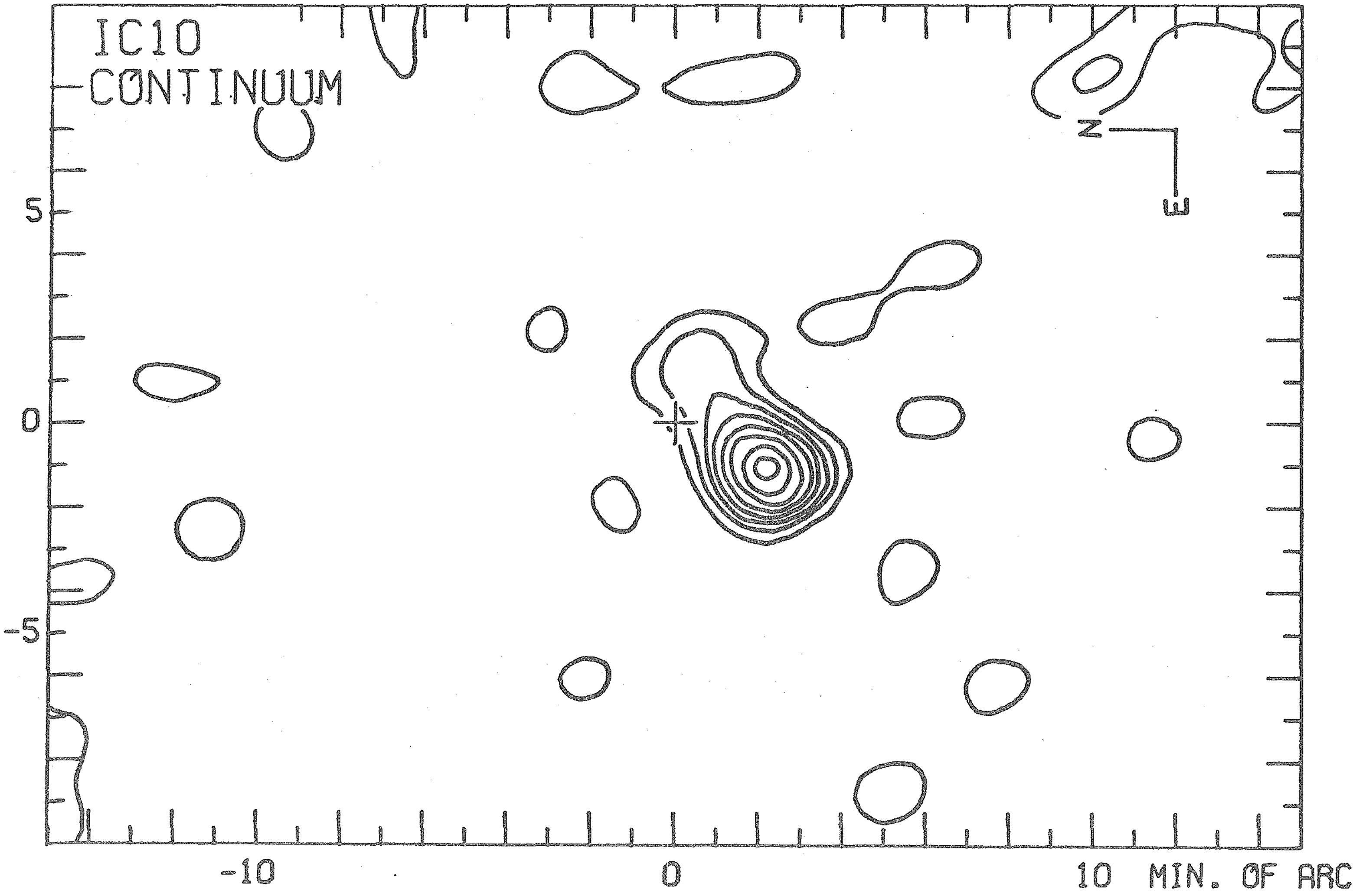

Figure 12. Continuum map for IC10. Contour interval is 1.0°K.

were measured.) For NGC2403 this integral may be a slight underestimate because of resolution effects. The values are listed in Table 7, along with those found by others. The most serious discrepancies occur between the values of the present data and those of Rogstad *et al.*, particularly in the case of NGC4236. It is felt that contamination of the broad-band channel by HI emission accounts for the larger fluxes reported by those authors. For example, using the integrated HI line profile for NGC4236 (see Figure 7) one would expect to measure ~0.7 flux units in a 5 MHz channel, even without a continuum source.

TABLE 7

1420 MHz Continuum Fluxes
(flux units)

	NGC2403	NGC4236	IC10
Heeschen and Wade	0.3a	0.3	--
Epstein	1	--	0.6
Rogstad *et al.*	0.2b	0.63	0.75
Present study	0.5	0.044	0.30

Notes: a) This value assumes a point source and is therefore a lower limit.

b) Confusion limit.

The errors in the listed fluxes depend, of course, on the accuracy with which the source boundaries could be defined. For NGC4236 and IC10 only the small, centrally-located sources were considered real; the integration error is then ~0.01 f.u. Nearly all the sources contiguous with the central emission region were included in the integration for NGC2403, and the estimated uncertainty due to this procedure is ~0.1 f.u. Correlation of the continuum distributions with optical features of the galaxies is discussed in Chapter 5.

3. Confusion

Since the continuum radiation was synthesized and subtracted from the hydrogen channels as discussed above, confusion due to continuum sources was eliminated. An example of a potentially confusing object can be seen in the eastern corner of the NGC2403 continuum map (Figure 10). The strength of this source is ~0.05 flux units.

Galactic hydrogen confusion was not anticipated for IC10 due to its large systemic velocity. However, both NGC2403 and NGC4236 have hydrogen emission near 0 km-s^{-1} and were therefore subject to this type of error. The galactic longitudes of these objects, respectively $l^{II}=95°$ and 127°, occur in the quadrant in which confusing hydrogen would be expected to have mildly negative velocities.

Emission line profiles measured near the position of NGC2403 ($b^{II}=12°$) have a typical width of ~30 km-s^{-1} centered at -20 km-s^{-1} (Muller and Westerhout 1957; Weaver and Williams 1971). Thus, only the extremum channel centered at -3 km-s^{-1} is likely to be affected. This is confirmed by the zero-spacing measurement of Section 2.4 which shows disruption of the spectrum in the same velocity range as the aforementioned published surveys. Unfortunately, because of the subtraction of comparison fields employed in obtaining this spectrum, Galactic emission is, to first order, cancelled out. The residual disruption, amounting to ~10 f.u., is an upper bound on the amount of Galactic emission having structure of a size comparable to or smaller than the beamwidth (24'). A further size limitation is imposed by the interferometric observations of Hughes, Thompson and Colvin (1971) in which they report emission of $\leq$ 6 f.u. with a 200-foot baseline. (These values refer to a survey involving ninety-seven sources scattered over much of the visible sky.) It is clear from these data that the Galactic hydrogen emission has a large-scale smoothness with no appreciable structure smaller than ~6 - 10'. Structure larger than 24', the largest fringe spacing of the present synthesis, is of no consequence since it will not appear in the maps. (Zero-spacing fluxes at the confusion velocities were not used as measured. An interpolated value, judged by the amplitude of neighboring channels, was used to set the d.c. level of the maps. Error in this value is expected to be of negligible importance.) If, using the above results, we consider the typical Galactic emission region in the neighborhood of NGC2403 to be 15' in diameter with an integrated flux of 5 f.u., the expected brightness temperature is ~4°K. This corresponds to the lowest contour plotted on the narrow-band maps. In fact the actual situation seems far better than this; the measured flux in the -3 $km\text{-}s^{-1}$ channel never exceeded 1.5 f.u. (c.f. Seielstad and Whiteoak 1965; Figure 3).

Similar arguments hold in the case of NGC4236, although the expected emission should be less because of its higher Galactic latitude ($b^{II}=47°$). The velocity and extent of the potentially confusing hydrogen are essentially the same as for NGC2403. Observationally, the amplitude of the -22 $km\text{-}s^{-1}$ channel was always less than 2.5 f.u.

The ultimate test for the effects of Galactic confusion is inspection of the maps themselves. In this regard they seem remarkably free of any unusual features or asymmetries suggestive of confusion.

4. The Narrow-Band Maps

The individual channel maps for NGC2403, NGC4236, and IC10 are displayed in Figures 13 through 15. Contours are at intervals of 400^0K-kHz (=84°K-km-s^{-1}) except for certain extremum channels of NGC4236 and IC10 where the interval is one-half this value. Brightness temperatures are obtainable by dividing by the bandwidth (100kHz = 21 km-s^{-1}). Zero level contours are not plotted.

Relevant parameters for the maps are summarized below:

Resolution: 2 arcmins, half-power.

Position angle of maps:		
	NGC2403 ---	120°
	NGC4236 ---	160^0
	IC10 ---	-90^0.

Noise level (5 times r.m.s.): 300^0K-kHz.

Sidelobe amplitude:		
	NGC2403	<10%
	NGC4236	<10%
	IC10	<15%

Map origins: as listed, Table 6.

Filter centers: marked on maps in km-s^{-1} with respect to sun.

These maps comprise the fundamental data of the present study. In the following two chapters they are combined to produce the total hydrogen distributions and radial velocity fields for the three synthesized objects.

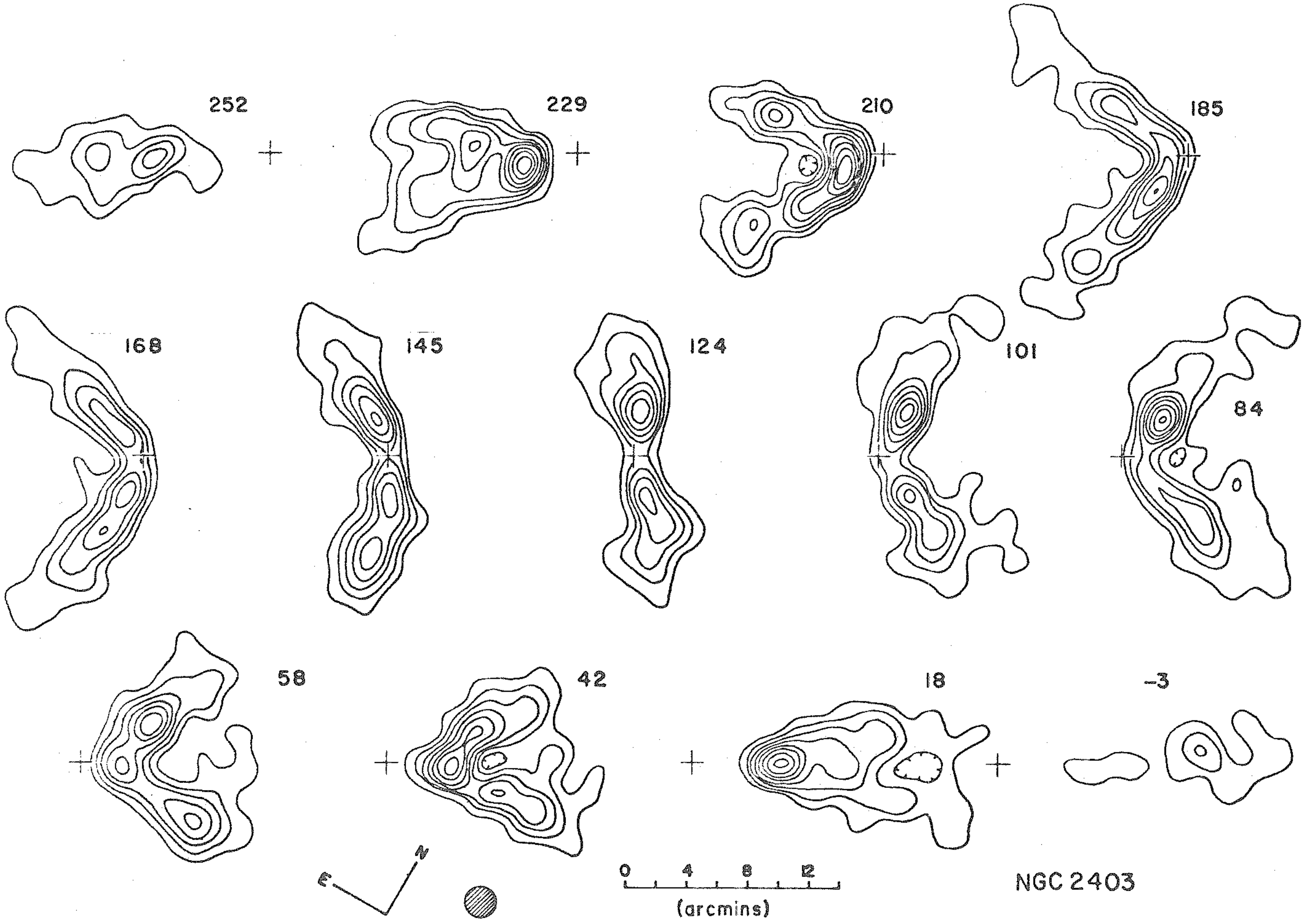

Figure 13. Narrow-band maps for NGC2403. Contour interval is 400°K KHz (84 °K-km-s^{-1}). Nominal radial velocities for each filter are indicated.

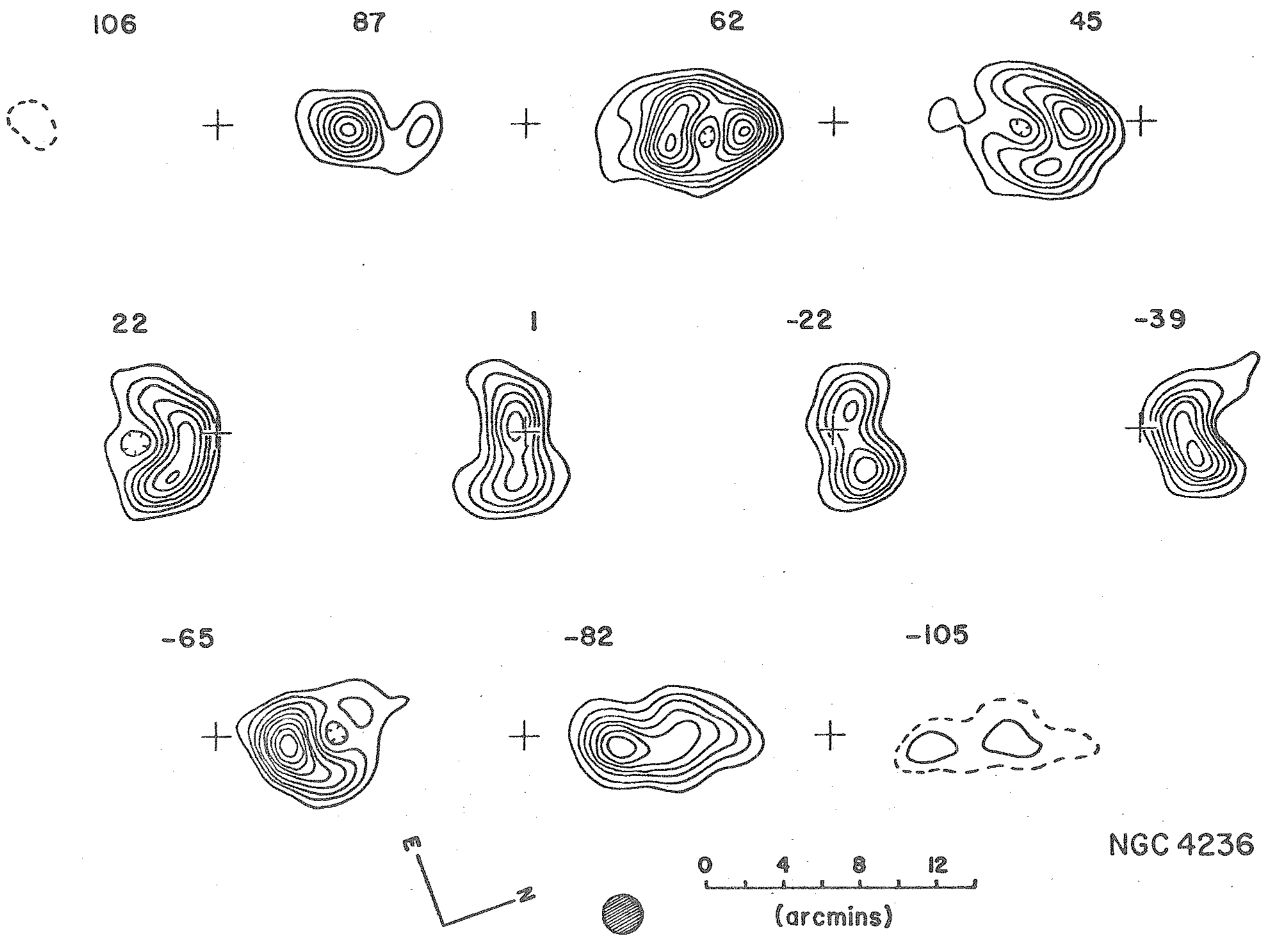

Figure 14. Narrow-band maps for NGC4236. Contour interval is 400^{o}K-KHz (84 °K-km-s^{-1}). Dotted contours are at half this value. Nominal radial velocities for each filter are indicated.

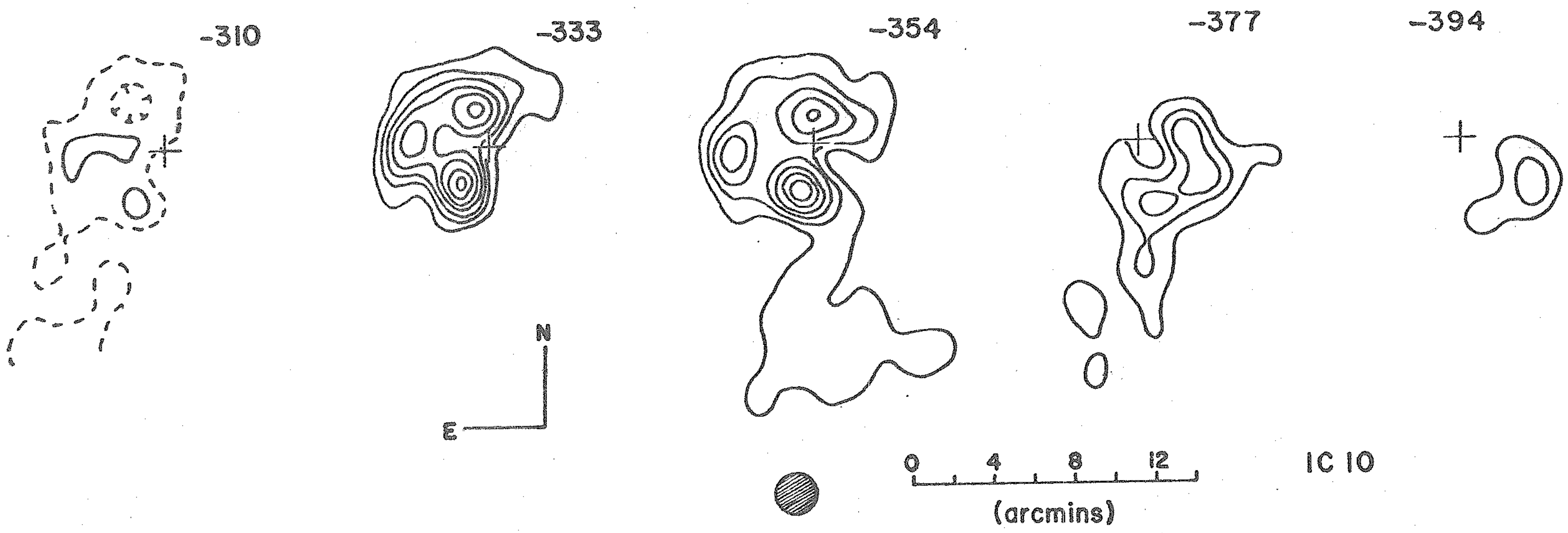

Figure 15. Narrow-band maps for IC10. Contour interval is 400°K-KHz (84 °K-km-s^{-1}). Dotted contours are at half this value. Nominal radial velocities for each filter are indicated.

V. HYDROGEN CONTENT AND DISTRIBUTION

1. Line Formation and Transfer Equation

The 21-cm line is a forbidden magnetic dipole transition between two hyperfine states of neutral atomic hydrogen. Although it has a very low transition probability, it can readily be detected because of the long paths involved in observations of interstellar hydrogen. Existence of the line was first predicted by van de Hulst (1945) and Shklovsky (1949).

Although densities are low, Purcell and Field (1956) and Field (1958) have shown that most transitions of HI are collisional and non-radiative. This thermalizing of the interstellar gas allows us to invoke local thermodynamic equilibrium; we characterize the relative population of the excited and ground states by the Boltzmann equation

$$\frac{N_2}{N_1} = \frac{g_2}{g_1}\, e^{-h\nu/kT_s} \, . \tag{5.1}$$

The statistical weights g_2 and g_1 are respectively 3 and 1. T_s is the excitation (spin) temperature, and is close to the local kinetic temperature except under conditions of extremely low density or high radiation intensity.

Since we wish to relate the observed brightness temperatures to the number of hydrogen atoms in the line of sight, we solve the transfer equation for the emergent intensity in the line

$$\frac{dI}{ds} = -(\kappa_L + \kappa_C)I + (\varepsilon_L + \varepsilon_C). \qquad (5.2)$$

The absorption and emission coefficients (κ and ε, respectively) are separated into their line and continuum values. The formal solution of this equation is simplified by introducing the optical depths

$$\tau_C(s,s') = \int_{s'}^{s} \kappa_C d_s,$$

$$\tau_L(s,s') = \int_{s'}^{s} \kappa_L d_s, \qquad (5.3)$$

so that

$$I(s) = I(o)e^{-\left[\tau_C(s,o) + \tau_L(s,o)\right]}$$

$$+\int_{o}^{s} \left[\varepsilon_L + \varepsilon_C\right] e^{-\left[\tau_C(s,s') + \tau_L(s,s')\right]} ds'. \qquad (5.4)$$

Further reduction of this formula occurs if we take $I(0)=0$ and note that $\kappa_C \ll \kappa_L$. Also, since local thermodynamic equilibrium obtains in the line, the emission coefficient ε_L is related to κ_L by Kirchoff's law

$$\varepsilon_L = \kappa_L B(T), \qquad (5.5)$$

where B is the Planck function. Rewriting equation (5.4) in terms of brightness temperature T_B,

$$T_B(s) = \int_0^s \left[\kappa_L T + \frac{\lambda^2}{2k}\,\varepsilon_C\right] e^{-\tau_L(s,s')} ds' . \tag{5.6}$$

The Rayleigh- Jeans formula has been used to approximate B(T). Defining a mean optical depth

$$e^{-\bar{\tau}} = \frac{\int_0^s \varepsilon_C e^{-\tau_L} ds'}{\int_0^s \varepsilon_C ds'} , \tag{5.7}$$

and assuming homogeneity of the region producing the line radiation (i.e. κ_L and T are independent of s), then

$$T_B = T(1-e^{-\tau_L}) + T_{BC}e^{-\bar{\tau}} , \tag{5.8}$$

where T_{BC} is the brightness in the continuum. For galaxies which are not too greatly inclined to the line of sight, the assumption $\tau_L \ll 1$ is generally made. This assumption can in principle be partially verified for galaxies which have continuum sources by considering observed brightnesses in and out of the line and using equation (5.8) to solve for τ_L. As a practical matter, none of the three objects encompassed by this work had a continuum flux large enough to allow this test to be made.

For the optically thin case, and with $T \gg T_{BC}$

$$T_B = T\tau_L. \tag{5.9}$$

Since the emitting region is taken to be homogeneous, τ_L in the above expression is simply $\kappa_L S$, where S is the path length through the region. It remains, then, to relate κ_L to the hydrogen density. We briefly discuss how this is done:

Consider the emission coefficient to be solely dependent on spontaneous emission; stimulated emission is more correctly treated as negative absorption. Then

$$\varepsilon_L = N_2 A_{21} \frac{h\nu}{4\pi} p(\nu), \tag{5.10}$$

where A_{21} is the probability of an emission and $p(\nu)$ is the probability that the observed frequency lies between ν and $\nu + d\nu$. Using the Kirchoff relation and the Rayleigh-Jeans formula we have

$$\kappa_L = \frac{N_2 A_{21} h c^2 p(\nu)}{8\pi k T \nu}. \tag{5.11}$$

Finally, with $kT_S \gg h\nu$, we can use equation (5.1) to express N_2 in terms of the total number density of hydrogen atoms N,

$$N_2 \approx 3/4\ N. \tag{5.12}$$

Relation (5.9) becomes

$$T_B = \frac{3A_{21}hc^2NS}{32\pi k\nu}\, p(\nu). \qquad (5.13)$$

Since the line has practically zero width, $p(\nu)$ is solely the result of Doppler broadening. In velocity units

$$T_B = 5.44 \times 10^{-19}\, N(V)S \ ({}^0K), \qquad (5.14)$$

where N(V)S is the number of HI atoms in the line of sight (no.-cm^{-2}) with velocities between V and V+dV km-s^{-1}. To the extent that the assumptions leading to this relation are justified (see below), it is fair to interpret the narrow-band and total hydrogen maps as depicting HI surface densities.

Another useful formulation of equation (5.14) is the expression for optical depth in the line (for small τ)

$$\tau = 1.67\, \frac{\rho S}{T\Delta V}, \qquad (5.15)$$

in which ρ is the hydrogen density (atoms-cm^{-3}), S is the path length in parsecs and ΔV is the velocity width in km-s^{-1}.

2. Total Hydrogen Masses

The total neutral hydrogen content of the objects is obtained either by summing the narrow-band maps or by integrating the zero-spacing velocity profile. The latter approach is simpler and does not suffer from inversion noise, overlapping filters, etc. For a profile which has not suffered beam attenuation (or, as is the case here, has been suitably corrected) equation (5.14) may be integrated to yield

$$M_{HI} = 2.37 \times 10^{5} \; D^{2} \int F(V)\,dV \quad \text{(solar masses)} \qquad (5.16)$$

where F(V) is the profile amplitude in flux units and D is the distance in megaparsecs.

The profiles presented in Chapter 3 were integrated and the hydrogen masses computed as above. The masses are listed in Table 8 along with values obtained by others. All values have been corrected to common distances indicated in the table.

The uncertainty in the masses derives from several sources. For NGC4236 and IC10 the most important effect is probably the uncertainty in their distances, as these are squared when computing the masses. There is an estimated 20% uncertainty in the integrated velocity profile for all objects due to the scaling difficulties discussed in Chapter 3.

TABLE 8

Observed HI Masses

NGC2403			
	4.6	$\times 10^9\ M_\odot$ at 3.2 Mpc	(Roberts 1962a)
	3.3	"	(Guelin and Weliachew 1969)
	3.5	"	present study
NGC4236			
	1.5	$\times 10^9\ M_\odot$ at 3.2 Mpc	present study
IC10			
	1.8	$\times 10^9\ M_\odot$ at 3.0 Mpc	(Epstein 1964a)
	1.8	"	(Roberts 1962b)
	0.91	"	(Gouguenheim 1969)
	1.0	"	present study

Aside from these considerations, there is the more fundamental question of the applicability of equation (5.14) and of equation (5.16) which is derived from it. Primarily we are concerned with the small τ assumption. In our own Galaxy, the disparity between wide emission profiles and relatively narrow absorption profiles suggests that the interstellar HI consists of a least two components (Clark 1965) at very different temperatures. The hot component, found between spiral arms, has a temperature which is probably no less than 300°K, and may be several thousand degrees (Quirk 1971). This component will be optically thin in most circumstances. Within the arms are found massive clouds whose temperatures are ~70°K (Hughes, Thompson and Colvin 1971). The observed frequency of occurance of maximum optical depths is an exponentially decreasing function with increasing depth (op. cit.), so that the average value of τ_{max} is 1.0. Since the correction to the mass given by equation (5.16) is $<\tau>/(1-e^{-<\tau>})$ for non-negligible τ, an increase of 60% in the mass of the arm material is suggested. Actually this is an overestimate since $<\tau>$ will be less than $<\tau_{max}>$. Furthermore, since average interarm densities are not too much different from those within the arms (Quirk 1971), certainly less than half of the total HI of the Galaxy is in the cool component. To the extent that these arguments are applicable to the external systems studied here, we expect a "face-on" increase in the total hydrogen masses of less than 30% over the observed values.

One expects an additional increase in HI mass due to inclination effects. Epstein (1964b) has considered this problem employing simple galactic models to find average optical depths. The models have solid-body rotation and uniform spin temperatures. For an inclination of 75^0 (that of NGC4236), he finds $<\tau> = 1.0$, assuming $T_s=125^0$ K. For the hot component of a two-temperature gas, this effect becomes negligible for inclinations $\leq 75^0$, since τ is scaled by T_s^{-1}. Because the cold gas is found in discrete clouds, each with its own peculiar velocity, the homogeneity assumption is invalid and Epstein's analysis does not apply. The only inclination-dependent effect of the clouds, which in our own Galaxy are restricted to a thin (~200 pc) layer (Hughes _et_ _al_. 1971), will be to block emission in relevant velocity ranges originating behind them. One expects this effect to have a general dependence of the form $(1 - f \cdot \sec i)$, where f is the fraction of HI emission being hidden in the face-on orientation. Although the data are only tentative, Roberts' (1969) plot of hydrogen mass-luminosity ratio versus inclination for external systems suggests a value for f of ~0.15.

In summary, then, we find two types of corrections to the observed HI masses: 1) A face-on correction due to optically thick hydrogen in cold clouds, amounting to an increase of ≤ 0.6 times the fractional HI mass in clouds, and 2) an inclination correction of ~0.15 sec i. Because of their uncertain nature, neither of these corrections has been applied to the values of Table 8. The indicated increases are greatest for NGC4236, but because of its barred geometry, these may not be entirely justified. Suffice it to say that Table 8 lists lower limits to the HI masses, the degree of underestimation being as much as a factor of two, distance considerations aside.

3. Total Hydrogen Distribution

The total hydrogen distributions may be obtained from the narrow-band maps of Chapter 4 in several ways. One might 1) add the various channel visibilities and then invert, 2) integrate interpolated line profiles at each point on the object, or 3) add the narrow-band maps. To a first approximation all these methods are equivalent, and further consideration will reveal that all are subject to the same inaccuracies (although method 1 introduces additional unwanted effects due to the non-linearity of the Fourier transform process and does not allow discrimination against noise in the summing procedure). The simplest approach, and the one used here, is to approximate the integrated hydrogen by a weighted sum of the channel maps

$$B_{TOT}(x,y) = \sum_n a_n B_n' (x,y). \tag{5.17}$$

Here B_n' is the brightness distribution for channel n. It is shown in Chapter 6 (equation 6.2) that B_n' is related to the true three-parameter object brightness $B(x,y,V)$ by

$$B_n'(x,y) = \beta(x,y) * \int_{-\infty}^{\infty} B(x,y,V) f_n(V) dV, \tag{5.18}$$

where β is the synthesizing beam and f_n is the normalized power response of the n'th filter. Therefore

$$B_{TOT}(x,y) = \beta(x,y) * \int_{-\infty}^{\infty} \sum_n a_n f_n(V) B(x,y,V) dV, \tag{5.19}$$

from which it is obvious that the summed distribution will equal the true (beam-convolved) distribution when the weights are chosen so that

$$\sum_n a_n f_n (V) = 1. \tag{5.20}$$

Because the shapes and spacing of the filters are given quantities, exact equality in the above relation is not possible. A computer program making a least-squares solution for the best a_n produced the response shown in Figure 16. Here the summed response is plotted against IF frequency; the local oscillator was adjusted so that the estimated systemic velocity of the galaxies corresponded to 10 MHz.

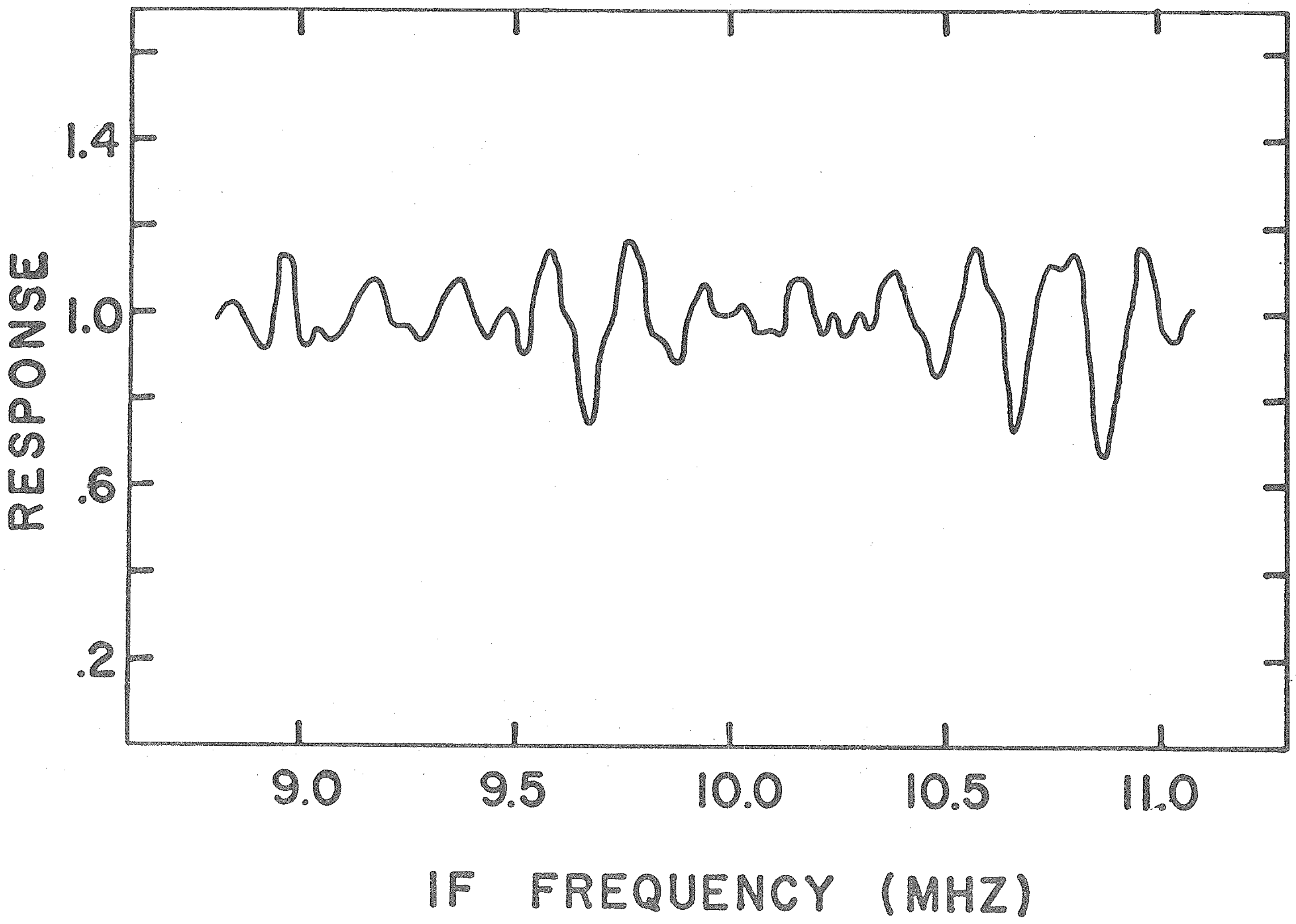

Figure 16. Frequency response of summed narrow-band filters. Systemic velocities correspond to an IF frequency of about 10 MHz.

The response curve is seen to have irregularities as large as ~0.25, although the anticipated deviations in the summed maps would hardly be this large since in most regions the galaxy line profiles are considerably wider than the irregularities. A better measure of the uncertainty in the summed maps caused by the lack of smooth response in the velocity domain is given by the standard deviation of the response curve. This amounts to 10% over the entire filter bank (8.8 to 11.1 MHz), but only 8% over the region in which hydrogen was detected.

The weighted sums of the narrow-band maps of Chapter 4 are shown in Figures 17 through 22. Only regions having a brightness greater than 300^0K-kHz (~noise level) were included in the sum to avoid adding noise. The contour increment of the maps is 600^0K-kHz (127°K-km-s^{-1}); the zero level contour is not plotted. This corresponds to a columnar HI density increment of 2.34×10^{20} H atoms-cm^{-2}. Conversion to surface density in the galactic planes requires multiplication by the cosine of the inclinations, respectively 0.50, 0.26 and 0.87 for NGC2403, NGC4236 and IC10. The inclination for NGC2403 (60^0) is obtained by symmetrizing the velocity field as described in Chapter 6. For NGC4236, a value of 75^0 was taken from de Vaucouleurs (1964). The inclination of IC10 (30^0) is deduced later in this chapter. Propagation of errors due to noise in the channel maps and irregularities in the velocity response indicate a

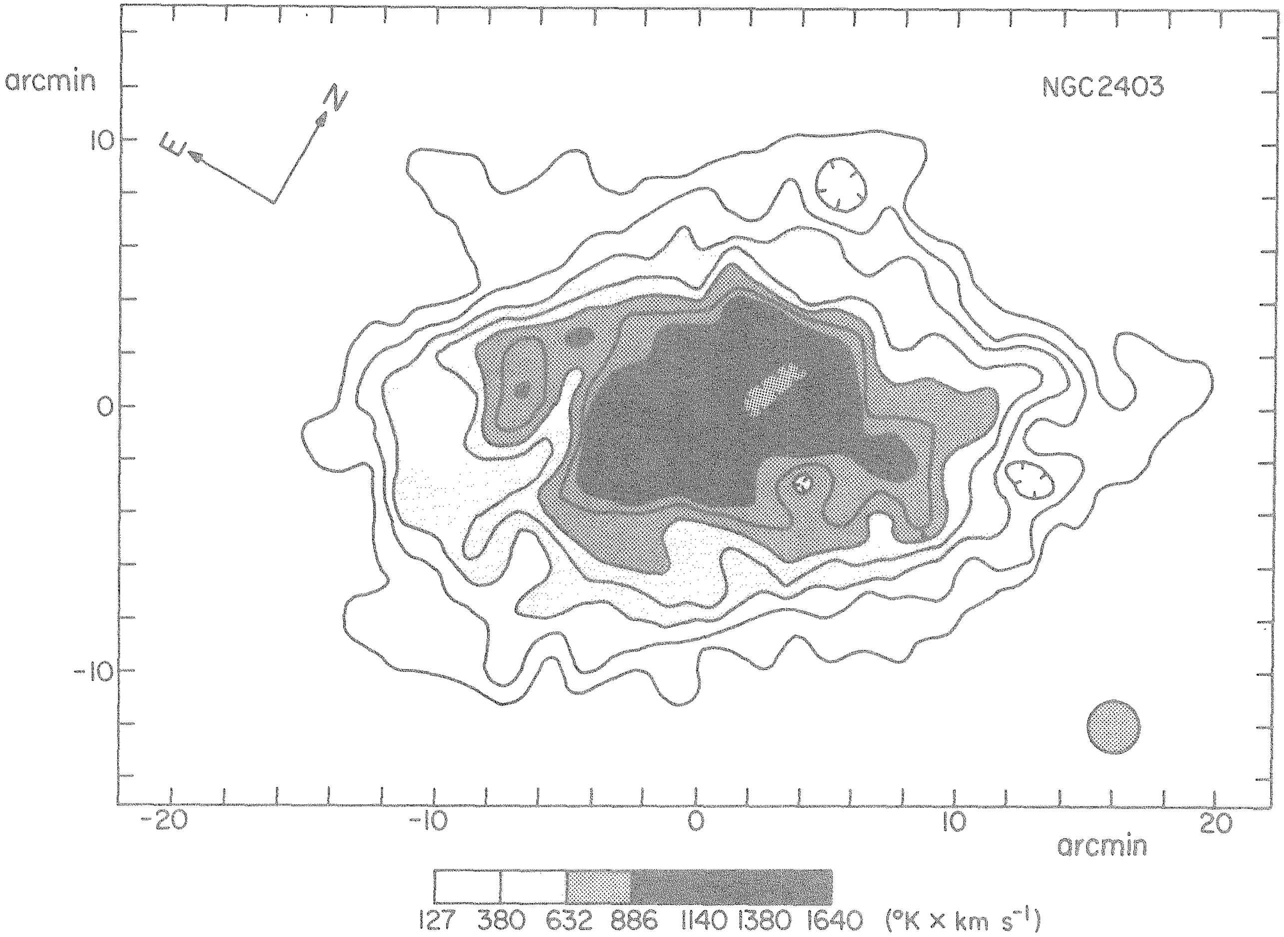

Figure 17. Integrated hydrogen map of NGC2403. Contour increment corresponds to line-of-sight density of 2.34×10^{20} at.-cm^{-2}.

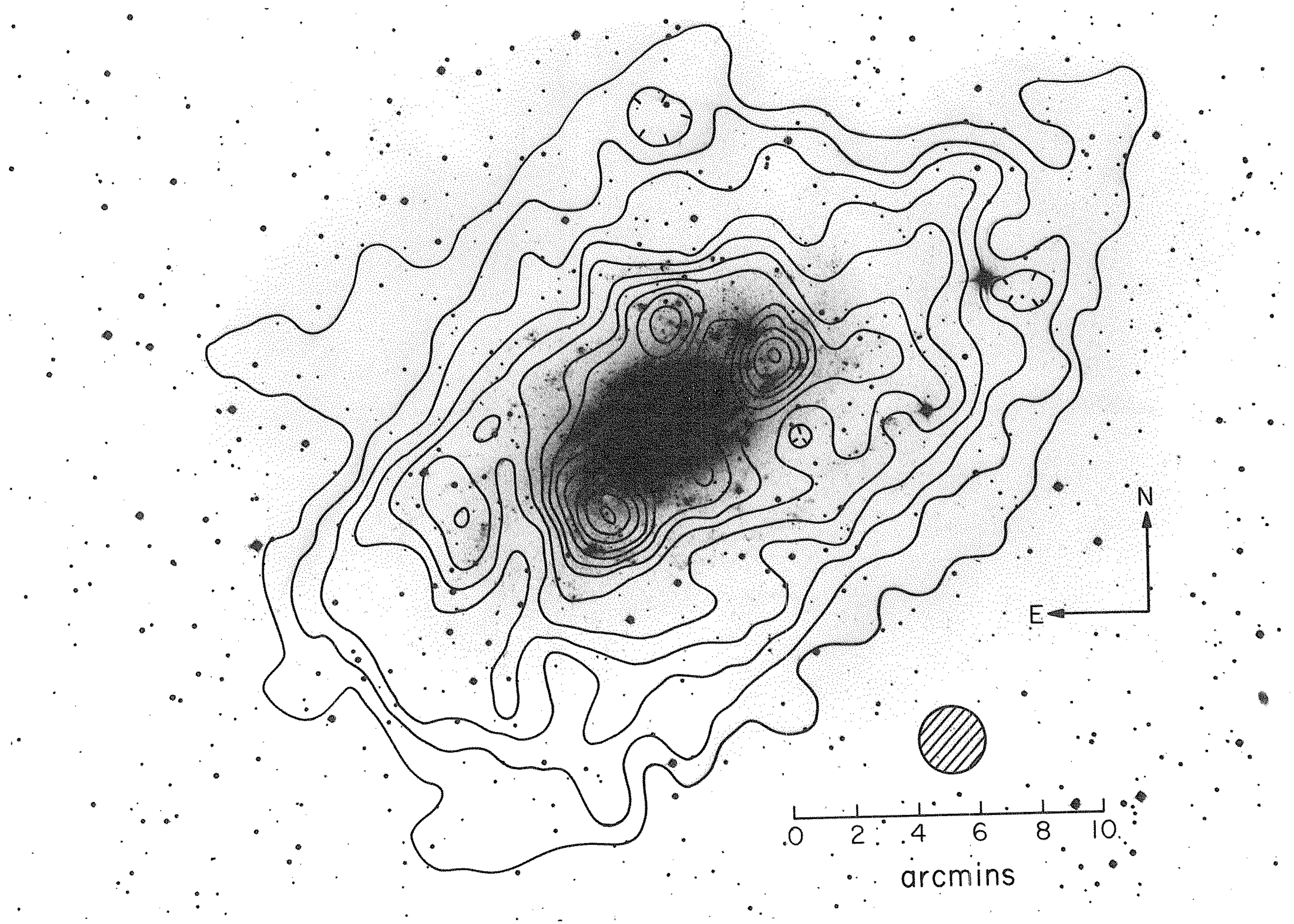

Figure 18. Integrated hydrogen map of NGC2403 superimposed on (blue) Palomar Sky Survey print.

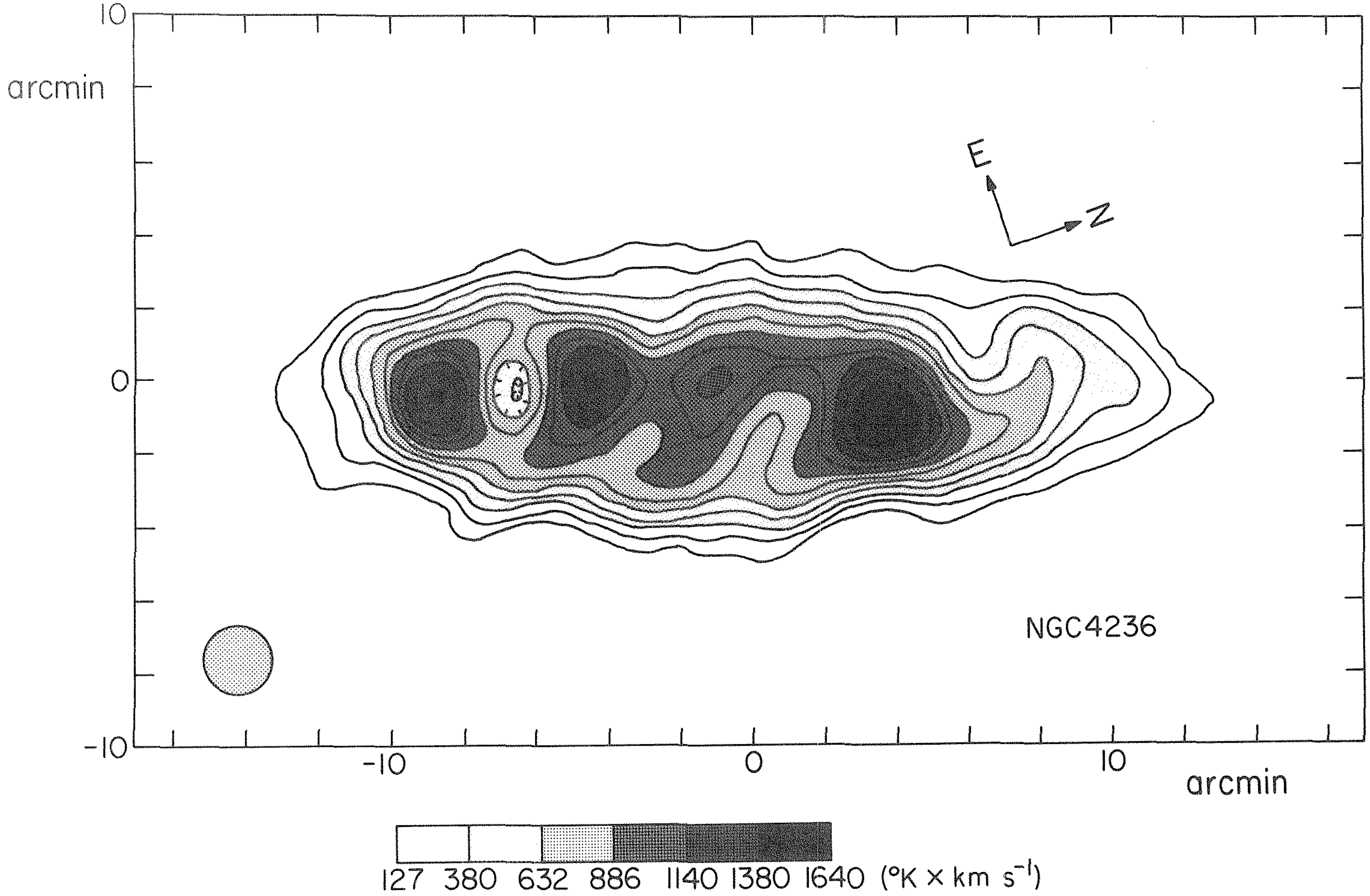

Figure 19. Integrated hydrogen map of NGC4236. Contour increment corresponds to line-of-sight density of 2.34×10^{20} at.-cm^{-2}.

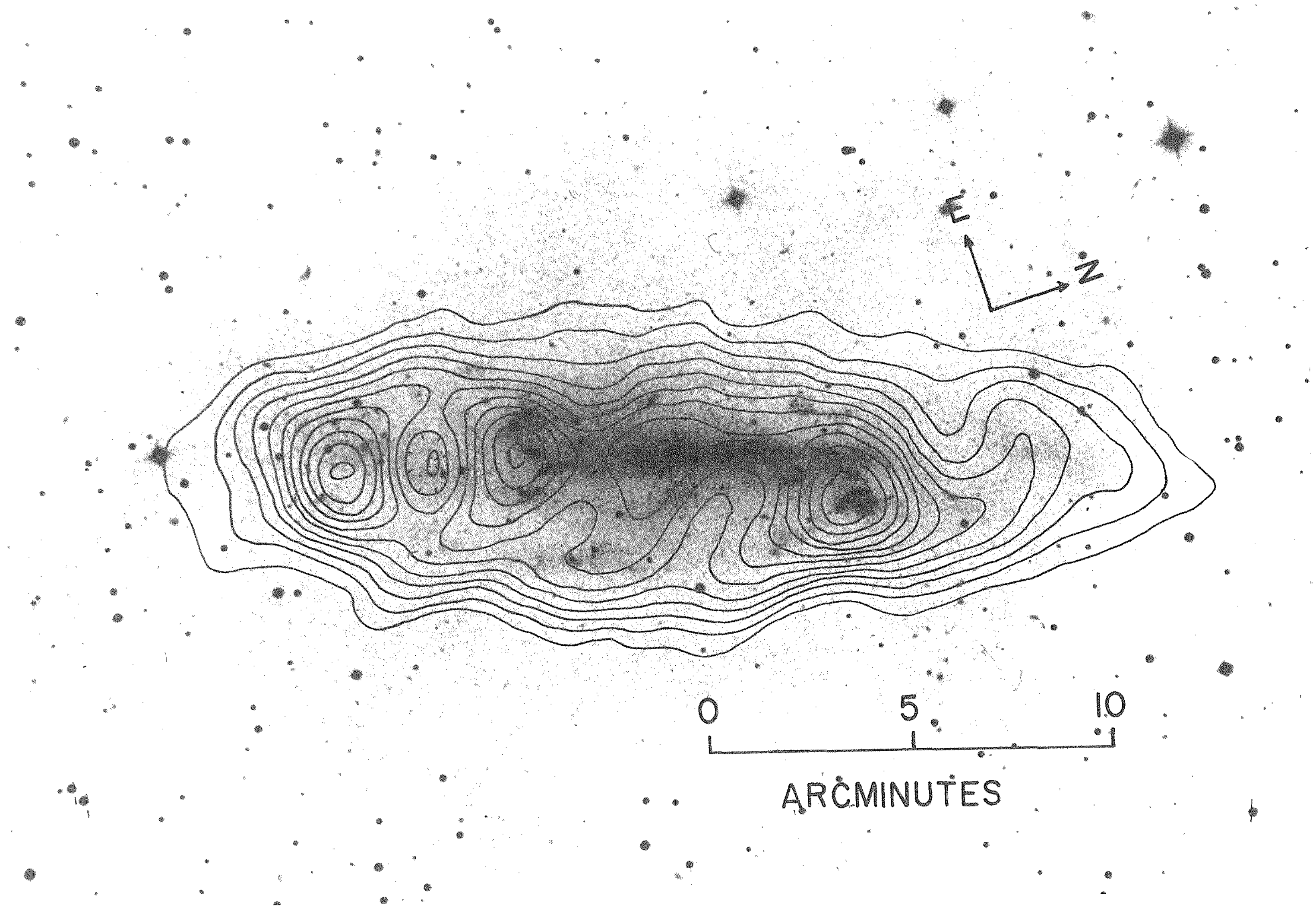

Figure 20. Integrated hydrogen map of NGC4236 superimposed on (blue) Palomar Sky Survey print.

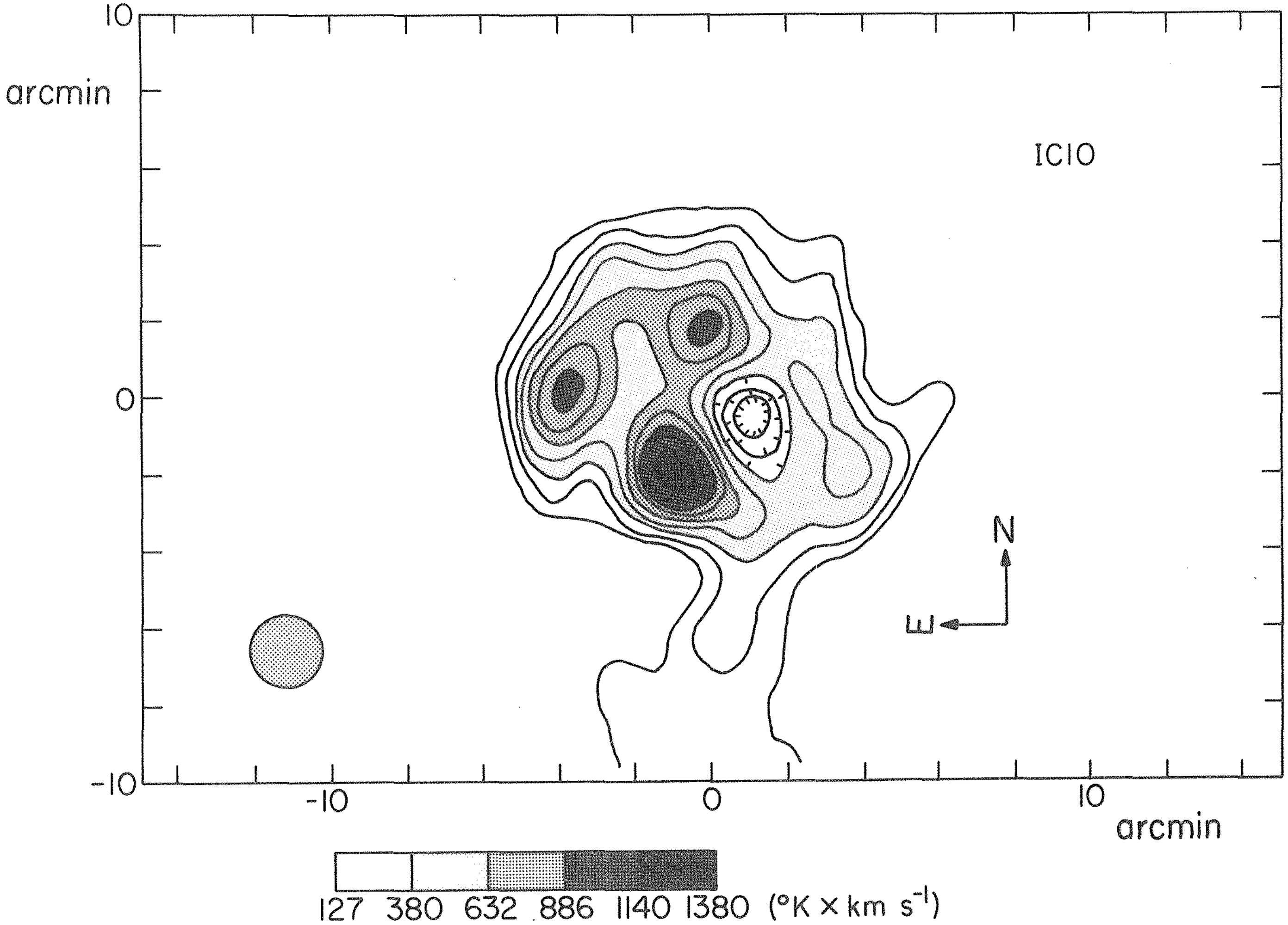

Figure 21. Integrated hydrogen map of IC10. Contour increment corresponds to line-of-sight density of 2.34 x 10^{20} at.-cm^{-2}.

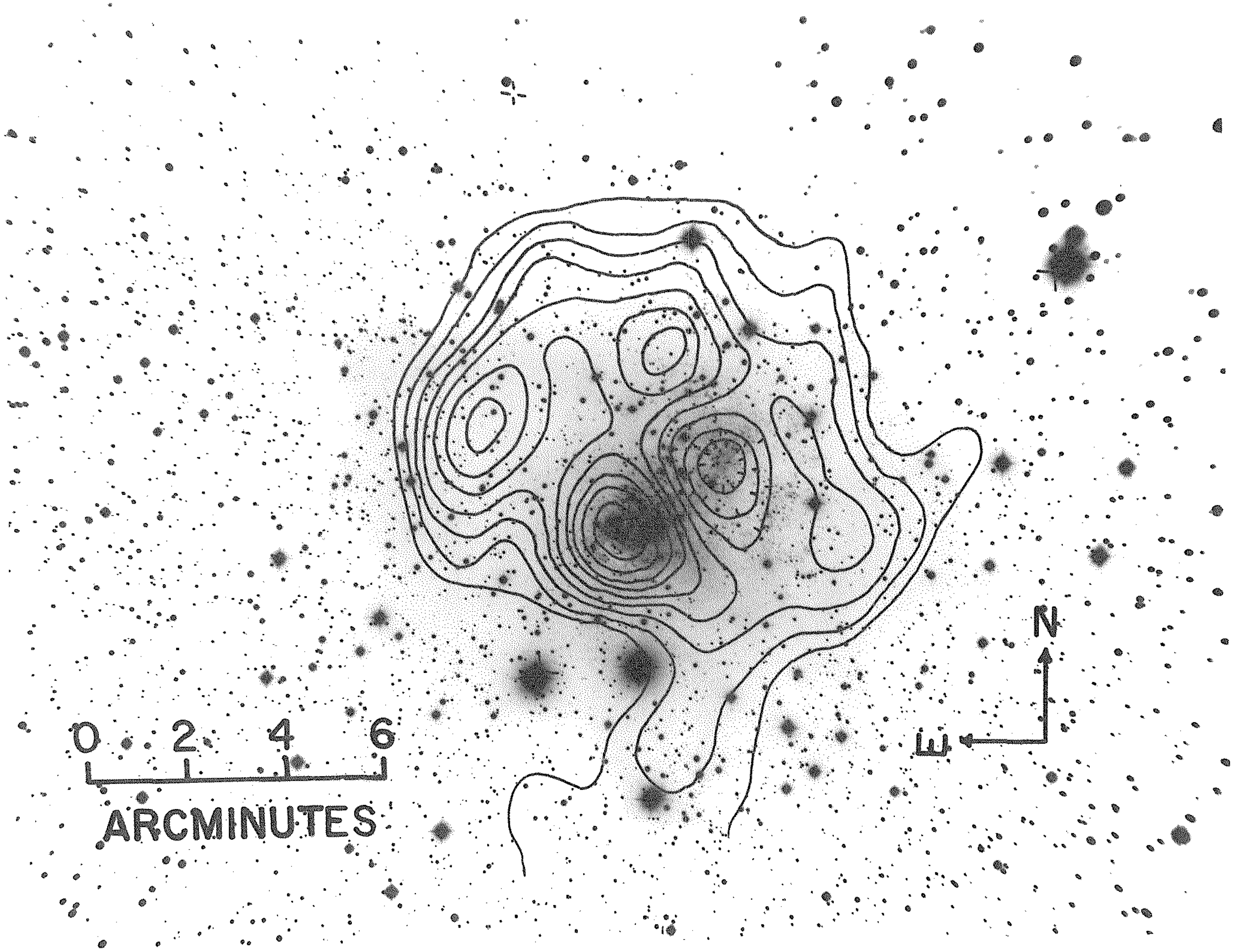

Figure 22. Integrated hydrogen map of IC10 superimposed on (blue) 200" photograph.

relative error of ~1 contour level in the summed maps. Absolute scaling error, due to calibration uncertainty of the zero-spacing profiles, was estimated in Chapter 2 to be $\leq$20%. The origins of these maps are at the zero-phase positions given in Table 7.

In Figures 18, 20 and 22 the total hydrogen maps are shown superimposed on photographs of the appropriate objects. For NGC2403 and NGC4236 these are blue plates from the Palomar Sky Survey; for IC10 red and blue sensitive plates were kindly supplied by F. Zwicky. The contours are superposed on the blue plate. Separate discussions of these maps for each object follow below.

4. NGC2403 - HI Distribution

The observed hydrogen shows overall coincidence with the optical object. Equi-density contours have an elliptical shape consistent with a flattened gas distribution at the galaxy's inclination and position angle. Angular extent of the hydrogen is essentially the same as the optical size (29' x 15') given by Holmberg (1958). Integration of the observed hydrogen in quadrants defined by the major axis and dynamical center (listed in Table 9) shows slight asymmetries. The fractional HI content is given by the diagram.

22%	22%
31%	25%

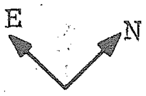

The somewhat greater hydrogen content of the southern quadrant reflects the location of the principal HI peak in this region.

The HI extension seen along the north-west semimajor axis also appears in the map of Burns and Roberts (1971); this latter map, the only other two-dimensional study of HI in NGC2403, is well reproduced by convolution of the present data with a 10' beam. Burns and Roberts have suggested that the extension is possibly due to distortion of the gas by a nearby hydrogen companion. Distortion of the neutral hydrogen is seen in several external systems. The bending of the HI in our own Galaxy (see for example Kerr and Westerhout 1965) is duplicated in M31 (Gottesman and Davies 1970). The influence of companion galaxies has been cited as a possible explanation for the warping. More serious asymmetries are seen in M101 (Beale and Davies 1969), and NGC300 (Shobbrook and Robinson 1967), in which the tidal effects of nearby galaxies are again suspect. A similar situation obtains for the two southern objects NGC253 and NGC5236 (Lewis 1969). Assuming that interaction with companions is responsible, distortion of the gas is to be expected in a large number of galaxies; Arp (1964) has stated that 20 of the 31 brightest spirals in the Shapley-Ames Catalogue had companions within four galactic diameters. Nonetheless, the present high resolution map hardly encourages the belief that NGC2403 must be categorized as a seriously disturbed system. The bulk of the north-west "wing" seems to be a logical extension of two optically visible spiral arms. It is true that the prominent south-western arm displays a larger pitch angle as it trails in the direction of the N.W. semi-major axis. This effect is evident when comparison is made with visible arms on the opposite side of the galaxy. Furthermore, the region in question has an excess radial velocity toward the observer (see Figure 28 or the rotation curve, Figure 31), suggesting an expansion of about 15 km-s^{-1} in the galactic plane. However, these anomalies are small in comparison with the truly disturbed systems described above. No perturbing object is visually apparent; van den Bergh (1959) lists a dwarf spheroidal companion of very low surface brightness, but it is one degree north of NGC2403.

The general HI distribution is characterised by a high plateau of emission near the center which gives way to a relatively slow decrease toward the edges. The contours of the plateau accurately delineate the central, high luminosity disk of the galaxy. Near the edges of the plateau, at approximately 4 kpc radius, are several HI emission peaks with columnar densities nearly twice that of the surrounding regions. These peaks suggest that the neutral hydrogen surface density σ_{HI} is maximal in a "ring" of the quoted radius. This appearance is, once again, common to several external galaxies, principally M31 (Roberts 1966a; Davies and Gottesman 1970) and M101 (Rogstad and Shostak 1971). Our own Galaxy also has a minimum in the value of σ_{HI} near the nucleus (see Oort 1965a), a deficiency which is correlated with a volume density minimum (Kerr 1962). One must exercise care in interpreting the columnar densities obtained for external galaxies as volume densities since this obviously depends on a knowledge of the thickness of the HI disk.

There has in the past been some disagreement over the existence of a central depression in the HI surface density of NGC2403. Roberts (1967) originally claimed a "ring" distribution of 9' radius based on a double-peaked hydrogen distribution at the systemic velocity. Guélin and Weliachew (1969) failed to detect this ring with the Nancay telescope, claiming instead a Gaussian (radial) HI distribution of 20' half-intensity width. The controversy illustrates the dangers of data interpretation; the present high resolution study is compatible with both sets of observations. The double-peaked systemic velocity distribution certainly exists for this object (see Figure 13), but in itself is a poor indicator of ring structure. The presence of a differential velocity field and a total HI surface density which eventually decreases with radius combine to produce the double-peaked appearance even for centrally concentrated hydrogen distributions. This point has been made in the literature (Wright 1971).

On the other hand, the 4' x 33' beam of the French instrument is rather unsuited for detecting ring distributions. Integration of the observed total HI map for NGC2403 along the north-south direction and subsequent convolution to 4' produces an east-west distribution identical in shape to that published by Guélin and Weliachew.

Burns and Roberts (1971) re-analyzed their 300-foot data using an improved model-fitting technique and conclude that the maximum in the HI surface density occurs at a radius of 5', but the contrast ratio with respect to the center is low. This description is similar to the average radial distribution found here and shown in Figure 23. Note that σ_{HI} has been corrected for inclination.

To the extent that the ring-like HI features are smaller in width than the beam size, some enhancement of the HI contours of Figure 17 is expected in the vicinity of the major axis. This is simply a geometric crowding effect resulting from the fact that near the major axis we are looking along, rather than perpendicular to, the feature.

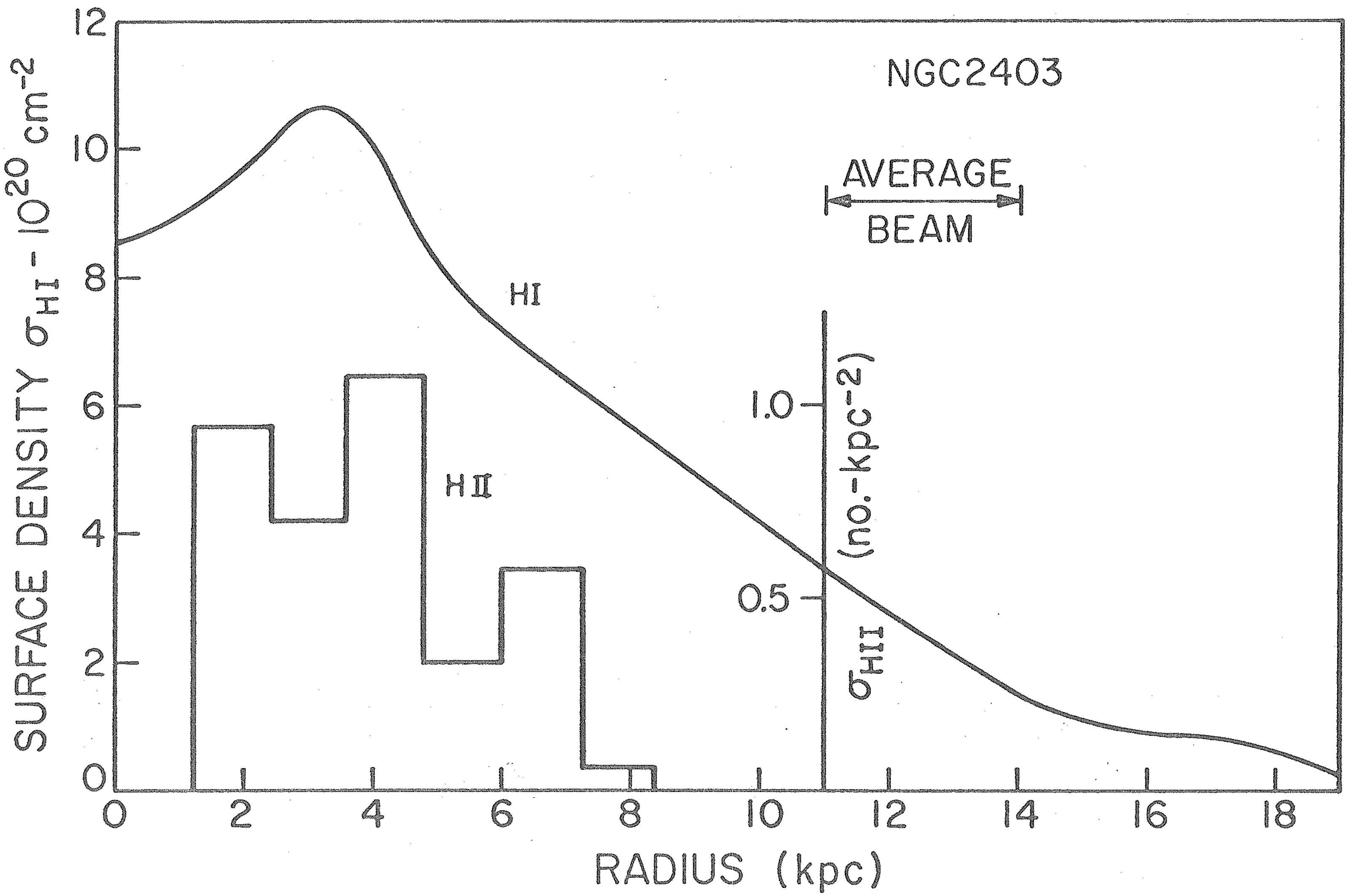

Figure 23. Average radial distributions of HI and HII regions for NGC2403. The HII information, which does not include the central 1', is from Hodge (1969).

We expect the apparent brightness of the ring-like emission to be increased by roughly the secant of the inclination near the major axis. The effect will largely account for the proximity to the major axis of the two largest concentrations in the total hydrogen map. The individual narrow-band peaks are similarly affected; the brightness temperatures of peaks near this axis are 40% higher than those situated elsewhere. The severity of this effect should be more than twice as great for M31 ($i=75^0$), an hypothesis amply verified by the maps of Davies and Gottesman.

Having established that the maxima of the neutral hydrogen surface density occur in a more or less circular region at 4 kpc radius, we inquire further into the dimensions and possible nature of this distribution. We might first consider the explanations proposed for similar morphology seen in other galaxies. These may be broadly described as follows:

1) Ionization of the neutral hydrogen in the central regions.
2) A thickening of the HI layer with radius, thereby producing a central minimum in σ_{HI}.
3) A true HI volume density increase in the ring.
4) Interaction with a central continuum source.

As discussed in Chapter 4, we may rule out mechanism 4) immediately because of the very low intensity of the continuum radiation from NGC2403. Ionization, item 1), has been advanced by Rogstad (1971) as the cause of the very deep central depression in M101. It is certainly of small consequence here since the interferometric investigations of Deharveng and Pellet (1970) reveal no extended ionized region in NGC2403. Their data place an upper bound on the emission measure[1] of 20 cm^{-6}-pc (Monnet 1971). This amount of ionization could account for a reduction in σ_{HI} of only 2×10^{20} cm^{-2}, assuming a uniform distribution of hydrogen in a column 200 pc thick. The uniform density assumption overestimates the HI depletion, a fact to be borne in mind when assessing the plausibility of this mechanism in other galaxies. However, even with this optimistic estimate, the depression in σ_{HI} as judged by Figure 23 is twice that ascribable to ionization.

Suggestion 2), a radial thickening of the HI layer, would be tenable only if the hydrogen volume density ρ_{HI}, which must ultimately decrease with radius, does so only slightly out to the region of the ring. Since the

---

[1] Emission measure (EM) is defined as $\int n_e^2\, ds$, where n_e is the electron (=ionized hydrogen) density and S is the path length through the medium.

neutral hydrogen is of negligible importance in determining the gravitational field of the galaxy, one would expect the thickness of the HI layer to be governed by the local total mass density and the z-motions of the gas. A simple analysis (Chapter 6) shows this dependence to be of the form $\Delta z \propto \frac{\Delta V}{\sqrt{\rho}}$, in which ΔV is the velocity dispersion of the HI in the z-direction, ρ the local total mass density and Δz the thickness of the HI disk. If we naively assume ΔV to be approximately constant, and use the mass density model for NGC2403 shown in Figure 34, then we expect a factor of two thickening between 1 and 4 kpc. This is capable of producing a very substantial central depletion in the observable σ_{HI}, assuming no great reduction in hydrogen volume density occurs over the same radius. It is additionally satisfying to note that this mechanism would favor objects with strongly peaked central mass densities, the very ones which show evidence of such depletions. As an explanation for rings, thickening of the gas layer has been suggested by Pikel'ner (1968).

Our own Galaxy, whose HI thickness doubles between the central region and the solar neighborhood (Kerr and Westerhout 1965), also shows a doubling of the volume density between the nucleus and 8 kpc (op. cit.). This effect, item 3) above, is observationally inseparable from the thickening mechanism.

We consider the example of M33, sister galaxy to NGC2403, and subject of both low and high resolution HI studies. When observed by Gordon (1971) with a 10' beam, a central depression of approximately 10% was seen in the total HI map for M33. Baldwin et al.'s (1971) subsequent investigation with a 1½' x 3' beam showed the hydrogen distribution to be very flat but with many small, intense emission regions. The central depression, as defined by the general level of σ_{HI}, had disappeared. The relative resolution for NGC2403 lies between that of Gordon and Baldwin et al. when account is made of the object's greater distance and size. In light of the break-up of M33 into small emission regions, we suggest that a similar lumpy distribution probably obtains for NGC2403. The ring may prove to be a relatively narrow clustering of high intensity knots.

As further evidence for this suggestion, we note that the prominent concentrations in the total HI map are composed of hydrogen covering a wide range of rotational velocity. They therefore do not indicate "superclouds", but rather unresolved regions in which high density concentrations occur. Summing such unresolved closely-spaced sources causes an apparent loss of information, as the resulting map shows only slightly beam-broadened contours. A return to the narrow-band maps allows determination of the position of the concentrations with an uncertainty much less than the synthesized beamwidth. (This is possible because for essentially unresolved sources the positional information is limited only by the amount of phase error in the data, but not by the finite beam size.) A plot of the major and minor narrow-band concentrations is shown superimposed on a photograph of NGC2403 in Figure 24. The distribution of the peaks is in remarkably good agreement with the location of the spiral arms. In particular, a regular series of strong maxima delineate the rather broad arms at approximately 4 minutes radius, giving rise to the ring-like appearance of the total HI map. The bifurcating arm 7' east of center and the prominent arm 5' S.W. of the major axis are similarly marked by secondary maxima. In the case of the latter feature this coincidence is particularly noteworthy as the arm region is undistinguished on the total HI map. A few peaks appear to be outside the optical extent of the object although their locations are generally along logical extensions of the visible spiral arms.

One might argue, in a manner similar to the previous discussion on the double-peaked appearance of the systemic velocity map, that the peaks in the narrow-band maps do not really mark regions of increased σ_{HI}, but simply result from the widening of the regions of constant radial velocity away from the nucleus. If this were true, however,

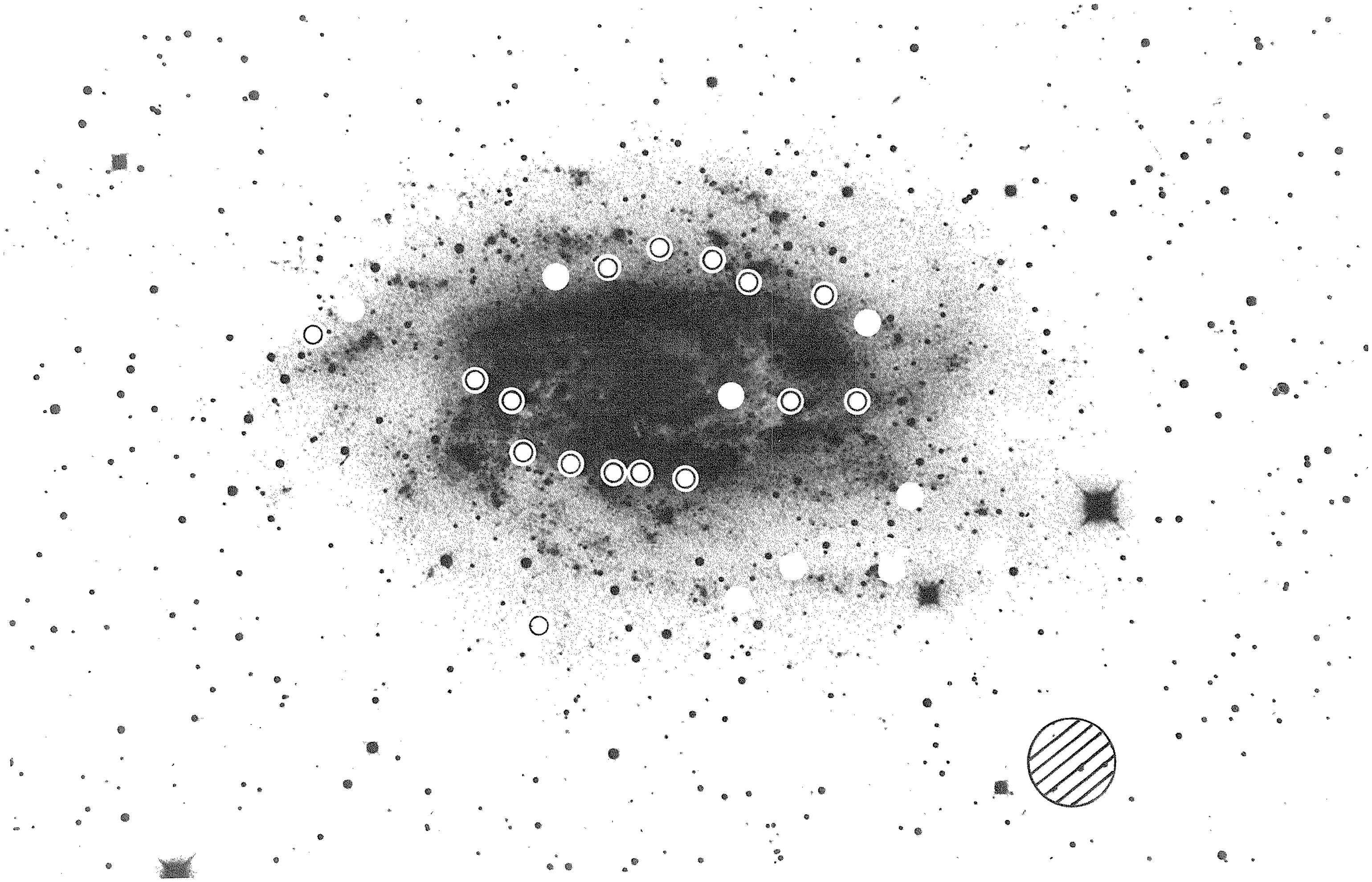

Figure 24. Positions of peaks on narrow-band maps for NGC2403. Dots with circles indicate principle peaks.

the sum of these maps would not produce the peaks at 4 kpc radius.

The maximum brightness temperatures of the unresolved peaks are about 25^0K except along the major axis where they rise to about 35^0K. The evidence is suggestive of a situation in which the hydrogen along the spiral arms is clumped into small regions of high density and/or optical depth, with a smoother, unsaturated distribution elsewhere. This is similar to the two-component model of gas distribution described earlier.

Figure 24 is quite like a similar plot made for M31 (see Figure 8, Davies and Gottesman 1970). Good agreement between the HI concentrations and the arm-defining HII regions was found for this object, a result in accord with the present investigation. In particular, the ring-like disposition of the principal concentrations is strikingly similar in the two galaxies. This is despite the fact that the central depression in M31, unlike NGC2403, is quite deep.

We have concluded, then, that the central HI distribution in the present object can be described as a plateau of ~4-5 kpc radius over which σ_{HI} varies by $\leq 10\%$ (when averaged over a beamwidth). At the edges of the plateau, and having a circular distribution coinciding with thick spiral arms, are unresolved regions of intense emission. Similar regions appear along outer spiral arms.

It is also probable that these regions are optically thick. As mentioned, brightness temperatures in the narrow-band maps are as high as 35°K. Rewriting equation (5.8) gives

$$\tau_L = -\ell n \left[1 - \frac{T_B}{T}\right] \quad , \qquad (5.21)$$

which yields an optical depth of 0.4 for a kinetic temperature of 100°K. This is obviously a very crude estimate, but assuming the peak regions are unresolved, we have erred on the low side for τ_L.

The general positional coincidence of the HI maxima and the spiral arms has been noted. One would logically expect a similar coincidence of HI and HII regions since the rate of star formation, a process indicated by the ionized regions, is surely dependent on hydrogen density. A two-dimensional comparison is displayed in Figure 25 in which the HII regions as mapped by Hodge (1969) are shown superposed on the HI contours of the present study. One notes the good positional agreement between the major HII regions and clusters of regions and the HI peaks. In particular, the very largest HII knots invariably fall in the ring-like area of enhanced σ_{HI}. Similar correlations of HI and HII have been found in M31 (Davies and Gottesman 1970), the Large and Small Magellanic Clouds (McGee and Milton 1966; Hindman 1967) and NGC4236 and IC10 (see below). HI peaks at the locations of HII regions have also been observed

Figure 25. HI contours for NGC2403 superimposed on Hodge's (1969) map of HII regions.

in the Galaxy (see for example Hughes and Routledge 1970; Bridle and Kesteven 1970).

Of perhaps slightly more interest is the radial distribution of HII emission. In Figure 23 are plotted both the average value of σ_{HI} and the frequency (number/kpc^2) of HII regions from the data of Hodge (corrected to a distance of 3.2 Mpc). Because of the high photographic densities near the center of NGC2403, the HII frequency is not given within 1 kpc of the nucleus. One notes again the good correspondence of HI and HII densities. The secondary HII peak at ~7 kpc is caused by two prominent spiral arms. Enhanced neutral hydrogen in the arm regions is not apparent on this graph because it is washed out by the averaging procedure. One should compare Figure 23 with the plot of basically similar quantities for the Galaxy given by Oort (1965a). The differences are remarkable. Frequency of HII regions in the Galaxy is sharply peaked at ~5 kpc, and this peak lies inside the areas of high σ_{HI}. The latter quantity is distributed in a rather uneven plateau from 5 to 15 kpc, dropping steeply at both boundaries. The data for NGC2403 would suggest that major HII region formation occurs only when σ_{HI} is greater than 5×10^{20} cm^{-2}. Oort's plot places the peak HII frequency in a region with half that surface density. One might note, however, that a relatively small adjustment of the Galactic distances would ameliorate this discrepancy somewhat.

It is more logical, of course, to compare the radial gas distribution of NGC2403 with that of other Sc objects, the Galaxy being assumed to be of earlier type (see de Vaucouleurs 1970). Baldwin *et al.*'s (1971) high resolution study of M33 produced an HI surface density which was essentially flat out to 5 kpc and of a value practically identical to that found for the inner regions of NGC2403. Beyond this radius the distributions are dissimilar; in M33 σ_{HI} drops to 10% of its peak value in 3 kpc, while the fall-off for NGC2403 is only one-third as fast. (Note that the discrepancy is not attributable to beam effects.) The difference is possibly related to the greater mass of NGC2403. If one disregards the asymmetry in M101, its radial surface density has a low central value and then rises to the plateau value of the previous two objects at ~6 arcmin (Rogstad and Shostak 1971). From there it drops essentially to zero in two beamwidths. The radial dependence of σ_{HI} for this object seems intermediate between that observed for NGC2403 and M31. As mentioned, the latter galaxy has a very definite hole in the center. If, as Rogstad (1971) has suggested, ionization is responsible for the HI deficiency in the inner regions of M101, then it may yet be similar to the other Sc objects. Otherwise, one must seriously reconsider any hypotheses proclaiming a simple correlation of HI distribution with galactic type. This matter is discussed further in Chapter 7.

The continuum source in NGC2403, shown in Figure 10, is generally extended along the major axis suggesting a confinement to the disk. Unlike the continuum radiation in M31 (Pooley 1969), no correlation is apparent with either the HI or HII distributions; however comparison is unfair because of the lesser sensitivity of the present study. For the same reason, any nuclear point source analogous to Sagittarius A in our own Galaxy would not be discernable. The central regions of the source in NGC2403 (defined by $T_{BC}>1.5^{0}K$) could conceivably be decomposed into three point sources, each with a flux of ~0.03 f.u. This is twice the flux of the supernova remnant Cas A at the same distance. However, no supernovae have been detected in NGC2403 (Zwicky 1964). A non-thermal source of similar amplitude and extent is seen in M101.

5. NGC4236 - HI Distribution

The neutral hydrogen distribution for NGC4236, shown in Figures 19 and 20, is in excellent agreement with the visual appearance of this object. Every major optical feature has a corresponding HI feature and, when allowance is made for beam broadening, no 21-cm emission is found outside the optical bounds of the galaxy, given as 26' x 9' by Holmberg (1958). Unfortunately, due to its high inclination and low luminosity, the morphology of NGC4236 is not entirely clear. Examination of a 200" blue plate taken by Sandage (private communication) shows a very regular and sharply defined outer elliptical boundary. Symmetrically placed within this ellipse, and about half its maximum dimension, is the smooth bar. At each end of the bar appear patches of bright nebulae from which spiral arms break away. The situation is complicated by what appears to be an additional arm, concentric with the others, but originating near the northern end of the bar on its western side. The southernmost optical emission for this galaxy, coincident with an HI surface density peak, seems to be an extension of this arm rather than the one of greater radius which begins at the northern end of the bar. Evidence for a fourth arm on the eastern side of the bar is uncertain, for this region is only faintly visible.

The hydrogen distribution is once more marked by several peak concentrations having a contrast of as much as two to one with the general 21-cm emission. Two of the peaks are symmetrically placed at the ends of the bar and coincide with prominent HII regions. The third, mentioned above, is located at the southern extreme of the galaxy. Two of these three peaks have almost identical amplitudes and extent; the northermost peak represents considerably more HI. A fourth, substantially weaker concentration is found on the bar axis, 2' south of the galactic center.

Examination of an Hα plate taken by Sandage shows this position to coincide with the strongest HII region within the bar.

Along most of the bar, we find an HI surface density of 4.5 x 10^{20} cm^{-2} when correction is made for inclination. With an arbitrarily assumed thickness of 0.2 kpc, the average hydrogen density in the bar is 0.7 cm^{-3}, considerably less than found in the central disk regions of our own Galaxy (Oort 1964) or NGC2403. It is clear that NGC4236's low optical luminosity has its counterpart in a low HI surface density; it is easily observed only because of its high inclination.

Several HI extensions below the western side of the bar can be seen. There are clearly associated with regions of greater stellar density in the spiral arms. At the southern end of the galaxy, the hydrogen contours extend in such a way as to make a closed loop about a depleted region situated between the end of the bar and an arm. The extreme southern peak, mentioned before, occurs in an area of relatively weak Hα emission. Because of the 'turning back' of the spiral arm found here, geometric crowding has enhanced the apparent columnar densities.

We return to consideration of the HI peaks occurring at the ends of the bar. Inspection of the narrow-band maps shows that these features have an approximate (radial) velocity width of 40 km-s^{-1} (see Figure 14). The velocity field data of the next chapter show a gradient of approximately 15 km-s^{-1}-arcmin^{-1} in the region of the peaks, which consequently represent truly extended regions and not simply small, intense emission knots which have been beam broadened. The existence of knots within the peaks is certainly not precluded by this line of argument; we simply wish to emphasize the extended nature of these regions. The maximum brightness temperature of the peaks is 40°K.

The existence of these higher density regions provides a certain similarity of appearance between NGC4236 and the spirals. Both have their maximum HI surface densities occuring several kiloparsecs from their nuclei. However, the peaks in NGC4236 are most simply explained by assuming that the HI distribution is concordant with the luminosity distribution. Consequently the peaks are composed of emission from the ends of the bar and from the beginnings of the spiral arms. Because of the galaxy's inclination, the beam is incapable of separating the arms from the bar. Note that this explanation requires the regions of greatest hydrogen content in the arms be near their point of contact with the bar. This seems plausible given the similar disposition of the major HII regions.

Integration of the contours of Figure 19 gives an HI mass for the bar alone of 2.5 x $10^8 M_\odot$.

Despite the presence of the peaks, the general hydrogen distribution has no major asymmetries. Contour integration shows the fractional HI content in each quadrant to be as follows:

25%	20%
30%	25%

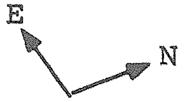

The differences are not considered significant.

A plot of the average surface density as a function of radius would not be meaningful for this object because of 1) the fact that azimuthal symmetry is not anticipated for a barred galaxy, and 2) the great disparity in relative resolution along the major and minor axes. Instead, Figure 26 shows separately the average radial dependence of σ_{HI} along these two axes. On a radius perpendicular to the bar, where the galaxy is only 3.5 beamwidths wide, we see a smooth fall-off of σ_{HI} with distance from the nucleus. However, along the major axis, with four times the relative resolution, there is a well-defined plateau of higher density delineating the bar followed by a secondary peak where this axis intersects the spiral arms. Note that, compared to NGC2403, NGC4236 has surface densities which are less by a factor of two. Also note the sharper "edge" to the hydrogen distribution in the barred object.

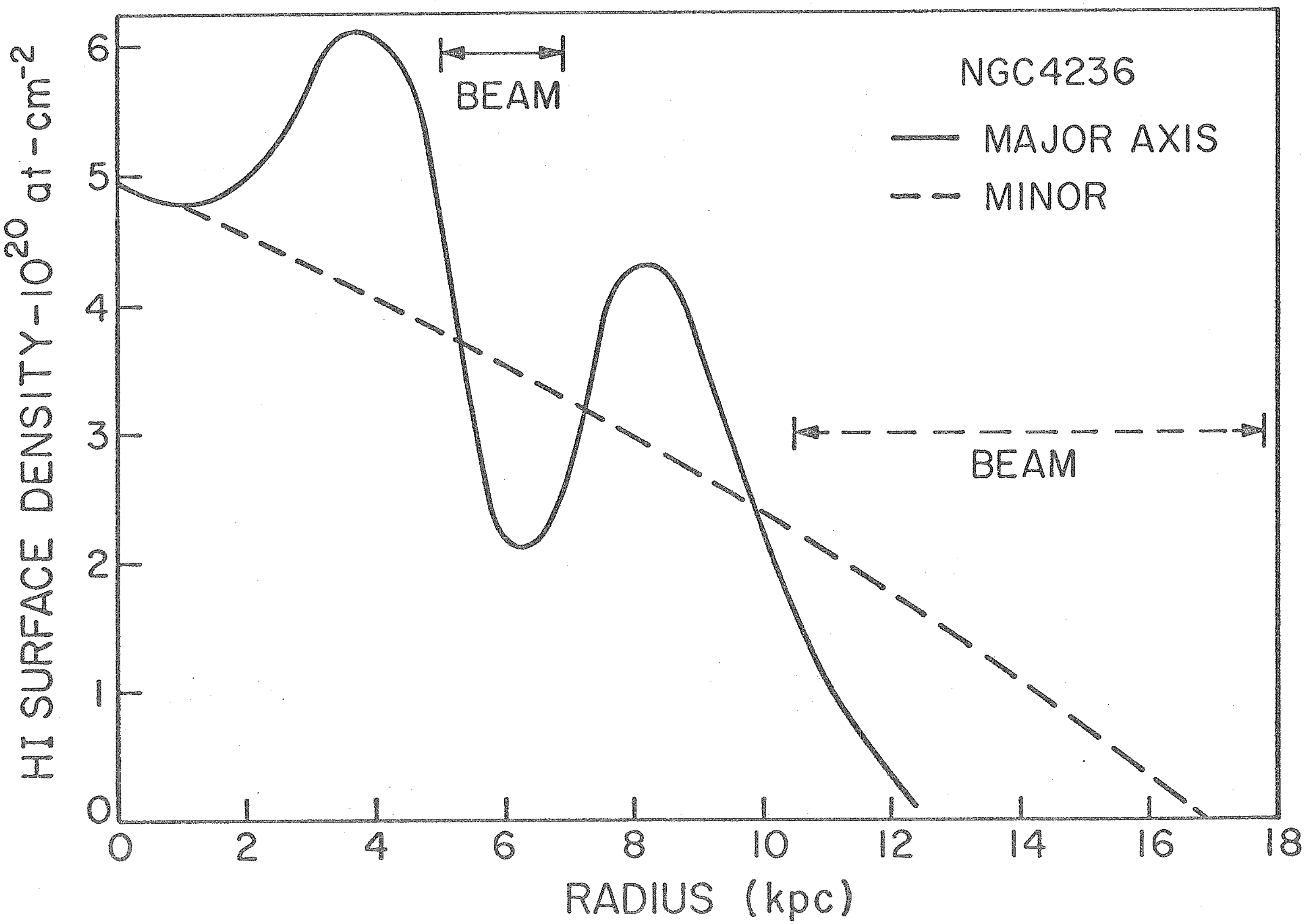

Figure 26. Average radial distributions of HI along major and minor axes of NGC4236. The surface densities are corrected for inclination.

The existence of the very well defined outer HI contours, in conjunction with the nearly edge-on aspect, allows us to place an upper limit on the density of a neutral hydrogen halo surrounding NGC4236. Knowledge of HI densities in the halo surrounding the Galaxy is made difficult by the presence of confusing local hydrogen, although values of $\sim 10^{-3}$ cm^{-3} have been estimated (Oort 1968). From the narrow-band maps for NGC4236 we may place an upper limit on the HI columnar density outside the galactic disk of 8×10^{19} cm^{-2}, assuming the gas is optically thin and seen in emission. If we assume for simplicity a uniform sphere of 10 kpc radius, the derived volume density is $\lesssim 10^{-3}$ cm^{-3}. The total HI mass of such a sphere would be $\lesssim 10^{8} M_{\odot}$, or about 7% of the measured hydrogen mass of the disk. A similar measurement by Roberts (1966c) on two nearby spirals (NGC4244 and NGC7640) produced a comparable upper limit on the HI volume density. However, because of his larger beam the measurements referred to regions 6 kpc above the galactic planes. The present data refer to an average height of 3.5 kpc. Furthermore, to the extent that the halo gas is pressure supported, we would expect the densities in NGC4236, because of its lower total mass surface density, to be higher than those in our own Galaxy or those measured by Roberts. Note that implicit in the measurement is the assumption that any halo hydrogen would have radial velocities in the measured range, about 450 km-s^{-1} centered near zero.

The weak continuum source in NGC4236 (Figure 11) is unresolved and located approximately 1' N.W. of the dynamic center (Table 9). This is a rather unremarkable region both optically and with regard to HI features. Photographs reveal a smooth stellar background with very little visible Hα emission.

6. IC10 - HI Distribution

The total HI map of IC10 presents a generally elliptical appearance with a faint extension to the south. Most of this extension arises from the lowest contour on a single narrow-band map. The shape of the contour is suggestive of a grating response, and therefore the reality of the extension is questionable. The main body of the object has approximate dimensions 10' x 8', substantially larger than the optical size (4!0 x 2!8) given by de Vaucouleurs (1964), however not so much larger that any support can be given the suggestion by Mayall (1935) that we are viewing only an arm of an otherwise obscured spiral.

There are three prominent peaks of HI emission forming an equilateral triangle with sides of ~3 kpc. The most intense of these coincides with the large HII complex comprising the principal optical feature of IC10. Both the other peaks occur in a region where no optical emission is evident, and we conclude that obscuration by the Galaxy is present in these directions. As noted in the Introduction, such effects have been anticipated for this object due to its low galactic latitude.

A slight beam broadening of the brightest HI peak is evident. The HI mass of this region is $3 \times 10^7 M_\odot$, and if we assume a spherical configuration the density has a lower bound of $0.7\ \mathrm{cm}^{-3}$. As discussed in connection with similar features in NGC2403 and NGC4236, this peak arises from emission over an extended area, a fact deduced from the slight changes in position of the peak from channel to channel. The changes are ~1', so the emission is probably contained within the HII region. Reference to the continuum map for IC10 (Figure 12) shows a very intense source (~8^0K peak) coincident with this peak. It is intriguing to think that this source is thermal emission from the ionized regions; however this seems unlikely from energetic considerations. The total 21-cm continuum flux of the source amounts to 0.2 f.u. Using the data of Pike and Drake (1964) we find that this is thirty-six times the expected flux of Cygnus X at the distance of IC10. Cygnus X is one of the largest HII complexes in the Galaxy, consisting of at least twenty identifiable sources of thermal emission. It seems more likely that a majority of the IC10 continuum is non-thermal. As further evidence, one may cite the example of

NGC4236 in which HII regions of similar optical appearance evidenced no continuum emission greater than 0.5^0K.

Comparison of IC10 with the Small Magellanic Cloud, a prototypical Irr I object, shows the latter to have a similar HI appearance with three intense peaks superposed on a smoother distribution (Hindman 1967). Typical dimensions of the peaks in the SMC are 500-600 pc. For IC10 the minimum size of the largest HI emission feature is 900 pc judged from the shift in the emission centroid from channel to channel. Higher spatial resolution may show this apparently single peak to consist of several smaller concentrations, with a consequent reduction in the velocity dispersion of each region.

Another similarity between IC10 and the SMC is the asymmetric location of the principal HI peak with regard to the general hydrogen distribution. Evidently the optical emission coincident with the peaks, representing the most luminous regions of these objects, is similarly offset from the galactic centers as determined by the overall hydrogen distributions. Roberts' (1970) lower resolution data for the irregulars IC1613 and Ho II suggest a similar situation; in both objects the principal optical emission fails to coincide with the HI centroid. If higher resolution studies of these galaxies should show the good agreement between HII regions and HI peaks found for IC10 and the SMC, then the evidence would be great that the irregulars are similar to the spirals in having their major HI and HII concentrations away from the centers of the gas distribution. This gives faint support to theories which describe the irregulars as having central maxima in their hydrogen surface densities (e.g. Roberts 1970). Perusal of the *Hubble Atlas of Galaxies* (Sandage 1961) shows many objects of type Irr I having HII concentrations near the edges of their optical images.

Because of the preeminence of this peak in both the optical and radio domains, it is interesting to question whether it might be analagous to the 30 Doradus nebula in the Large Magellanic Cloud. This latter object, the largest known HII region, is the strongest source of HI and radio continuum radiation in the LMC (McGee and Milton 1966; Mathewson and Healey 1964). In these regards it is entirely comparable with the central regions of our own Galaxy, a comparison which has forced the conclusion that 30 Doradus is the nucleus of the LMC despite its asymmetric position with regard to the overall HI and light distribution (Johnson 1959; Mathewson and Healey *op. cit.*). Qualitatively the situation is similar in IC10. Quantitatively, however, we have the same continuum energetics problem as before; the observed flux from IC10 is ten times the thermal emission from 30 Doradus at the same distance.

Furthermore, Tammann (private communication) reports that the HII regions in IC10 have rather normal dimensions, assuming that the luminosity classification (SIV) given by van den Bergh (1960) is correct. Although not comparable to 30 Doradus as an HII region, we must conclude that the primary peak bears at least a functional similarity to the nebula of the LMC: It is the locus of the maximum HI and (presumably non-thermal) radio continuum radiation as well as the dominant optical feature. To call it the nucleus of this galaxy, in spite of its asymmetric placement, is at least not without precedent.

Perhaps the most curious feature of the IC10 hydrogen distribution is the "hole" $2'\!.5$ north-west of the principal concentration. The HI columnar density in this region is less than 2×10^{20} cm^{-2}, the extent of the depression being essentially that of the synthesized beam. The hole is remarkable both for its depth and for the fact that it occurs in an area of optical emission. Since it seems unlikely that such anomalously low volume densities could be very extended along the line of sight, we infer that the neutral hydrogen in IC10 constitutes a flattened system. With an assumption of an overall circular HI distribution, an estimate of the galaxy's inclination can be made by examining the elliptical outer contours. An inclination of 30^0 with major axis position angle of $\sim 35^0$ is deduced, so that we see IC10 very nearly face-on. This conclusion is consistent with the relatively narrow line width of this object. The systematic displacement with velocity of the narrow-band maps, coupled with the knowledge that the system is flattened, indicate that this object has a general rotation. The velocity field, and the implied total mass, are discussed in Chapter 6.

The nature of the hole itself is somewhat mysterious. Examination of Zwicky's blue and red plates shows a patchy stellar background and several HII regions in the vicinity of the hole. Again one must consider the possibility that the apparent deficiency of hydrogen is the result of ionization. Reference to the continuum map for IC10 reveals a faint extension of the strong source coincident with the principal HI peak in the direction of, and extending throughout, the hole region. The brightness of the source in this region is about 2°K. We use the expression for optical depth in an ionized medium given by Greenstein and Minkowski (1953)

$$\tau_C = \frac{0.4}{\nu^2}\,\mathrm{EM}, \qquad (5.22)$$

where ν is in MHz and the emission measure (EM) has units pc-cm^{-6}. Since the optical depth will be small, the expected brightness of the 21-cm continuum source is

$$T_{BC} = 1.9 \times 10^{-3} \text{ EM}, \qquad (5.23)$$

with the assumption of an electron temperature of 10000°K in both formulae. Taking the line of sight thickness of the hole to be 1 kpc, the average hydrogen density required to fill the hole is 0.2 cm^{-3} which, if uniformly distributed, would provide an EM of 40. Since the ionized regions are expected to be filamentary, this value is a lower bound. Because for a fixed columnar density the emission measure is approximately proportional to the hydrogen density, clumping into regions with $n_H = 5$ cm^{-3} would produce the observed continuum brightness. This is still an underestimate of the required density if the continuum source is smaller than the beam. The importance of ionization could be easily ascertained by a moderately sensitive Hα investigation.

A rather more dramatic explanation would invoke an explosive event to clear the hydrogen from this region. Zwicky has noted the presence of semi-circular Hα features in IC10 which he suggests are supernova remnants (see Roberts 1962b). At least one such feature can be seen in the depleted area. Unfortunately, approximately 20 remnants with the radio brightness of Casseopia A would be required to produce the observed 2^0K continuum at the distance of IC10. There is a bending of the lines of constant radial velocity just outside the hole region (see Figure 30) suggesting large-scale non-circular motions, but higher velocity resolution studies are required to confirm such an hypothesis.

In conclusion, one must admit that the circumstances producing an apparent loss of $\sim 10^7$ solar masses of hydrogen in IC10 are uncertain. A fundamental datum in their determination is the existence of a relatively strong continuum source coincident with the depleted region.

VI. VELOCITY FIELDS AND MASSES

1. Determination of Velocities

Although radial velocities are only one component of a general three-component velocity field, the assumed symmetries of galaxies allow us to infer much of their dynamics from the radial measures alone. Unfortunately, representation of the radial velocity field is complicated by the fact that information on the hydrogen distribution and its velocities is unavoidably mixed in the course of observation. Most studies of external galaxies have been made with single-dish drift scans which generate line profiles for several points on the object. The assignment of a velocity to each of these points has been done by variously taking the mean, median or peak of the associated profile. Because of the generally large beamwidths involved, all of these measures are influenced by the hydrogen distribution.

In synthesis work, where brightness distributions are obtained for many discrete velocities, each such distribution will itself consist of a mix of information about the HI distribution and the velocity field. Considering an individual narrow-band channel, measurement of the visibility at a point in the (u,v) plane occurs after integrating the three-parameter visibility function over the appropriate filter response

$$\hat{V}_n(u,v) = \int_{-\infty}^{\infty} \hat{V}(u,v,V)\, f_n(V)\, dV, \qquad (6.1)$$

where $f_n(V)$ is the (normalized) power response of the n'th filter in velocity units. Inserting this into the Fourier transform relation gives, upon interchanging integrals,

$$B_n'(x,y) = \beta(x,y) * \int_{-\infty}^{\infty} B(x,y,V)\, f_n(V)\, dV, \qquad (6.2)$$

where $\beta(x,y)$ is the synthesized beam and $B(x,y,V)$ is the transform of $\hat{V}(u,v,V)$.

A great simplification, useful for evaluating the effect of finite filters and beams on the derived velocities, is to assume the velocity field to be single-valued. That is, at each point (x,y) there exists an associated unique radial velocity $V(x,y)$, so that

$$B(x,y,V) = B(x,y)\,\delta\{V-V(x,y)\}. \qquad (6.3)$$

$B(x,y)$ is the brightness integrated over all velocities. An observed narrow-band map becomes

$$B_n'(x,y) = \beta(x,y) * \{B(x,y)V(x,y)f_n(V)\}. \qquad (6.4)$$

Observed line profiles may be generated for each point (x,y) by plotting the $B_n'(x,y)$ as a function of the nominal channel velocities. By using the above equation, model profiles for assumed brightness distributions and velocity fields can be easily computed for comparison. Alternatively, by similar model analysis, one may judge the degree to which radial velocities derived from profile peaks, medians, etc. agree with their true values. This allows choosing a "best" method for extracting the velocity field from the observations.

In Figure 27 is shown one result of such a model analysis. The HI brightness used was the observed major axis distribution for NGC2403 and is shown in the figure. The beam and filter widths were equal to those of the present study. All three estimation schemes, profile peak, mean, and narrow-band channel ridge lines, fail to reproduce the true rotation curve. The general nature of the failure in all cases may be summarized as follows:

--- The slope of the linear part of the rotation curve is lessened and the two-dimensional loci of constant radial velocity are straightened.

--- The turnover of the rotation curve is flattened.

--- Although formally dependent on the total HI distribution, the observed velocity field is not overly sensitive to brightness irregularities.

Near the central regions of the objects where the velocity gradient is steep these resolution effects are

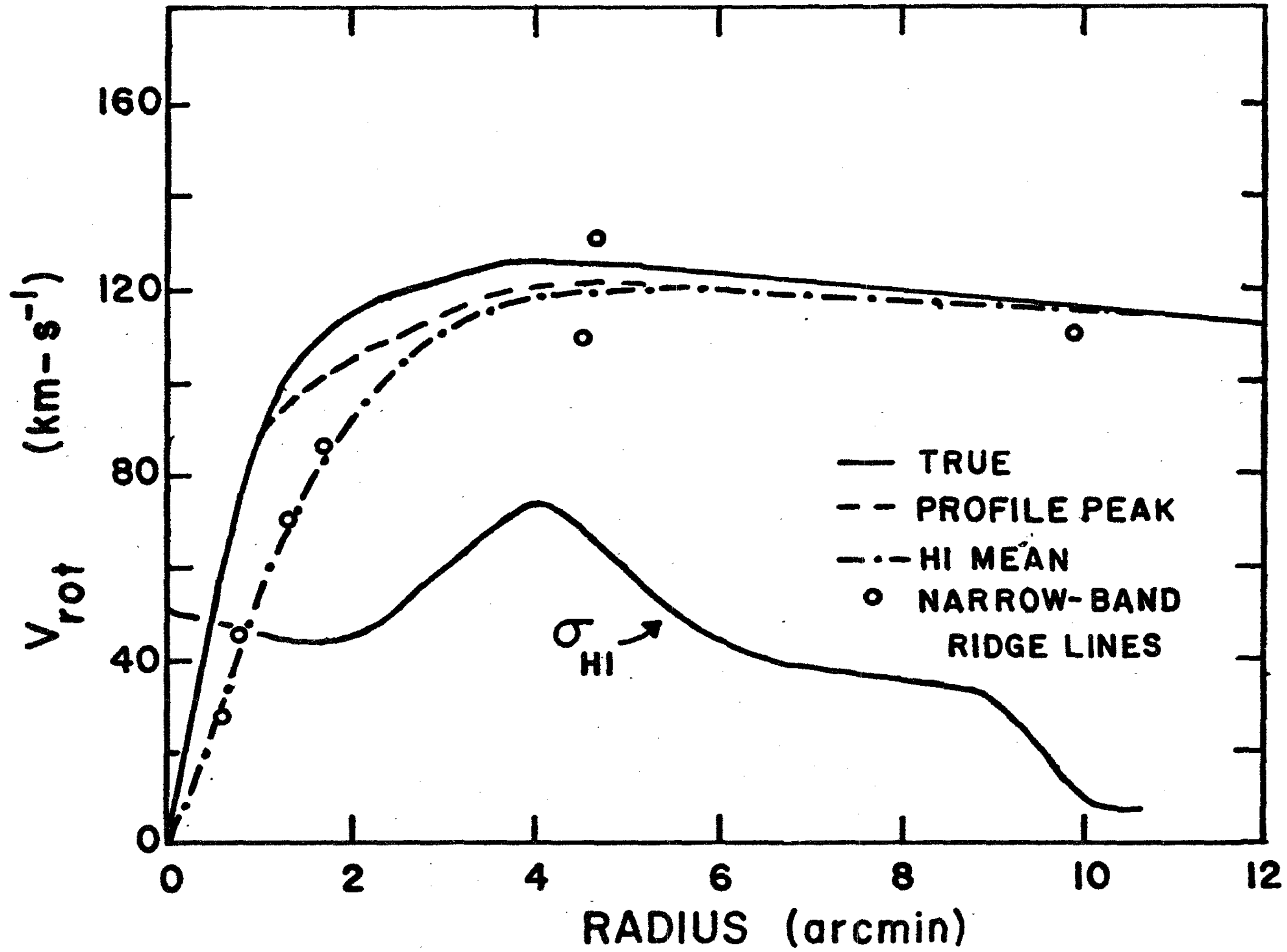

Figure 27. Sample model analysis for determining best method of defining velocities. The method adopted for the present study is to use the profile peak.

essentially the result of beam smearing. Once the velocity field has flattened out, the width of the filters is important, as well as the fact that one has response in only a few filters to define the field. Note again that the analysis has proceeded on the assumption of a flat system.

2. The Velocity Fields

On the basis of the model analysis, it was decided to use the peaks of the line profiles to define the velocity fields. The profile peaks are defined by fitting a Gaussian curve through the three highest points of the profiles. As with the production of the total HI maps, the channels were weighted to produce the smoothest spectral response. Brightness temperatures below the noise level were not included in the computations. The derived lines of constant radial velocity are shown in Figures 28, 29 and 30.

For purposes of comparison, mean profile velocities were also computed. The latter derivation simply involved taking the arithmetic mean velocity at each point on the object. These fields are not shown; they were in almost all respects similar to the profile peak curves.

With the assumptions of overall bilateral symmetry and small non-circular motions, these radial velocity fields afford a means of determining the position and systemic velocity of the galaxies' dynamical centers as well as

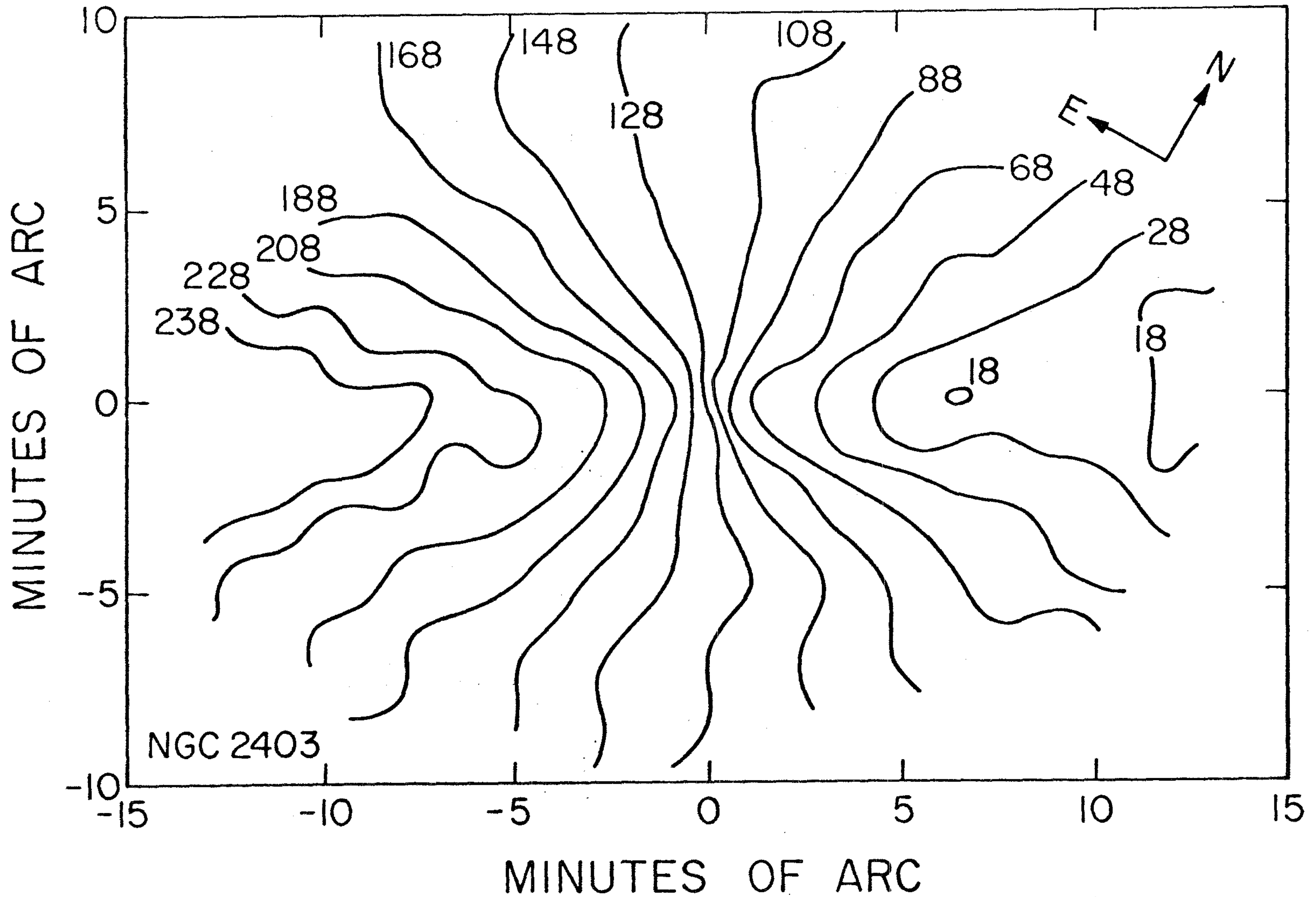

Figure 28. Radial velocity field of NGC2403. Velocities are in km-s^{-1} with respect to sun.

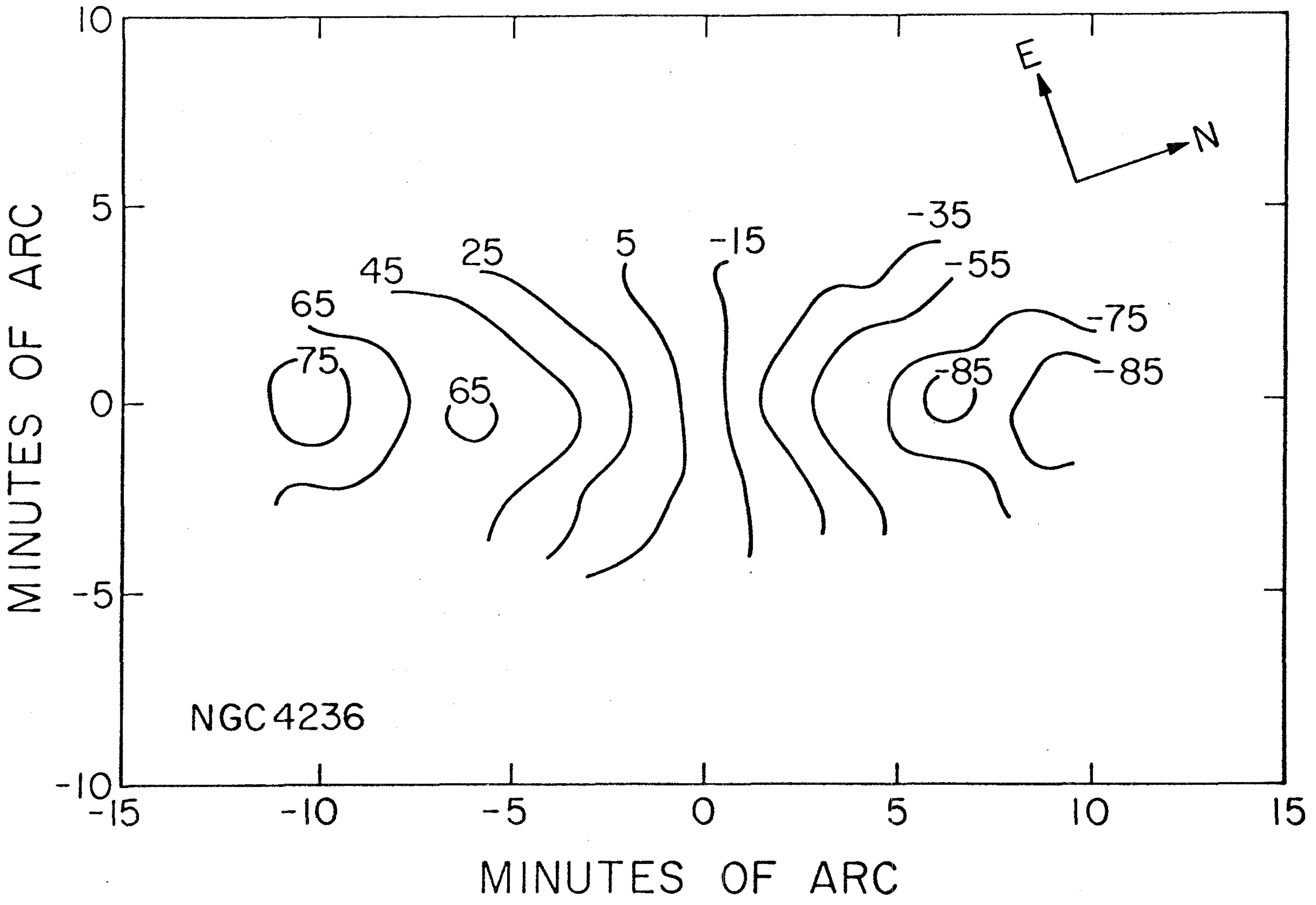

Figure 29. Radial velocity field of NGC4236. Velocities are in km-s^{-1} with respect to sun.

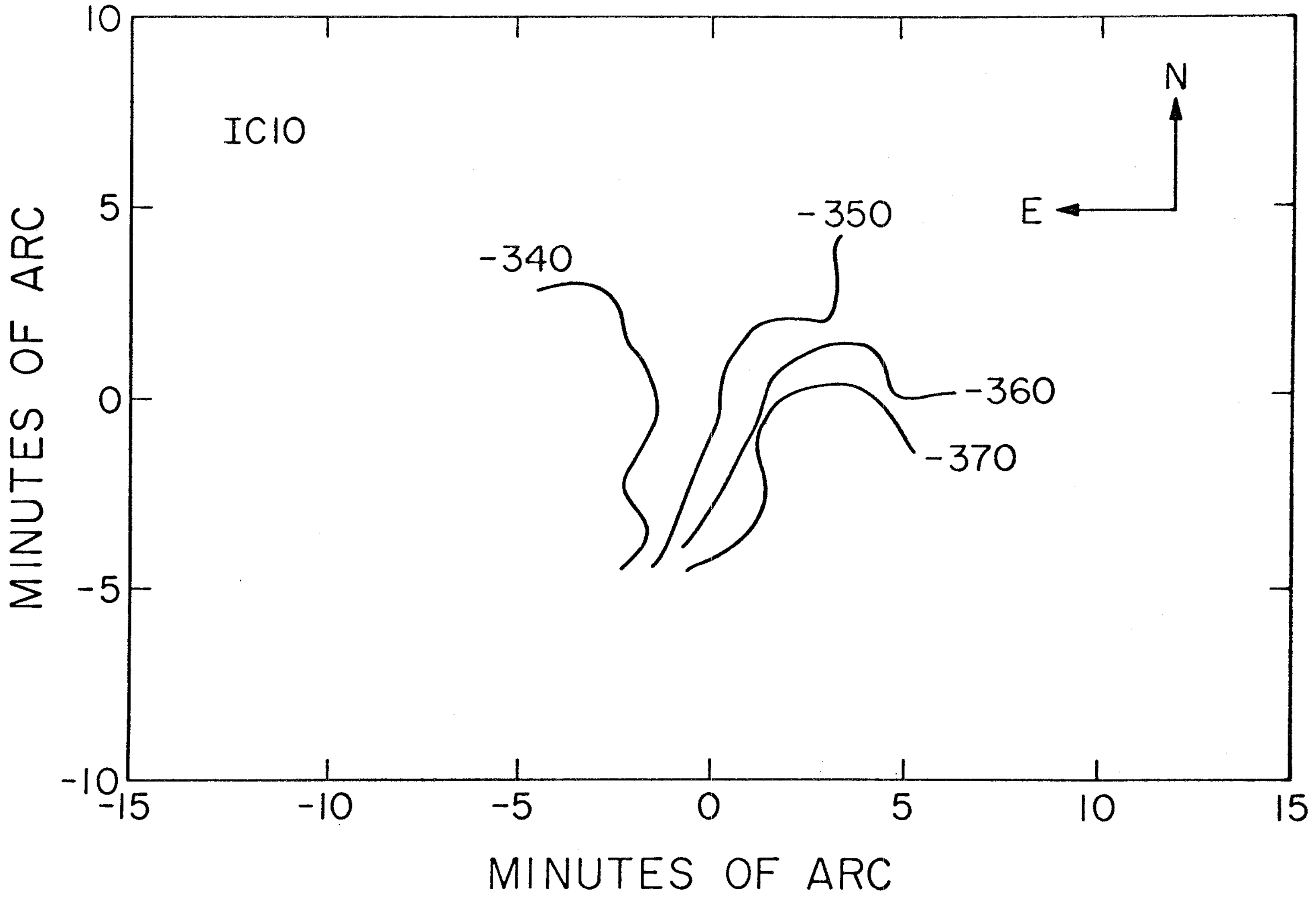

Figure 30. Radial velocity field of IC10. Velocities are in km-s^{-1} with respect to sun.

their major axis position angles. These quantities are interesting not only because they can be compared with similar values obtained by other means, but because of their importance in converting radial to circular velocities. The dynamical centers and position angles of NGC2403 and NGC4236 were determined by demanding the greatest degree of symmetry from their corresponding radial velocity fields. A central position and minor axis were adopted and the r.m.s. velocity difference between points symmetrically placed about this axis computed. Points were chosen on a 1' by 1' grid. When the values resulting in the minimum asymmetry were found, the systemic velocities were read from the dynamic centers. These quantities are listed in Table 9 along with values obtained by others. It should be noted that the systemic velocity for NGC4236 quoted by Humason, Mayall and Sandage (1956) is based on an emission region not located at the galaxy's optical center.

For IC10, whose velocity field is poorly defined due to its narrow line profile, the systemic velocity adopted is the mean value of the radial velocity field (Figure 30). As noted, the position angles listed for this object are obtained respectively from the gradient of the velocity field and from the ellipticity of the hydrogen distribution.

A discussion of the velocity fields of each galaxy and their implied mass distributions follows below.

Table 9

Orientation Parameters

Systemic Velocity[1]

NGC2403	70±40 km-s^{-1}	(Humason, Mayall and Sandage 1956)
	137±5	(Roberts 1962a)
	128	(Rogstad *et al*. 1967)
	133±10	(Guelin and Weliachew 1969)
	125	(Deharveng and Pellet 1970)
	137±5	(Burns and Roberts 1971)
	128±3	present study
NGC4236	27	(Humason, Mayall and Sandage 1956)
	5	(Rogstad *et al*. 1967)
	-10±5	present study
IC10	-343	(Humason, Mayall and Sandage 1956)
	-345±7	(Roberts 1962a)
	-341	(Gouguenheim 1969)
	-350	(Rogstad *et al*. 1967)
	-355±5	present study

Kinematic Center

NGC2403	$07^{h}\ 32^{m}\ 01^{s}.2$	(1950)
	65° 42' 57"	"
NGC4236	$12^{h}\ 14^{m}\ 24^{s}.2$	"
	69° 44' 40"	"

Position Angle

NGC2403	125°.5±1°	
NGC4236	163° ±3°	
IC10	70° ±10°	(HI contours)
	55° ±20°	(velocity field gradient)

---

[1] Velocities with respect to sun.

3. NGC2403 -- Velocity Field

Of the three objects studied, NGC2403 presents the most detail because of its large size and favorable inclination. Examination of Figure 28 immediately shows the high degree of symmetry in the radial (and by assumption, rotational) motions. This is in contrast to an obviously perturbed system such as M101 (Rogstad and Shostak 1971; Rogstad 1971), and is in agreement with the regularity of the optical object. In particular, the systemic (minor axis) contour is quite sensitive to any large-scale non-circular motions. The data suggest that these do not exceed approximately 10 km-s^{-1} over an area comparable to the synthesized beam. In this regard, it should be mentioned again that peculiar motions on a scale much smaller than the beam, for instance a possible nuclear expansion such as is observed in M31 (Munch 1960), are evidently subject to smearing. If, however, they involve sufficient quantities of hydrogen, detection is possible by examination of the narrow-band maps. No such large-scale motions, at variance with the general galactic rotation law, are indicated. This is easily seen by drawing ridge lines through the narrow-band maps and noting the regularity of the derived velocity contours.

The overwhelming characteristic of the velocity field is the practically constant circular velocity seen over much of the object. This is deduced from the radial alignment of the curves of Figure 28 once outside the very central regions. Wright (1971) has shown that large areas of constant rotational velocity are consistent with earlier 21-cm data, and observations of M101 and M33 (Gordon 1971; Baldwin _et al_. 1971) have confirmed their existence in other systems. One infers that in these regions of constant rotation, generally lying outside the most optically luminous part of the galaxy, the total mass (volume) density is falling relatively slowly -- perhaps as slowly as r^{-2}. On the other hand, in the central regions of NGC2403 (within a 2 kpc radius) the velocity gradient is very steep, implying a sharp increase in the central mass densities.

Obtaining a value for the total mass of the object involves the assumption of a mass model. Various models and their associated techniques are discussed by Perek (1962) and Burbidge and Burbidge (1971). Brandt and Scheer (1965) have given functions for calculating mass distributions for galaxies with rotation laws of the form

$$V_{rot} = \frac{V_{TO}\left(\frac{r}{r_{TO}}\right)}{\left\{\frac{1}{3} + \frac{2}{3}\left(\frac{r}{r_{TO}}\right)^{n}\right\}^{\frac{3}{2n}}}, \qquad (6.5)$$

in which n is a parameter governing the shape of the curve, and V_{TO} and r_{TO} are respectively the turnover velocity and radius. This rotation law, despite having no a priori physical basis, has been extensively used in fitting 21-cm velocities, with the parameter n usually equal to 1.5 or 3. The latter value produces a Bottlinger curve, also extensively used. By considering the behavior of equation (6.5) for $r >> r_{TO}$, one obtains for the galaxy's total mass

$$M_T = 6.77 \times 10^{4} D \left(\frac{3}{2}\right)^{3/n} V_{TO}^2 r_{TO} \text{ solar masses.} \tag{6.6}$$

Here D is the distance to the object in megaparsecs, and V_{TO} and r_{TO} are respectively measured in km-s^{-1} and arcminutes. By considering a flattened galactic model built up of differential spheroidal homeoids, and using the above rotation curve, Brandt and Scheer have calculated the resulting mass functions.

A rotation curve was determined using velocity field data within ±67° (on the sky plane) of the major axis of NGC2403. Rotational velocities were obtained from the observed radial velocities by

$$V_{rot} = \frac{V_{rad} - V_{sys}}{\cos\theta \sin i}, \tag{6.7}$$

where θ is measured in the plane of the galaxy from the major axis. Points on a rectangular grid were averaged to produce the curve; off-axis points were weighted by $\cos^2\theta$. The dynamic center, systemic velocity and position angle were as listed in Table 9. The remaining free parameter, the inclination, was then adjusted so that the computed curves had minimal scatter. For the two halves of this galaxy (as defined by the minor axis) the resulting inclinations were

N.W. 58° ± 2°
S.E. 62° ± 2°.

The adopted inclination for the object as a whole was 60°±3°. This is somewhat higher than the value used by most previous investigators (55°) and traceable to Danver (1942). It agrees with that given by Burns and Roberts (1971). The rotation curve is shown in Figure 31.

For the purpose of constructing mass models, a fit of equation (6.5) to the rotation curve was made. Brandt curves were smeared according to (6.4) with the observed major axis hydrogen distribution used for B(x,y). Random motions of 10 km-s^{-1} amplitude, whose effect was to slightly widen the filter widths, were assumed. These "observed" curves were then compared with the rotation curve of Figure 31. The parameters of the Brandt curve were adjusted until this comparison produced the best fit in a least-squares sense. This procedure represents a partial deconvolution of the velocity data and illustrates the fault common to such schemes -- their lack of a unique solution. In this case we have forced the deconvolved curve to be of the form (6.5).

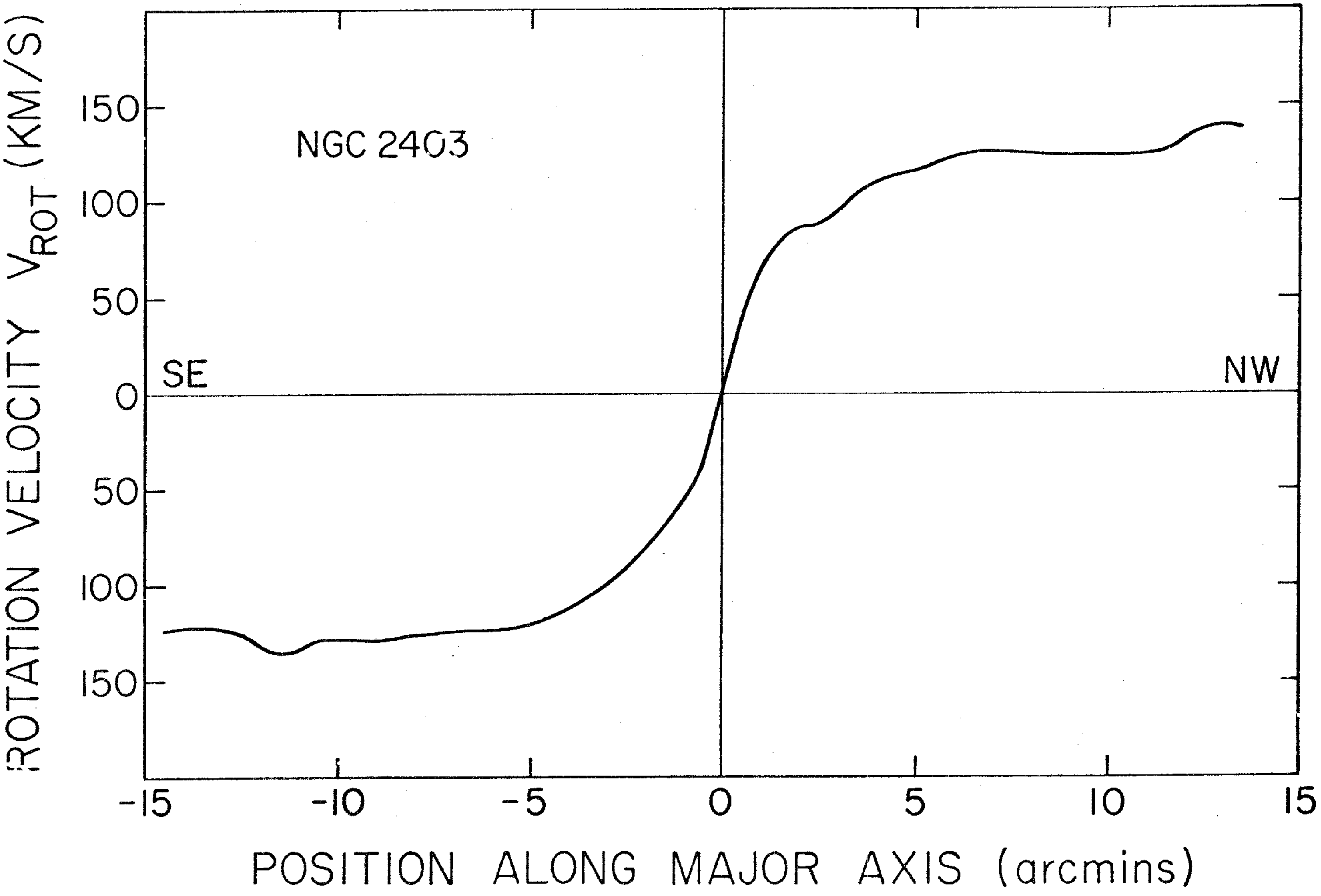

Figure 31. Rotation curve for NGC2403.

The values of the Brandt parameters producing the best fit are listed in Table 10. Curves were actually fit to the two halves of the major axis separately, although the asymmetry was small. By far the most well determined of the three parameters is the turnover velocity V_{TO}. This is rigidly fixed by the extreme points of the galaxy's line profile. The remaining two parameters, n and r_{TO} are strongly coupled. Reasonably good fits to the data could be made with variations in r_{TO} of a factor of two, with suitable adjustments of n. The flatness of the observed rotation curve is the primary cause of this uncertainty. This produces uncertainties of like order in the total mass estimate of equation (6.6), a reflection of the differing behavior of the curves beyond the last data points. A much better determined number is the mass out to the last measured points on the rotation curve. This quantity, also listed in Table 10, remained essentially unchanged with any of the acceptable fits to the rotation curve.

Because of its greater certainty, the bounded mass estimate, 3.6×10^{10} $M_{\odot}$, should be used for comparison with other works. Such estimates are, however, often unavailable and consequently a value for the total mass is listed. That this value is nominally three times the bounded mass implies that we have failed to observe at sufficient radius to see a majority of the galaxy. This observational limit occurs

Table 10

Rotation Curve Parameters and Masses

Object	i (deg)	n	r_{TO} (arcmin)	V_{TO} (km-s^{-1})	r_{max} (arcmin)	$M_T(r_{max})$ (10^{10} $M_{\odot}$)	$M_T(\infty)$ (10^{10} $M_{\odot}$)
NGC2403	60	1.0	9.	126	13.5	3.6	10. 10. (a) 6.4 (b) 5.6 (c) 16.7 (d) 11.8 (e)
NGC4236	75^1	1.5	9.	89	13.0	1.7	3.5 3.0 (c)
IC10	35^2	-	-	-	-	-	0.5^3 1.3^4 (f) 0.54^5 (c) 0.3 (g)

Notes: 1. Danver (1942). 2. Based on ellipticity of HI contours. 3. Keplerian estimate. 4. Assumes i=90°. 5. The 35° inclination derived here was employed.

References: (a) Burns and Roberts (1971). (b) Guelin and Weliachew (1969). (c) Rogstad et al. (1967). (d) Seielstad and Whiteoak (1965). (e) Roberts (1962a). (f) Gouguenheim (1969). (g) Roberts (1962b).

because the hydrogen surface brightness has dropped to the level of the noise in the maps. The total mass is therefore largely an extrapolation, and an implied decrease in the ratio of hydrogen to total mass surface density occurs in the outer regions of the galaxy. Note that the 10% thickness correction to the total mass suggested by Brandt (1960) has not been used here.

Listed in the table are masses obtained by other observers, corrected to a common distance of 3.2 Mpc. In most cases these were obtained by fitting models having rotation laws of the Brandt form to observed velocity profiles. The hydrogen distribution was variously approximated by sums of Gaussians and disks. It should be clear from this investigation that such smooth distributions are unrealistic, and this certainly affects the accuracy of the derived rotation parameters. The sense of this error is to generally underestimate the resolution effects discussed above, thereby deducing values of r_{TO} which are too large. However Guelin and Weliachew (1969) used a centrally peaked hydrogen distribution which led them to consider curves of higher n than found here. Because of the strong interdependence of n and r_{TO}, their values of r_{TO} were lower than other estimates. The values of total mass found by all observers range from 5 - 12 x 10^{10} $M_{\odot}$. However the data are not nearly as disparate as this range would suggest; when the Brandt parameters given by all investigators are used to compute the mass out to 12' radius, the resulting values agree to within 25%.

The only other two-dimensional velocity map of NGC2403 available is that of Burns and Roberts (1971). The loci of constant radial velocity given in this work are much straighter than those of the present study, suggesting a considerably larger area of solid body rotation. This conclusion is fallacious, however, since the loci have been straightened by the larger beam employed (10' diameter). When account is taken of such effects, the velocity data of Burns and Roberts are not inconsistent with those presented here. However there seems to be a systematic shift of their radial velocities to higher values, reflected in the choice of 138 km-s^{-1} as the systemic velocity of the system. This value is 10 km-s^{-1} higher than found here, a difference which is considered significant. The source of the discrepancy is unknown, the slight asymmetry in the hydrogen distribution being an unlikely explanation.

A Fabry-Perot interferometer has been used by Deharveng and Pellet (1970) to determine radial velocities of HII regions near the major axis out to 6' radius. The measurement accuracy of this work is ±6 km-s^{-1}, although the velocity scatter will be much larger due to motions perpendicular to the galactic plane. The data, reflected about the dynamic center and corrected in accordance with the orientation parameters listed in Table 9, is shown in Figure 32. Also shown is the Brandt curve which best describes the HI motions of the present study. Although agreement in the rapidly rising segment of the curve is good, the HII motions are systematically higher than the Brandt curve at 4' radius. The discrepancy is on the order of 15 km-s^{-1}. In light of resolution effects, which can be particularly important at the knee of the rotation curve (Figure 27), one must admit to the possibility that the HI velocities in this region have been underestimated by the amount of the discrepancy. That there exists in this region neutral hydrogen at velocities higher than indicated by the rotation curve can be readily seen by inspection of the major axis velocity profiles. Several of these profiles are displayed in Figure 33. Even though the HI and HII motions are therefore not fundamentally incompatible, it may be that their velocities do in fact differ. The measured regions of Deharveng and Pellet were taken from the Hα study by Veron and Sauvayre (1965), and lie principally along inner spiral arms. In an examination of HII regions in M33, Carranza et al. (1968) found that ionized hydrogen in spiral arms rotated approximately 15 km-s^{-1} faster than in the disk. Because of the narrowness of the arms and their proximity to the nuclear region, they are not easily distinguished in

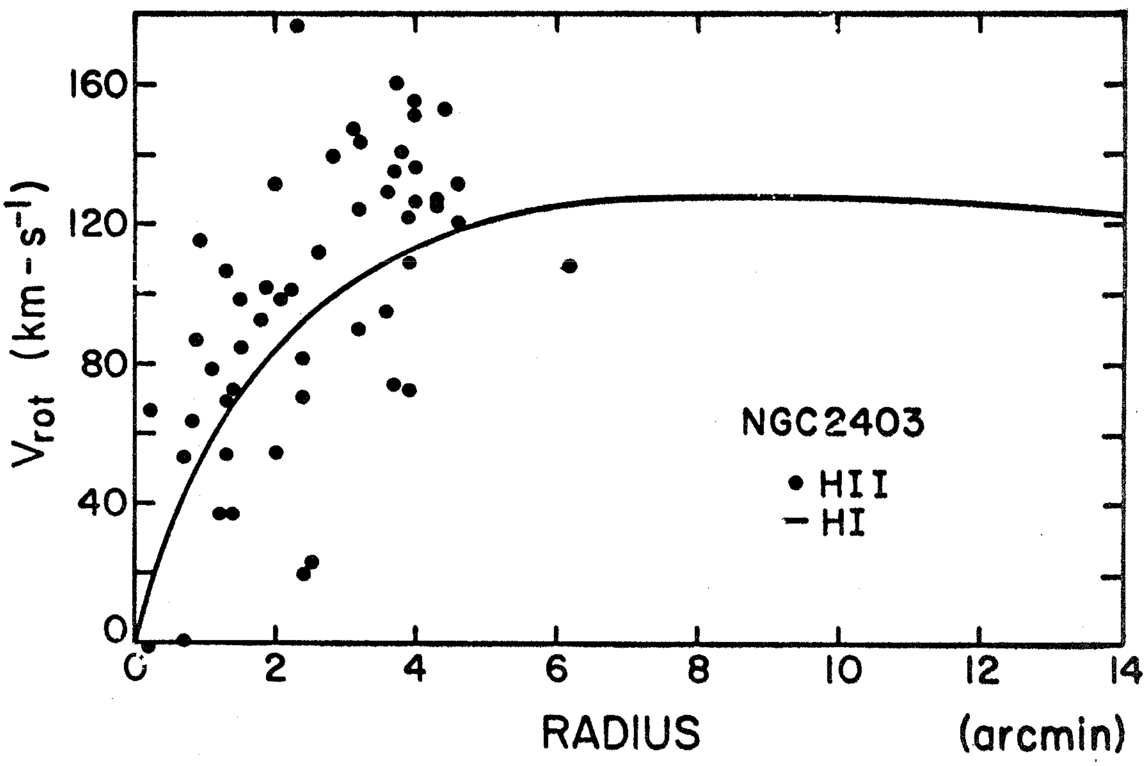

Figure 32. Best fitting Brandt rotation curve (solid line) and Deharveng and Pellet's (1970) HII data for NGC2403.

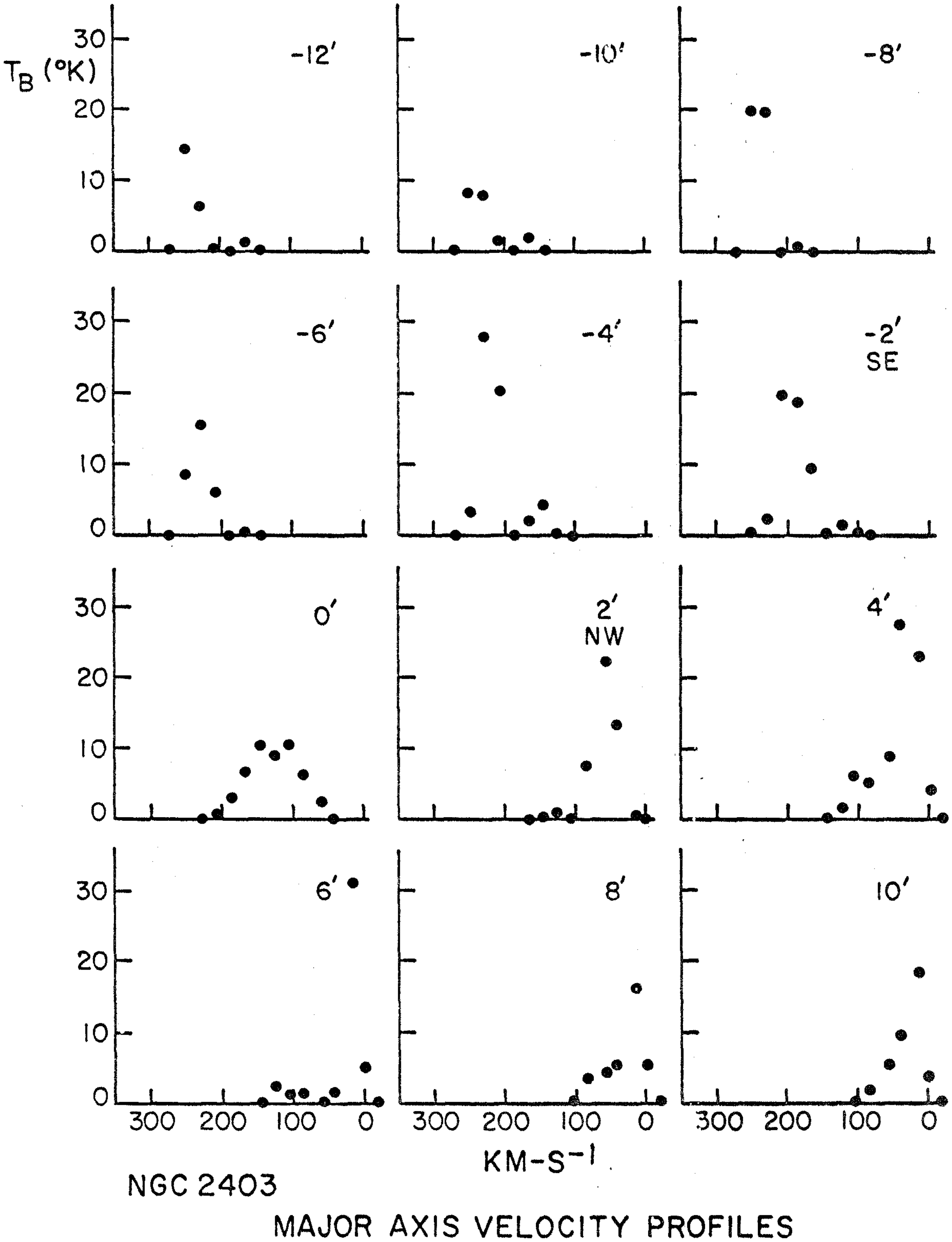

Figure 33. Selected line profiles for NGC2403.

the HI data which must therefore give velocities more typical of the disk. The discrepancy in rotation curves could therefore be due to an observational selection of either disk (HI) or arm (HII) motions, assuming the effect found in M33 applies here. In their study of neutral hydrogen in M31, Gottesman and Davies (1970) found good agreement with the HII rotation curve of Rubin and Ford (1970) except in the region of the velocity turnover in the north-following half where the HII velocities were higher. The discrepancy is approximately 30 to 50 km-s^{-1}, several times that found for NGC2403, but the same fraction of the maximum rotational velocity. This suggests beam smearing effects, although the good agreement between HII and HI velocities in the south-preceding half of M31 is then unexplained.

In conclusion one must say that the mild disagreement between HI and HII velocities in NGC2403, while possibly real, is most simply accounted for by resolution effects. This would not have severe consequences for the total mass estimate, however; the maximum rotational velocity (which appears squared in equation 6.6) is constrained by the limits of the velocity profiles to <140 km-s^{-1}. Furthermore the flatness of the rotation curve is well established by narrow profiles over large areas of the galaxy. A Keplerian tail beginning at, say, 6' radius would reduce velocities by 70% at 12', a reduction which is inconsistent with the data. These constraints respectively bound the total mass from above and below.

The mass functions given by Brandt and Scheer give the run of density with radius shown in Figure 34. The axial ratio was taken to be 0.1 (eccentricity=0.995), the density being inversely proportional to this ratio. The main contours of edge-on spirals give values near 0.08 (Perek 1962), although in a recent study of M33 ratios as high as 0.3 were considered (Boulesteix and Monnet 1970).

An estimate of the flatness of the HI distribution can be made by considering velocity dispersions perpendicular to the galactic plane (z-direction). We assume a Gaussian isotropic dispersion of velocities so that observed profiles are considered representative of z motions. Then

$$\phi(V_z) = \phi_o e^{-V_z^2/2\sigma^2} ,$$

where ϕ is the velocity distribution function. Motions in the z direction are assumed to be decoupled from motions in the plane. One can easily show (see for example Oort 1965) that the resulting gas density has a z dependence of the form

$$\rho_{HI}(z) = \rho_{HI}(0) e^{\int_0^z K_z dz/\sigma^2} .$$

Here K_z is the acceleration toward the plane. For small z the total mass distribution can be approximated by infinite

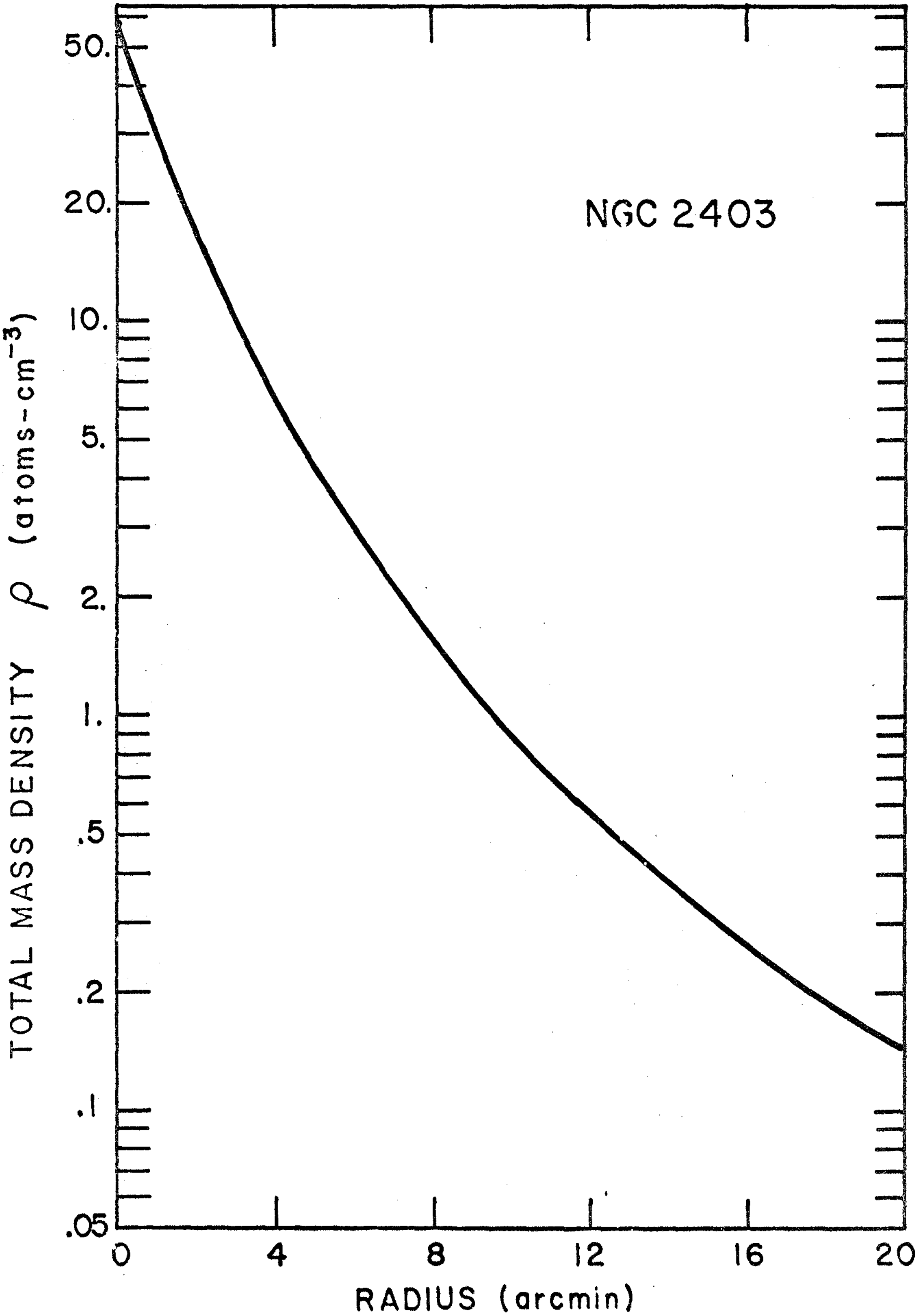

Figure 34. Mass density for NGC2403 from Brandt model.

plane sheets of constant density ρ_o, so that

$$K_z = -4\pi G\rho_o z \ , \qquad (6.8)$$

with G being the gravitational constant. One can then write for the thickness to half-density of the gas layer

$$\text{thickness} = \frac{\sigma \ln 2}{\sqrt{\pi G\rho_o}} . \qquad (6.9)$$

In order to correctly estimate the profile width (2σ), a region of relatively constant radial velocity should be selected. This avoids widening of the profile by differential rotation. Inspection of the profiles at 9' radius along the major axis yields σ=6 km-s^{-1}, when deconvolution with the filter width is considered. Taking the total mass density to be one atom-cm^{-3} (Figure 34), we arrive at a gas thickness of 230 pc. This is comparable to the thickness observed locally in the Galaxy (Kerr and Westerhout 1965). Most of NGC2403's velocity profiles beyond 5' have similar widths, and therefore thicknesses derived from equation (6.9) simply reflect changes in mass density, a rather steeply decreasing radial function. The expected thickening of the hydrogen layer with radius is observed in our own Galaxy (Kerr and Westerhout).

The important point to be made here is that the hydrogen is confined to a relatively thin layer, confirming an important assumption in the interpretation of radial velocities.

The peculiar velocities implied by Figure 28 are discussed in the section on spiral structure.

4. NGC4236 -- Velocity Field

The velocity field of NGC4236 as derived from profile maxima is shown in Figure 29. The general appearance of the field is consistent with differential rotation, similar to NGC2403. However since NGC4236 is probably a barred spiral (see Introduction for discussion of classification), circular symmetry cannot be assumed and care must be taken in interpreting the radial velocities. Indeed a unique interpretation is impossible once the restriction to planar circular motions is abandoned.

The geometry of a barred spiral requires, in addition to values for the inclination (75°, Danver 1942) and major axis position angle (163°, Table 9), specification of the angle in the galactic plane between the bar and the line of nodes (major axis in sky plane). This is easily related to the apparent angle between major axis and bar by

$$\tan\theta_o = \tan\theta_{\mathrm{appar}} \sec i, \qquad (6.10)$$

where θ_o is the desired angle. Measurements of the Sky Survey plate give a position angle for the bar of 163°±2°.

This is the same as the derived kinematic position angle (163°±3°) and hydrogen distribution position angle (161°±3°). The value of θ_o must therefore be $\leq 8°$, and the bar is essentially perpendicular to the line of sight. Motions of the gas along the bar are consequently unobservable.

Velocities within ±8° of the major axis were used as described in the previous section to construct a rotation curve, shown in Figure 35. As before, correction for the galaxy's inclination has been made (planar motions assumed). Because of the unfavorable orientation of NGC4236, an independent determination of i from the velocity field was not attempted. However, since the velocity corrections are small, no significant error is caused by uncertainties in i. The curve is extremely symmetric, the slight disparity in maximum velocities falls within the estimated error of the systemic velocity. The dips at ±7!5 radius are real and extend over most of the galaxy, as can be seen by inspection of Figure 29. In two dimensions these features agree well with the location of the spiral arms. They are suggestive of the peculiar motions associated with the density-wave theory of spiral structure discussed in the last section of this chapter. Over the length of the bar the velocity field is that of solid body rotation with a gradient of 17 km-s^{-1}-arcmin^{-1}. A decrease in rotational velocity occurs beyond 10', as indicated by a shift of the line profiles back

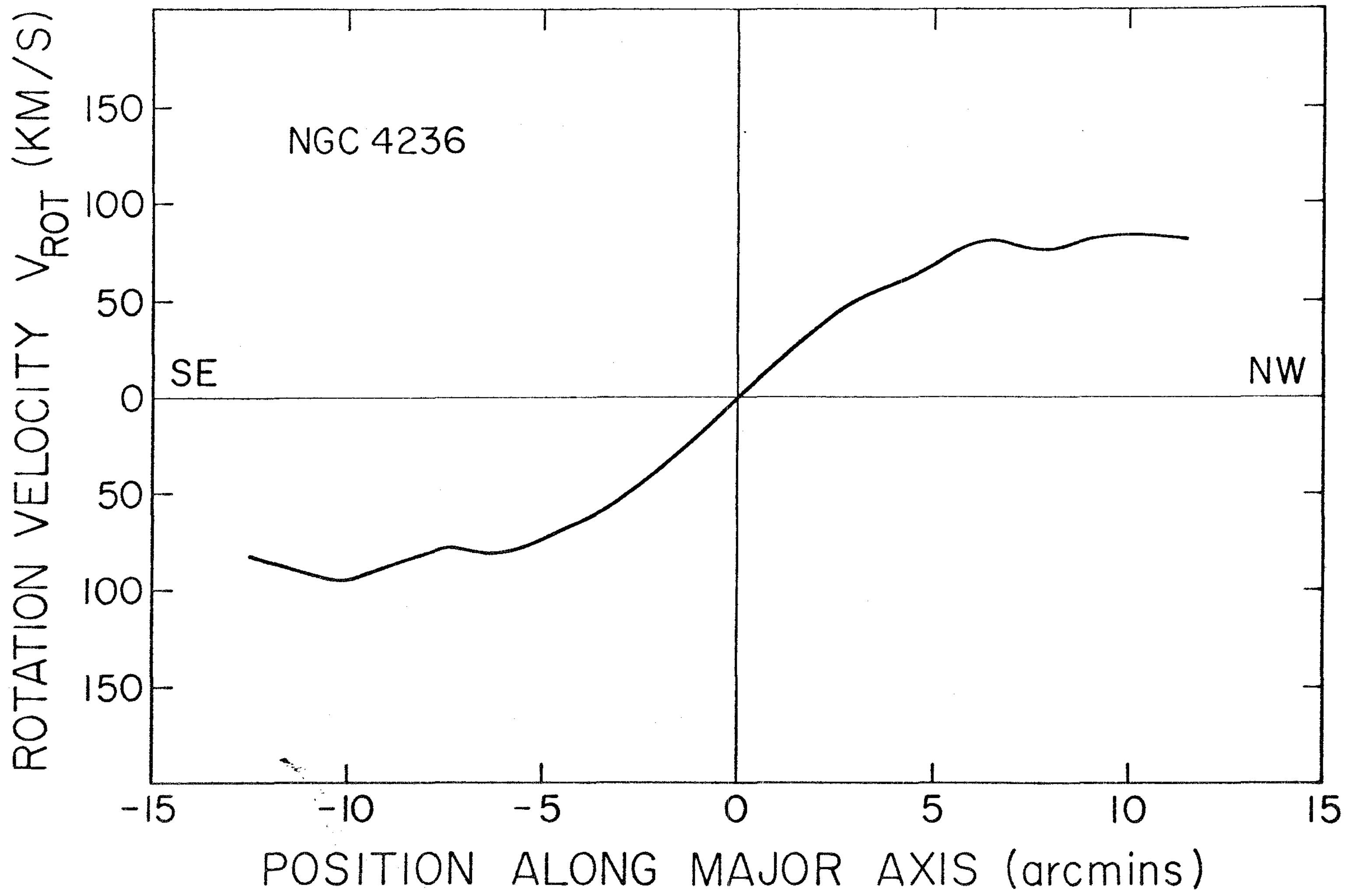

Figure 35. Rotation curve for NGC4236.

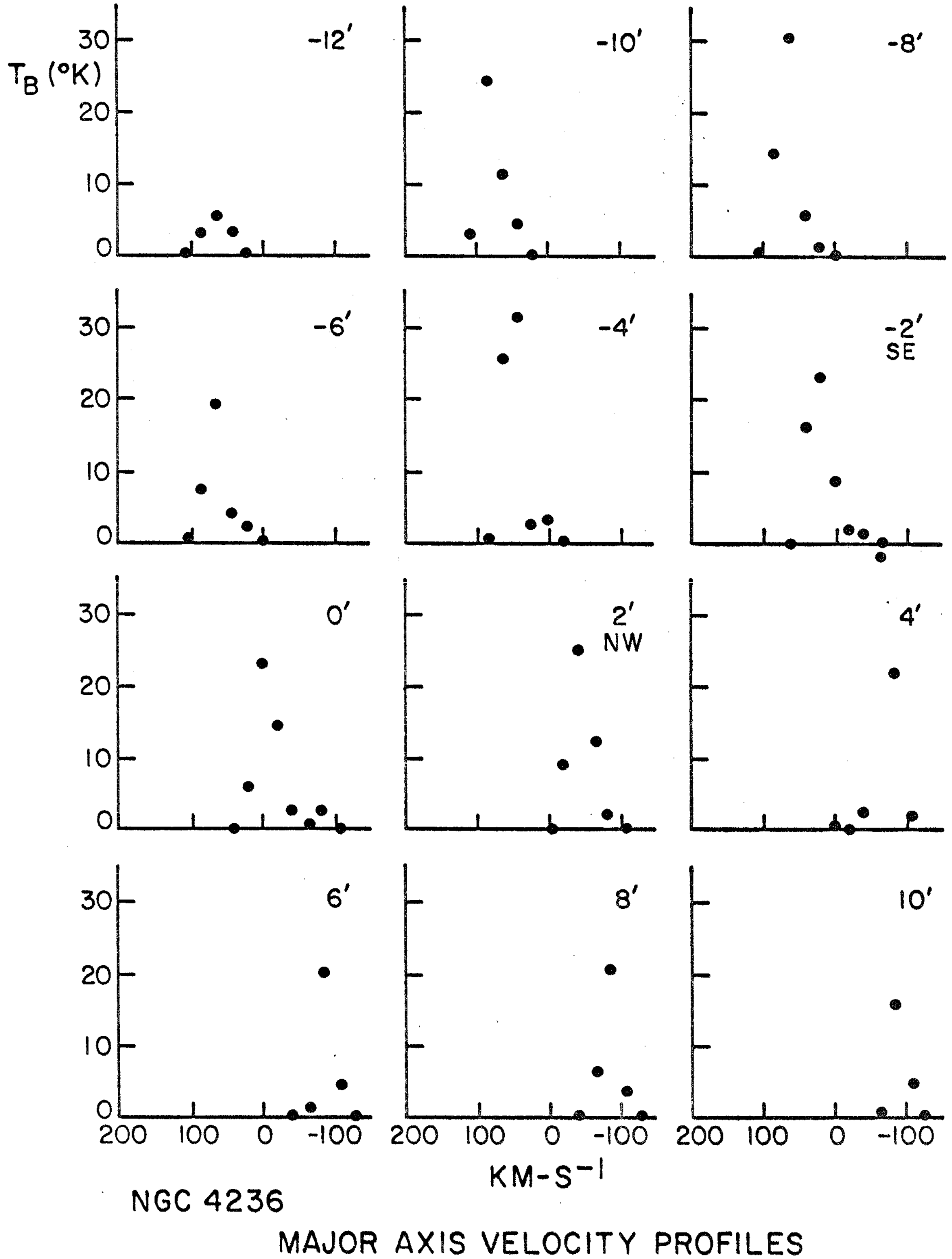

Figure 36. Selected line profiles for NGC4236.

toward the systemic velocity (see Figure 36). The major axis profiles are quite narrow, despite the high inclination, increasing confidence in the accuracy of the derived rotation curve. However, as mentioned in connection with NGC2403, there exists the possibility that the turnover velocity may be underestimated. Examination of the profiles shows measurable flux in channels centered at +106 and -105 km-s^{-1}. This may not indicate hydrogen at these velocities, but rather could be due to overlap of the filters. Depending on the actual velocity profile, between 10 and 20% of the flux in one channel will show up in otherwise empty adjacent channels. Because of velocity structure within one channel, adjacent maps would not necessarily be similar. Random motions will also produce flux in extremum channels which, although real, would be misleading in deriving rotation curves. Both effects are certainly present to some extent, and probably account for the bulk of the observed brightness at +106 km-s^{-1} and approximately half the brightness at -105 km-s^{-1}. It is therefore felt that the radial velocity map and rotation curve cannot be in error (underestimated) by more than 10 km-s^{-1} at their maxima. Uncertainty in the positions of the maxima is not considered to be a serious problem in NGC4236 due to the relatively small velocity gradients.

There is no published optically derived velocity data for this object save the one measurement by Mayall (Humason *et al*. 1956; see also Table 9) of an emission patch 5'.5 S.E. of the center. The measured redshift of 59 km-s^{-1} is in good agreement with Figure 29.

Freeman (1965) has considered dynamic models of barred spirals. Solid body rotation of the bar is assumed in order to avoid distortions within a few revolutions. The motion of the gas, however, is radially outward along the bar, trailing from the ends to produce a two-armed spiral structure. By integrating the gravitational potential of a prolate spheroid, he finds the circular component of the gas velocity increases linearly with radius within the bar and drops approximately as r^{-1} thereafter. Because of the orientation of the bar in NGC4236, the major axis rotation curve gives directly the circular gas velocity. The solid body motion within 4' radius has already been mentioned, and is not only consistent with the assumption but also with the one optical object (NGC7479) for which the rotation over an entire bar could be mapped (Burbidge *et al*. 1960). Rapid fall-off is not possible because of the shortness of the observed velocity tail.

Radial motions of the gas, which are predicted to be more than half the maximum rotational values at twice the bar radius, would be most detectable along the minor axis. Despite the relatively poor spatial resolution in this direction, velocities of this magnitude should give the systemic velocity contour a definite tilt, an effect which is not observed.

One must conclude that the data are not in particularly good accord with the theoretical models.

Because of the absence of axial symmetry, determination of the mass of NGC4236 done in the same way as for NGC2403 might not be justifiable. An estimate of the mass of the bar alone can be made by considering gravitational balance in a uniformly filled prolate spheroid. By balancing the radial acceleration along the bar against the centrifugal force, one arrives at (Burbidge et al. 1960)

$$M_{bar} = \frac{\omega^2 a^3}{2BG} \ . \tag{6.11}$$

The spheroid has axial ratio c/a and angular velocity ω. B is given by

$$B = \frac{3}{4}\lambda^2 \left| \lambda \ \ln\left(\frac{\lambda+1}{\lambda-1}\right) - 2 \right|$$

$$\text{with} \qquad \lambda = \frac{a}{\sqrt{a^2-c^2}} \ . \tag{6.12}$$

For a distance to NGC4236 of 3.2 Mpc and an estimated bar length of 10' with axial ratio c/a=0.1, we find $M_{bar} = 1.3 \times 10^9 \ M_\odot$. This number is uncertain by at least a factor of two, primarily because of the strong dependence on a; reduction of the bar length to 8' halves the mass. Further, uncertainties in the distance enter linearly, and choosing the axial ratio to be 0.2 would increase the mass by 50%. One might also note the crudeness of the model. Nonetheless lack of precision in the estimate should not obscure the fact of the bar's very low mass -- only a percent or so of the total mass of NGC2403. Dividing by the volume of the bar gives a mean density of 13 atoms-cm^{-3}.

Extension of the formulae for the gravitational potential outside the bar to determine the galaxy's total mass seems unjustifiable in view of the flatness of the rotation curve in this region. The best one can do is make a Keplerian estimate based on the outermost measured velocity. Using a point at 12!5 radius (S.E. major axis) with rotational velocity 82 km-s^{-1}, one obtains M_T=1.6 x 10^{10} $M_\odot$. Since this is over ten times the bar mass, the use of axisymmetric models for calculating the large-scale mass parameters is reasonable. A curve of the form (6.5) was fitted to the major axis rotation curve as described for NGC2403. The derived parameters are listed in Table 10. It is interesting to note that the implied Brandt mass interior to 12!5 is identical to the Keplerian estimate above. The extrapolated total mass is 3.5 x 10^{10} $M_\odot$. Note that since the bar structure is ignored in these derivations, they will also apply if the galaxy has been mis-classified and is actually of type Sc. The only other published value for the mass is that Rogstad *et al*. (1967), also listed in the table.

Since the bar contributes so little to the mass of the object, a scheme in which the arms are trailed out by gas escaping from the ends of the bar seems somewhat implausible. This is not to suggest that streaming motions do not exist, however. They provide at least one mechanism for the accumulation of hydrogen at the ends of the bars, an effect seen in NGC4236 (Figure 19), and implied in other systems by the presence of bright stars and HII regions (see Sandage 1961). Such motions have been inferred from optical studies of several barred galaxies (Burbidge *et al*. 1962a, 1962b; de Vaucouleurs and de Vaucouleurs 1963a, 1963b), although frequently the interpretation seems far from unique.

5. IC10 -- Velocity Field

Roberts (1962b) made the earliest study of neutral hydrogen velocities in IC10 and determined the shape of the integrated line profile (see Chapter 3). Since he could detect no shifts with velocity in the position peaks of the hydrogen, rotation of the object could not be established. The possibility therefore remained that the observed velocity dispersion was due to random motions. The more sensitive interferometric data of Rogstad *et al*. showed a systematic phase shift with velocity, thereby reinstating rotation as the most likely description of the general motion of this galaxy. Such a description is confirmed by the present data.

A radial velocity field for IC10, constructed in the same manner as for NGC2403 and NGC4236 is shown in Figure 30. This representation is undoubtedly crude, owing to the relatively small velocity dispersion of the object; hydrogen was detected in only six narrow-band channels. Furthermore, unlike the situation that obtains with the highly ordered velocities of the other two objects, there is a great deal of spatial overlap of IC10's narrow-band maps (Figure 15). Despite the obvious complexities of the motions in this galaxy, several conclusions can still be drawn: There is a definite progression of the maps with increasing radial velocity from south-west to north-east. This is manifested in the approximately parallel radial velocity loci of Figure 30, an effect which is particularly evident over that (southern) region of the galaxy showing optical emission. As is discussed in Section V.6, the presence of a "hole" in the hydrogen distribution suggests that IC10 is a flattened system, and with this assumption the implied motions are circular solid body. Such an interpretation is corroborated by the fact that the velocity gradient, at position angle ∿70°, is reasonably parallel to the apparent

HI major axis (p.a.=55°). The discrepancy could easily be due to the uncertainty in determining this axis, given the almost-circular outline of the object in integrated hydrogen (Figure 21). The divergence of the radial velocity loci in the north could be explained by a bending of the galaxy's plane toward the sky plane, although certainly some of the divergence is distortion of the derived velocities arising from weighting by the HI distribution. Velocity profiles constructed from the narrow-band maps have typical half-widths of ~ 20 km-s^{-1}, further evidence that motions in IC10 are largely confined to two dimensions.

A Keplerian mass estimate, $M_T = 0.5 \times 10^{10}\ M_\odot$, has been made using an assumed distance of 3.0 Mpc and an inclination of 35°. The latter value derives from the measured ellipticity of the total hydrogen map. An independent mass estimate can be made by assuming a ratio $M_{HI}/M_T = 0.22$ for irregular galaxies (Roberts 1969) and using the measured value of M_{HI} (Table 8). The total mass computed in this manner is $0.5 \times 10^{10}\ M_\odot$. In view of the large corrections to the rotational velocity due to the small inclination of this object, the agreement is comforting.

Roberts (1962b) has claimed to have observed narrow (3 - 5 km-s^{-1}) velocity features in IC10 near -340 km-s^{-1} radial velocity. Such features were not observed in the zero-spacing profile (Figure 6), made with 5 km-s^{-1}

resolution. A recent re-examination of the object by W. Wright (private communication) with better signal-to-noise ratios has likewise failed to show the features.

The only published optical Doppler shifts for IC10 are those of Mayall (1941) made in connection with his determination of the systemic velocity, and the Humason, Mayall and Sandage (1956) value listed in Table 9.

6. Peculiar Motions and Spiral Structure

Reference to the derived radial velocity map for NGC2403 (Figure 28) reveals the presence of peculiar motions superimposed on the general galactic rotation. Because of the manner in which this map was produced, some of the perturbations in the velocity loci might be ascribable to distortions caused by irregularities in the hydrogen distribution, and therefore would not represent actual velocity anomalies. A conservative approach to this problem is to consider as real only those anomalies which appear in the individual narrow-band maps. Because of the very narrow sections of the galaxy (except for the extremum channels) picked out by the 21 km-s^{-1} filters, the chance of deception with this procedure is small. Indeed, because of smearing by the beam, velocity kinks seen in these maps will actually tend to be reduced in amplitude from their true values.

Inspection of the maps (Figure 13) shows virtually all the peculiarities in the radial velocity loci south of the major axis are clearly present in the individual channels. This does not include the very ends of the loci which, because of the decrease in HI surface brightness, are not well determined. Nor does it include the extremum channels where the reality of velocity perturbations is difficult to assess due to the extended nature of the maps. The principal feature is a ridge of higher radial velocity approximately 5' south of the galactic center running normal to the loci. At a slightly greater radius is a parallel ridge of lower radial velocity. The resulting "wave" behavior of the loci is most evident in the systemic velocity contour (128 km-s^{-1}), suggesting that the peculiar velocities are radial motions in the plane of the object. Location of the high velocity ridge coincides with a well-defined spiral arm. This can be seen in Figure 37 in which the velocity map has been superimposed on a Palomar Sky Survey photograph of NGC2403.

The density wave theory of spiral structure requires peculiar motions of both stars and gas near spiral arms (Lin, Yuan and Shu 1969). In the linear theory, the peculiar motions vary sinusoidally:

$$u_r = -a_r \cos\{2\theta - \phi(r)\}, \qquad (6.13)$$

$$u_\theta = a_\theta \sin\{2\theta - \phi(r)\}, \qquad (6.14)$$

where u_r and u_θ are respectively the radial and azimuthal components of the peculiar velocity (θ is measured in the direction of rotation). The phase of the periodic functions is zero ($\phi=2\theta$) along the spiral gravitational potential minimum. A two-armed trailing spiral is assumed, and is given by

$$r = r_o e^{-\tan t(\theta-\theta_o)} \quad , \tag{6.15}$$

where t is the angle between the spiral and a galactocentric circle. The amplitude coefficients a_r and a_θ are given by Burton (1971) and have been used by Rogstad (1971) in his description of peculiar motions in M101. The observed velocities in M101 are typically 5 - 8 km-s^{-1}, or 11 - 18 km-s^{-1} in the plane of the object. To account for such large motions using the linear theory, Rogstad was compelled to choose a co-rotation point at 35', more than twice the Holmberg radius for this object. (The co-rotation point is the radius at which the pattern speed of the density-wave equals the material rotation speed.)

From a theoretical point of view, larger streaming motions are expected than those given by the linear theory. Non-linear effects have been investigated by W. W. Roberts (1969). Rather than large-scale smooth variations in gas compression, he proposes the existence of galactic shocks in the usual spiral pattern given by equation (6.15). Such shocks provide a high compression over a short distance, thereby facilitating star formation along narrow arcs, an observed characteristic of many spirals. A further observational consequence would be the situation of the highest gas densities on the outside of the arc of luminous stars and HII regions delineating the shock, but because of the limited resolution available in this study such an arrangement cannot be verified. The shock produces a very high localized gas compression (5 to 10 times the usual density), and streaming (peculiar) motions of about a factor of two larger amplitude than those of the linear theory.

The behavior of the gas is given by Roberts' analysis. We decompose the motion into velocities perpendicular and parallel to the spiral shock. The perpendicular velocities increase in amplitude as the hydrogen approaches the potential minimum, dropping sharply at the shock, and then slowly rising again as the next minimum is approached. Velocities parallel to the shock exhibit complementary behavior, decreasing as the minimum is approached. These motions may be reasonably approximated by periodic ramp functions, discontinuous at the shocks (see Figure 5 of Roberts' paper). Since the pitch angle of the spiral arms is small, the motions perpendicular and parallel to the shock are nearly the same as the radial and azimuthal gas velocities. Consequently the peculiar motions (the motions described above minus the differential circular velocity) become radially outward on the inside of the arms, and inward on the outside of the arms. The azimuthal motion is counter to the general rotation on the inside of the arm, and adds to it on the outside.

The maximum amplitude of the peculiar motions is proportional to the average speed at which the gas moves through the spiral pattern, evidentally $(V_{rot}-\Omega_p r)$, where Ω_p is the pattern speed (angular velocity). The constant of proportionality is approximately 2tan t (Quirk, private communication). This corresponds to the solutions given by Roberts for a spiral potential field which is 5% of the general axisymmetric field. We may therefore estimate the expected size of the velocity anomalies in NGC2403. The rotational velocity $V_{rot}(r)$ is determined from the Brandt curve with parameters as found in Table 10. The tilt angle t can be measured on the photographs: for the prominent southern arm it has the average value t=18° (Danver 1942 lists 14°). Lin (1970) has suggested that the spiral pattern originates in the outer regions of the galaxy via clumping and shearing of the interstellar gas. The pattern speed is then obtainable as the angular rotational velocity where the spiral-defining HII regions end. This choice of Ω_p has been investigated for several nearby galaxies by Shu, Stachnik and Yost (1971) with favorable results. For NGC2403, the pattern speed derived in this way is 10.5 $km\text{-}s^{-1}\text{-}kpc^{-1}$.

With the above assumed parameters, the maximum expected streaming motions at the radius of the southern arm (9 kpc) near the minor axis should be 20 $km\text{-}s^{-1}$ which, after correction for inclination, implies a line-of-sight amplitude of 17 $km\text{-}s^{-1}$. The observed amplitude has a peak value of 8 - 10 $km\text{-}s^{-1}$. When allowance is made for resolution effects, this is certainly compatible with the expected value.

To better compare observed and predicted behavior, a computer model, shown in Figure 38, was made of a radial velocity field which included peculiar motions appropriate to a spiral pattern in accord with the optical image of NGC2403. Ramp functions were used to approximate the streaming velocities. General rotation of the galaxy was of the Brandt form with parameters listed in Table 10. Ω_p and t were as determined above. To allow for beam smearing, the computed radial field was convolved with a Gaussian of 2' half-power width. This is the synthesized beamwidth; however it should be noted that convolution of the velocity field, done for computational simplicity, is only an approximation to the actual resolution effects as given by summing equation (6.4) over all channels. It was previously shown that the accuracy of the derived velocities depends on the smoothness of both the velocity gradient and the actual

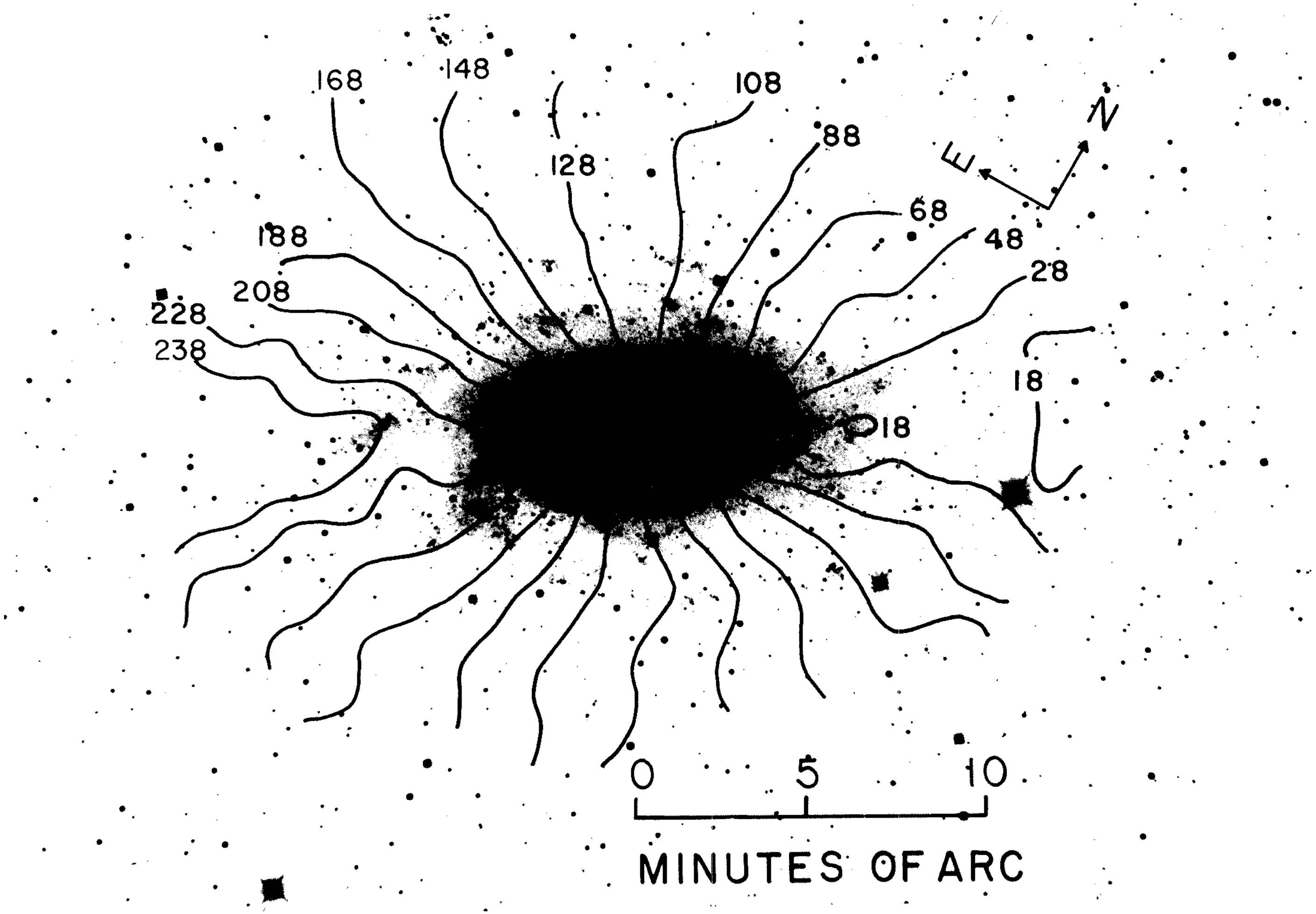

Figure 37. Radial velocity field for NGC2403 superimposed on (blue) Sky Survey print.

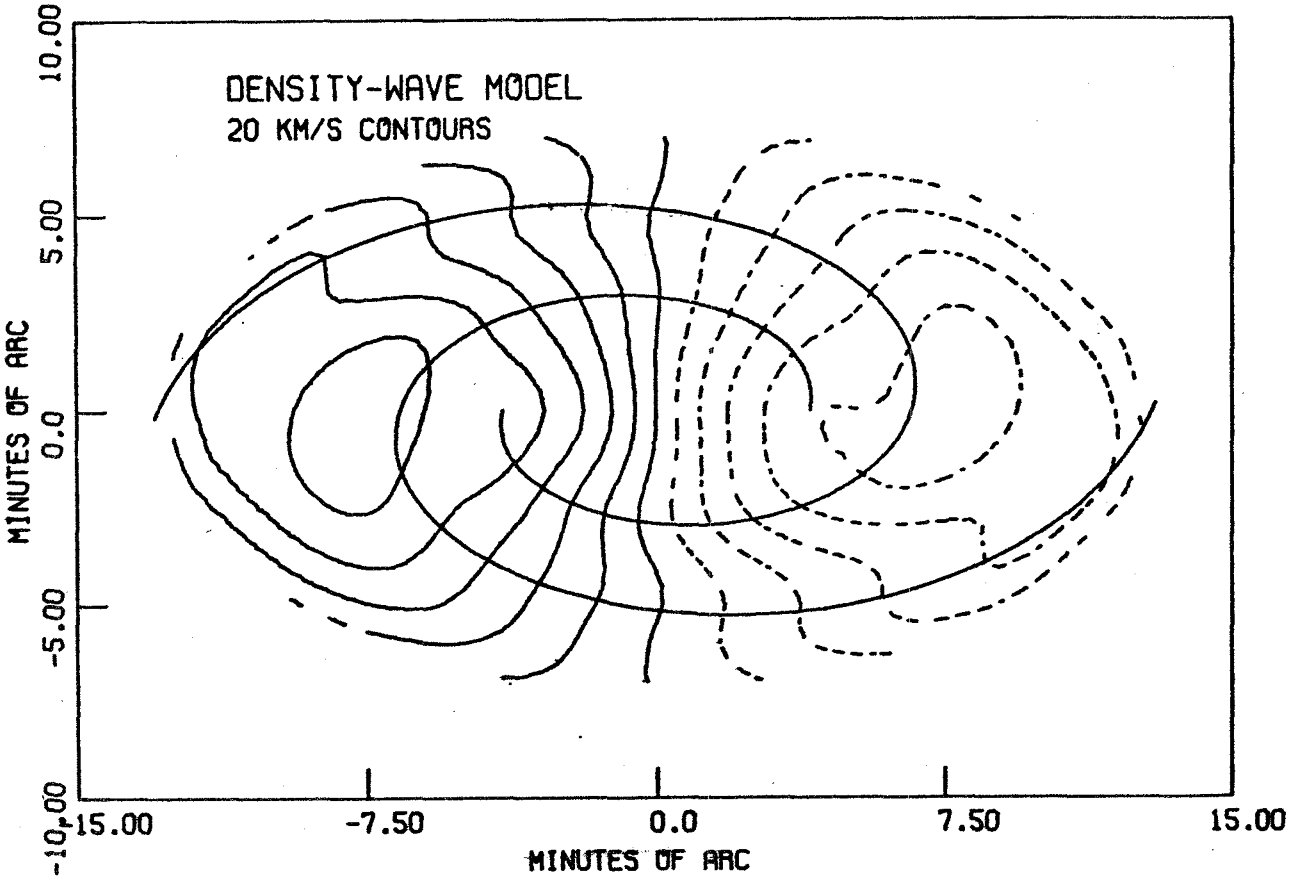

Figure 38. Computer model velocity field for NGC2403 using non-linear density-wave theory. Maximum streaming motions are 20 km/sec. The rotation curve is of the Brandt form with parameters as listed in Table 10. This model should be compared with Figure 37.

HI distribution. Reference to the total HI maps (Figures 17 and 18) shows that the observed distribution in the southern arm region is relatively smooth, implying that the derived velocities are not too severely smeared. Furthermore, since the maximum of the HI density occurs at the maximum positional displacement for any given velocity (at the shock front), beam effects are somewhat counterbalanced.

The model field is seen to be in generally good accord with the observed field in the region south of the major axis. Furthermore, the double-wave behavior which occurs when two arms are a beamwidth or so apart can be seen in the data north of the axis along contours at 228 and 238 km-s^{-1}. There also seems to be some evidence in the observations for the "pinching" of extremum loci near the major axis because of azimuthal motions.

In summary, we conclude that peculiar velocities, especially radially in the galactic plane, are certainly present in the data. Their location, direction and magnitude are consistant with those predicted by the density-wave theory if we take into account expected non-linear shock phenomena.

A recent refinement of the non-linear theory to include the effects of magnetic fields (Roberts and Yuan 1970) shows little alteration of the anticipated peculiar motions and only a slight reduction in the expected gas compression.

VII. INTEGRAL PROPERTIES AND DISCUSSION

1. Integral Properties

Integral quantities and ratios are useful for describing variations among different classes of galaxies. Values derived during the course of the present study are listed in Table 11, together with several other parameters. It should be borne in mind that every one of the listed integral ratios is an average value of quantities which vary substantially over the galactic disks.

Determination of the intrinsic luminosities of the present galaxies is complicated by distance uncertainties and the degree to which the apparent magnitudes are affected by Galactic and internal absorption. The absolute photographic magnitudes and associated luminosities listed in Table 11 were determined as follows: For NGC2403 Holmberg (1958) lists $m_{pg}=8.80$. Correction for Galactic absorption is usually made by assuming a dependence proportional to the cosecant of Galactic latitude (Hubble 1934). Unfortunately, the absorbing medium is patchy, and use of the cosecant law may lead to large errors in individual cases. Tammann and Sandage (1968) have determined the color excess in the direction of NGC2403 to be $E_{B-V}=0\overset{m}{.}06$, so the implied absorbtion ($4E_{B-V}$) is $0\overset{m}{.}24$. Together with their absolute distance modulus to this object ($27\overset{m}{.}55$), this leads to an absolute

TABLE 11

Summary of Integral Properties

	NGC2403	NGC4236	IC10
Classification (de Vaucouleurs 1964)	SAB(s)cd	SBdm	IAm
(van den Bergh 1960)	Sc III	SB$^+$IV or Ir$^+$IV	Ir$^+$IV?
Distance D (Mpc)	3.25	3.25	3.0
Hydrogen mass M_{HI} ($10^9 M_\odot$)	3.5	1.5	1.0
Bounded mass to $13\overset{\prime}{.}5$ M(r') ($10^9 M_\odot$)	36.	17.	--
Extrapolated total mass M ($10^9 M_\odot$)	100.	34.	5.
Absolute mag. M_{pg}	$-19\overset{m}{.}2$	$-17\overset{m}{.}8$	$-18\overset{m}{.}5$†
Luminosity L ($10^9 L_\odot$)	6.7	1.8	3.5†
$M_{HI}/M(r')$	.097	.088	--
M_{HI}/M_T	.035	.044	.20
M_{HI}/L	.52	.82	.29
$M(r')/L$	5.4	9.5	--
M_T/L	15.	19.	1.4

†See text.

magnitude of M_{pg}=-19.0. Holmberg's data suggest a correction to a face-on inclination of $0^{m}_{.}2$ (not including internal absorption independent of inclination), therefore M_{pg}=-19.2 as listed in the table. This is practically identical to Tammann's (private communication) revised mean value of $-19^{m}_{.}3$ for objects of luminosity class III (van den Bergh 1960). The conversion to solar luminosities assumes $(M_{\odot})_{pg}$ =5.37 (Stebbins and Kron 1957).

The same procedure was adopted for NGC4236, for which Holmberg lists m_{pg}=10.05 and the distance modulus from Tammann is $27^{m}_{.}4$. Negligible Galactic absorption is seen in the direction of this object. Formally, the inclination correction is large since i=75°; however, partly because NGC4236 is barred and partly because it is of luminosity class IV, the indicated correction is probably excessive. Only half the formal amount was used to compute the tabular value, M_{pg}=-17.8. This is identical to the revised mean value for luminosity class IV.

The intrinsic luminosity of IC10 is somewhat controversial; its location in the zone of avoidance requires assumptions about its colors in order that Galactic absorption can be computed. UBV photometry by de Vaucouleurs and Ables (1965) yielded an apparent blue magnitude of 11.8. However, assuming the object is similar to the Magellanic irregulars, a color-color plot shows IC10 to be very substantially reddened, with a color excess of $E_{B-V}=0^{m}.77\pm.07$ (note that computational errors in the work cited caused the authors' listed value to be larger by $0^{m}.03$). The implied blue absorption is $3^{m}.1\pm0.3$, and with the adopted distance modulus of $27^{m}.4\pm0.5$, we find $M_{pg}=-18.5\pm0.7$, after conversion to photographic magnitudes following the precepts of the Reference Catalogue (1964). This is as bright as the Large Magellanic Cloud (de Vaucouleurs 1960) and 0.7 magnitudes brighter than the mean class IV object. The dispersion within a luminosity class is $0^{m}.5$, so that the discrepancy is within one standard deviation of the combined errors. It is possible that the absorption has been overestimated; Zwicky has pointed out an (unmeasured) field of blue stars in IC10 which suggests little absorption in that direction (see Roberts 1962b).

Table 11 lists the fractional hydrogen masses and the several mass-luminosity ratios for the objects of the present investigation. The fractional mass shows the well-known variation with type, although the values for NGC2403 and NGC4236 are about half those listed by Roberts (1969) as typical for similar objects. We remark that Burns and Roberts' (1971) work on NGC2403 produced a fractional mass close to the value found here. IC10 has a value typical of irregulars. The two mass-luminosity ratios are consonant with Roberts' listed averages except in the case of IC10.

For this object the ratios are low, suggesting that the tabular luminosity is an overestimate. Note that the ratio M_{HI}/L is independent of distance, and its anomalously low value for IC10 reinforces the belief, stated earlier, that Galactic absorption is not as great as claimed. The quantities M_{HI}/M_T and M_T/L are respectively proportional to the distance and its inverse. We would expect that the current upward revision in galactic distances (Tammann and Sandage 1971) will adjust accordingly the average values of these ratios as given by Roberts. Curiously, such an adjustment would move the average values further from those found here.

The table also lists ratios employing the bounded mass estimates discussed in Chapter 6. Naturally, these ratios have a greater certainty than those employing the (extrapolated) total masses. Note in both cases the lower mass to luminosity ratio of NGC4236 in comparison with NGC2403.

Examination of the mass-luminosity ratios observed in spiral and irregular double galaxies by Page (1962) shows them to be considerably less than those found here. For a Hubble constant of 60 km-s^{-1}-Mpc^{-1}, Page lists $\langle M/L \rangle = 1.7$, or if only his high-weight objects are considered, $\langle M/L \rangle = 0.7$. However the mean masses for these two groups were only 6.1×10^{10} $M_\odot$ and 2.2×10^{10} $M_\odot$ respectively, implying a large fraction of low mass objects. Coupled with a possible observational bias towards high luminosity systems, one might be able to account for the discrepancy in ratios.

2. Hydrogen Distributions

The present study shows the HI extent of galaxies to be essentially the same as the optical. This is in contradiction to previous thought, which held that the hydrogen was considerably more extended (see Roberts 1966b). The low resolution aerials used in earlier studies are undoubtedly responsible for this misconception.

To a great extent the reduction in HI size has ameliorated the rather jarring discrepancies between the distribution of neutral and ionized hydrogen formerly proposed (Hodge 1969). We have demonstrated in this work the very good positional coincidence of HII regions and HI concentrations in the presently observed galaxies. Nonetheless, the HI distributions are of considerably greater extent than those of the ionized gas (Figure 23). Hodge (1967) has pointed out that the number of HII regions in a galaxy is directly proportional to its total neutral hydrogen mass. Since the HII regions occupy only a fraction of the volume taken up by the HI, Hodge's result forces us to conclude that the number of HII regions in an object, and therefore the formation rate of the bright stars, is macroscopically rather than microscopically dependent on the HI distribution. To a certain degree this is in contradiction to an earlier statement concerning the role of density-wave shocks. It was suggested, after W. Roberts (1969), that the formation of Population I material was the result of a very large compression of the interstellar HI as it passed through a density-wave minimum. Such a scheme evidently relates the birth rate of bright stars to the local HI density, a seemingly very microscopic quantity. However, Lin (1970) has proposed that generation of the density wave is caused by clumping of the hydrogen in the exterior regions of the galaxy. To first order, then, Hodge's correlation simply reflects the larger area of influence of the density-wave shocks for objects of greater HI mass. Furthermore, these objects will have lower pattern speeds, and the gas compression, which is proportional to $(\Omega-\Omega_p)$, will be greater and consequently more effective in the formation of the Population I material. We conclude, then, that while the production of hot stars requires locally high gas densities, the extent and amplitude of the shocks causing such conditions is governed by the large-scale distribution of the HI.

Recent high resolution HI studies of M31, M33, M101 and the Large and Small Magellanic Clouds, when combined with the present work, allow us to inquire into the existence of a correlation of overall hydrogen distribution with galactic type. Evidently our sample is small, and any conclusions must be regarded as tentative. Nevertheless, it is useful to review those HI morphological features which appear to typify a given class of objects.

We begin with the irregulars. They are characterized by small areas of high brightness immersed in an extended region of considerably lower emissivity. The peaks, which are probably saturated, show good positional agreement with HII regions. Columnar line-of-sight densities for the low-level regions range from 1 - 2 x 10^{20} cm^{-2} in the LMC (McGee and Milton 1966) to 10 and 20 x 10^{20} cm^{-2} for IC10 and the SMC (Hindman 1967) respectively. The LMC has been classified as an SB(s)m system by de Vaucouleurs (1961), and is therefore not fairly compared with the other objects. Confirmation of a distinction between the LMC and irregulars is drawn from its fractional HI content, which is only 5 - 10%. For IC10 and the SMC, the figure is 20 - 30%. When allowance is made for inclination effects, the general HI surface brightnesses of IC10 and the SMC are quite similar, as are their masses. They both show three principal emission peaks. Because of the general regularity of their velocity fields, they are suspected of being flattened systems, an hypothesis strengthened by the presence of the "hole" in IC10. The degree of flattening is not known, although the statistical investigation of Hodge and Hitchcock (1966) indicates that typical axial ratios for irregulars fall in the range 0.2 - 0.4.

The barred spirals are poorly represented; the barred nature of the LMC is subtle, and NGC4236 presents itself in a most disagreeable orientation. The latter object shows hydrogen concentrations coincident with the major HII regions at the ends of the bar and at points along the spiral arms. Explanation of these concentrations as due to an outflow of hydrogen along the bar could not be verified. Surface densities (corrected for inclination) in the bar region are $\sim 4 \times 10^{20}$ cm^{-2}, with a mild peaking toward the center. The fractional HI mass of the bar is $\sim$20%, substantially higher than the object as a whole. Since the HI mass of the bar represents less than 20% of the hydrogen content of the galaxy, it seems that distinction between barred and normal spirals solely on the basis of their HI distributions is unlikely. The extensive region of solid body rotation, a requirement for the persistence of a non-axisymmetric geometry, has already been noted for NGC4236.

The spirals, particularly of type Sc, comprise the largest observed group of objects. They have been studied with resolutions ranging from 400 pc for M33 (Baldwin _et al_. 1971) through 2 kpc for M31 (Davies and Gottesman 1970) and NGC2403, and up to 8 kpc for M101 (Rogstad and Shostak 1971), assuming the distance to the latter is 6.9 Mpc (Tammann, private communication). Again, a patchy structure is evident; the maps tend to be dominated by peaks and ridges. Correlation of these regions of high σ_{HI} with Population I material is usually good, although hardly one-to-one. As many of the peaks are unresolved with the presently available beamwidths, and since the velocity dispersion over the small areas involved is probably ≤ 15 km-s^{-1} (see Chapter 6), we can expect these regions to be optically thick.

Outside of the peak regions, the three Sc objects show considerable similarity in the value of their maximal HI surface densities. They all attain a value of about 10×10^{20} cm^{-2} somewhere in their average radial distributions (Gordon's 1971 data for M33 were used here). These densities are, of course, distance independent, and the inclination correction introduces only a small uncertainty. The values reached in M31 (type Sb) are two to three times less, and this is in keeping with the well known decrease in fractional HI mass content with earlier type (Roberts 1969). Care must be exercised in speaking of surface densities because of the obvious selection effects, although a fair range of inclinations is present. The value of σ_{HI} quoted above applies to Sc galaxies having at least a 10 to 1 range of HI and observable total mass. The variation of σ_{HI} with type has been found using low resolution data by Roberts (_op. cit._) and Gouguenheim (1969). If the extreme uniformity within a type presented here holds up, then σ_{HI}

would be a sensitive classification criterion. We note that the maximum average surface density in our own Galaxy (Oort 1965a) is halfway between that of M31 and the Sc's. This is consistent with de Vaucouleurs' (1964) classification of the Galaxy as Sbc, based on the appearance of the spiral pattern.

Historically the feature of hydrogen distributions receiving the most attention has been the existence (or non-existence) of a central "hole". Usually described as an HI ring, this type of distribution was thought to be present in most spirals (Roberts 1967). However, as discussed in Chapter 5, this conclusion was partially based on a rather insensitive observational criterion. Detection of holes requires two-dimensional examination with small beams, and therefore discussion should be confined to objects observed in this way. We find that M31, M101 and the Galaxy have substantial central depressions whereas M33 does not. In the present study we have concluded that NGC2403 is closer to M33 in its central σ_{HI} distribution than to the others. The possible causes of holes were discussed in Chapter 5; discrimination among them being presently impossible. As mentioned, Rogstad (1971) has suggested that an extended ionized region accounts for the lack of central HI in M101. It is our opinion here that such an explanation is unconvincing when applied to the general phenomenon of holes. In his summary of Hα observations in spirals, Monnet (1971) reports the existence of an ionized disk in M101 and M33, but not in NGC2403 or M31 (values of EM less than 20 and 10 cm^{-6}-pc respectively). Correlation of holes and generalized Hα radiation is therefore only 50%. A more consistent correlation obtains between holes and high mass systems. The observed masses of M33 and NGC2403 are 5 to 10 times less than for M101, M31 and the Galaxy. This suggests that the holes are caused by the hydrogen layer thickening with radius, discussed in Chapter 5. Unfortunately, this explanation seems to fail in detail. In the central galactic regions we may characterize the rotation curve as solid body with slope $\frac{\partial V}{\partial r}=\Omega$. For such a curve, the mass density ρ is constant with radius, and of magnitude proportional to Ω^2 (equation 7.2). The HI scale height, given by (6.9) is consequently proportional to Ω^{-1}. Therefore if we assume the central decrease in σ_{HI} is due to compression of the HI layer by high central mass densities, we should observe a reciprocal increase in Ω along the mass sequence. This is not consonant with the data. Velocity gradients in the galactic planes of M33 (Baldwin _et_ _al_.'s data), NGC2403 and M101 are respectively 137, 64 and 50 km-s^{-1}-kpc^{-1}, averaged over the respective beamwidths: precisely the reverse order one would expect from the thickening argument. It might be thought that these values simply reflect the decreasing relative resolution of the observing beams, and this is partially true. However, the depression in M101 is at least one beamwidth wide, and we require a large value of Ω over a comparable distance. The maximum observed radial gradients in NGC2403 are 52 km-s^{-1}-arcmin^{-1} over a beamwidth; for M101 the number is 25 km-s^{-1}-arcmin^{-1}. If M101 had a high mass density over its central 4', a higher gradient would have been observed.

We may say, then, that while higher resolution studies will undoubtedly steepen the innermost regions of the rotation curves, a high mass density extending over the region of the HI "hole" in M101 seems impossible. The thickening mechanism as an explanation for the correlation of central depressions with galactic mass appears untenable.

Another point of comparison among galaxies is the manner in which σ_{HI} drops off at the edge of the galaxies. For M33, Baldwin et al. report a very sharp edge with an e-folding length of 2 kpc. NGC2403 was shown to have an extended (e-folding length = 6 kpc) distribution, somewhat similar to M31. The edges of other objects are essentially defined by the beams used in their observation.

In summary, it appears that a differentiation among Hubble classes is most pronounced in the hydrogen surface density σ_{HI}, which increases by a factor of 2 to 4 along the sequence Sb to Irr, and in the integral quantities, particularly the ratio M_{HI}/M. We inquire as to a variation of properties within a class, requiring a two (or more) dimensional classification scheme. The possible necessity for multi-variate classification has been suggested before: Roberts (1963) proposed that a second parameter should be the total mass; Heidmann (1969) preferred the luminosity. Gouguenheim (1969) favors the use of van den Bergh's (1960) luminosity classes, an ostensibly morphological (and therefore distance-independent) quantity.

We have investigated this latter proposal for galaxies of type Sc-Scd. Using the relatively accurately known bounded masses for M33, NGC2403 and M101, we find a suggested correlation of luminosity class with mass in the sense that the more luminous galaxies are also the more massive. Confirmation of this reasonable correspondence can be found in the data collected by Gouguenheim, although it is not so obviously present in those of Roberts (1969). The latter results are derived using the total mass formula of Brandt (equation 6.6), which we have seen represents a dangerous extrapolation of the measured velocities in the case of flat rotation curves. Gouguenheim employs the less sensitive "indicative" mass dexcribed by Bottinelli _et al_. (1968). Since the luminosity classes have been shown to be good indicators of absolute magnitude, we find that the three originally proposed second parameters are equivalent. There is but one free integral property left, M_{HI}. Its variation may be examined by considering changes in the ratio M_{HI}/M with luminosity class.

To do this in a reasonable way requires use of a consistent "total" mass. As stated above the extrapolated Brandt masses are very unsure; Bottinelli *et al.*'s indicative masses employ Holmberg dimensions, readily available and consistently defined, but not related *a priori* to the hydrogen distributions. In consideration of the data currently available, we suggest use of a radius r_s defined as the point at which σ_{HI} has declined to 2×10^{20} cm^{-2}. The suggestion is defended on the grounds that r_s generally represents the extreme point of good signal-to-noise in present studies, while at the same time being outside of 85 to 95% of the HI distribution. Furthermore, the rapid decline of σ_{HI} in the outer galactic regions allows a sharp determination of r_s, and the fact that the peak values of σ_{HI} are all similar gives r_s the characteristics of a uniform percentage contour. Evidently r_s is not affected by distance uncertainties. With this definition, and employing the HI and rotational parameters given for M33, NGC2403 and M101, we arrive at the values for $M_{HI}(r_s)/M(r_s)$ listed in Table 12. The values of $M(r_s)$ were calculated using the functions of Brandt and Scheer (1965).

We note that r_s agrees well with the Holmberg radii.

TABLE 12

Mass Ratios for Sc Spirals

Object	r_s (arcmin)	$r_s/r_{Holmberg}$	$\langle\sigma_{HI}\rangle$ $r\leq r_s$ (10^{20} cm^{-2})	$M_{HI}(r_s)$ (10^9 $M_\odot$)	$\frac{M_{HI}(r_s)}{M_{HI}(\infty)}$	$\frac{M_{HI}(r_s)}{M(r_s)}$
M33[1]	40'	0.96	6.2	1.5	.94	.090
NGC2403	14	0.96	5.0	2.9	.84	.081
M101[2]	16	1.14	5.9	4.2 1.7	.92	.043 (D=3.44 Mpc[3]) .085 (D=6.9 Mpc[4])

Notes: 1. Data from Gordon (1971). 2. Data from Rogstad (1971). 3. Rogstad's adopted distance. 4. Distance from Tammann (private communication).

It also defines a disk within which ~90% of the total HI mass is found. The important fact is the relatively constant fractional HI content (assuming Tammann's distance to M101 is the more accurate) over a 12 to 1 range in galactic mass. Gouguenheim has claimed a correlation of M_{HI}/M with van den Bergh luminosity class, but an examination of her data for Sc-Scd objects shows no such relation. Roberts (1969) data also show no correlation. We deduce that within the Sc class, $M_{HI} \propto M$.

Assuming a similar geometry for both mass distributions, this result implies the density ratio $\langle\rho_{HI}\rangle/\langle\rho\rangle$ is also constant. For planar HI distributions, $\langle\sigma_{HI}\rangle \propto \langle\rho_{HI}\rangle$, so that the invariance of the former applies to the latter, and therefore also to $\langle\rho\rangle$. To a first approximation, then, the Sc spirals have similar average local densities, and differ from one another only in radius with $r \propto \sqrt{M}$.

One of the hoped-for results of high resolution studies was to firmly establish the spatial coincidence of HI and the optical spiral arms. This goal has been only partially realized, the observed arm-interarm gas contrast being low at best. This situation will obviously improve when greater resolution is available, but it is remarkable (and disconcerting, from the standpoint of defining the spiral arms in our own Galaxy) that spiral structure is generally indiscernable on the HI maps alone. Note that the two-component model of hydrogen distribution, which fills the interarm regions with hydrogen at several times the ∿100°K kinetic temperature measured in the arms will, because of optical depth effects, work to reduce the observed arm-interarm contrast. Recent studies (Burton 1971; Quirk 1971) have tended to support a rather constant HI volumetric density within and between arms in the Galaxy.

3. Velocity Fields

The HI velocities observed in NGC4236 and IC10 have been discussed in Chapter 6, as were the peculiar velocities seen in NGC2403. We consider here the very flat rotation curve derived for the latter object, as this phenomenon appears to be characteristic of several galaxies. It may be questioned on the grounds that most optically derived rotation curves appear to have well-defined turnover points (see references in Burbidge and Burbidge 1971). However, as mentioned before, resolution effects are most severe when the slope of the rotation curve is large, a situation which hardly prevails in the outer regions of this object. One might also cite the case of NGC6574 (Demoulin and Chan 1969), an Sc galaxy for which optical measures indicate a very flat rotation. The limited radial extent of most optical investigations evidently fails to define such rotation curves. Two other nearby galaxies studied in the 21-cm line, M33 and M101 have also been shown to have very flat rotation curves. These two objects are similarly of type Sc. Additionally, we note that a flat rotation curve would hardly be incompatible with the data available for M31 (Gottesman and Davies 1970; Rubin and Ford 1970) and our own Galaxy (Kerr and Westerhout 1965). The existence of extended regions of constant rotational velocity has some important consequences. As mentioned before, estimates of the total mass of the object become hazardous at best, simply because the mass fraction outward of a given radius is falling only slightly with increasing distance from the center. Furthermore, because of the accompanying relatively slow decrease in the mass surface density σ, a very large increase in the mass-to-light ratio can occur.

A mass model built up of oblate spheroids as given by Burbidge, Burbidge and Prendergast (1959) and extended by Schmidt (1965) shows that for rotation curves expressible as a power series in r

$$\frac{V_{rot}^2}{r^2} = \sum_n \nu_n r^n, \tag{7.1}$$

the resulting mass density has the dependence

$$\rho(a) = \sum_n \rho_n a^n. \tag{7.2}$$

Here a describes a spheroidal surface

$$a^2 = r^2 + \frac{z^2}{c^2} ,$$

where z is the distance perpendicular to the plane of the galaxy and c is the axial ratio. The constants ρ_n are related to the ν_n in a simple way given by Schmidt. Clearly, for a rotation curve dominated by a large region of constant velocity, the mass density will fall as a^{-2}. The surface density is found by integrating over z, which for the spheroidal model means an integration through volumes whose densities are determined by the rotation curve beyond the radius at which σ is being sought. In other words, while ρ is well determined within the confines of the rotation curve, σ is dependent on the extrapolated behavior of V_{rot}. This important point was noted by Schmidt. If V_{rot} stays constant out to a radius r', thereafter dropping to zero, the surface density will have the behavior

$$\sigma(r) = 2\rho_{-2} c \frac{1}{r} \tan^{-1} \left[\frac{r'^2}{r^2} - 1\right]^{\frac{1}{2}} .$$

This function drops off as approximately r^{-2} in the region $0.5 < r/r' < 0.8$, and we note that the rate of decrease is independent of the axial ratio. In order that M/L[*] remain

---

[*] In deference to custom, we designate the surface mass-to-luminosity ratio by M/L. Consistency with the notation of the text would require this quantity to be written σ/L.

reasonably constant, the luminosity in the regions of constant V_{rot} should have a similar radial dependence. Such observations as are available show this to be hardly the case. De Vaucouleurs (1958, 1959) has published photometry on the nearby objects M31 and M33, whose large angular scales allow measurements to relatively great radii. The surface luminosities can be fit quite well (except in the very central regions) by an exponential function. Scale (e-folding) lengths for M31 and M33 are respectively 3.9 and 1.5 kpc in the blue, or ∿0.1 times their Holmberg diameters. Clearly, an exponentially decreasing luminosity of such short scale length will soon overwhelm a mass density falling no faster than r^{-2}, and M/L will increase dramatically in the outer regions of the galaxy.

Such an increase has already been noted for the two photometered objects mentioned above. For M31, Gottesman and Davies find that M/L has risen to 20 at 22 kpc (the largest radius measured by de Vaucouleurs). Boulesteix and Monnet (1970) have made a similar discovery for M33, using the rotation curve data of Gordon and Carranza _et_ _al_. (1968). M/L rises from ∿2.5 near the center to ∿20 at 8 kpc, with slight variations depending on the choice of axial ratio. Since M33 is similar to NGC2403, we consider further the validity of this result and the implications for the latter object. In particular, given the very flat rotation curves of these galaxies, is there any escape from a M/L ratio which grows so severely, and if not, what galactic constituents could account for the growth?

Boulesteix and Monnet employed the Burbidge *et al.* mass model described above, and a rotation curve which was essentially flat from 5 kpc to 8.4 kpc. The latter radius represents the limit of the 21-cm measures, and the authors assumed therefore that the mass density was zero outside of 10 kpc. As noted, their computed value of M/L at 8 kpc was ∿20. However, this value must be regarded as an underestimate. This is because they have assumed $\rho=0$ at $r=10$ kpc; any other distribution beyond the measured data will only increase M/L. Indeed, models were investigated with ρ decreasing as r^{-2} and r^{-4} from 10 to 20 kpc, and these caused M/L at 10 kpc to more than double from the value given by Boulesteix and Monnet, while values near the center were hardly altered. Escape from a high M/L in the external reaches of M33 seems impossible.

Approaching the problem from the other end, Freeman (1970) has considered what rotation curve would correspond to an exponential surface density, arguing that the resulting constant M/L is required by existing multi-color photometry. He derives an expression for $V_{rot}(r)$ which falls almost linearly beyond the turnover point (see Figure 2 of the reference), and with a slope that is quite incompatible with the data for M101, M33, and NGC2403. A galactic model of zero thickness was assumed.

Unfortunately, no published photometry for NGC2403 is available. However, it is easy to demonstrate the probable similarity of its situation to that of M33. An estimate of the luminosity can be made by scaling the M33 data to account for differences in Holmberg diameters and absolute luminosities. We adopt a law of the form

$$L = 200\ e^{-.4\ r} \quad (L_{\odot}\text{-pc}^{-2}),$$

with r in kpc. The central luminosity is essentially the same as for M33, an assumption supported by Freeman's collected data. Use of this relation, together with a mass surface density derived according to the precepts of Brandt and Scheer (1965) leads to the M/L relation shown in Figure 39. The rotation curve constants were those determined in Chapter 6. Also shown are the radial dependencies of several other mass and light ratios.

As expected, the mass-luminosity curve grows in a manner similar to M33. Evidently the slope of this curve is rather sensitive to the luminosity scale length, and therefore the numbers should not be taken too literally. However, unless the behavior of M33 is exceptional, the growth of M/L with radius in NGC2403 is predictable.

An explanation for this growth requires the presence of

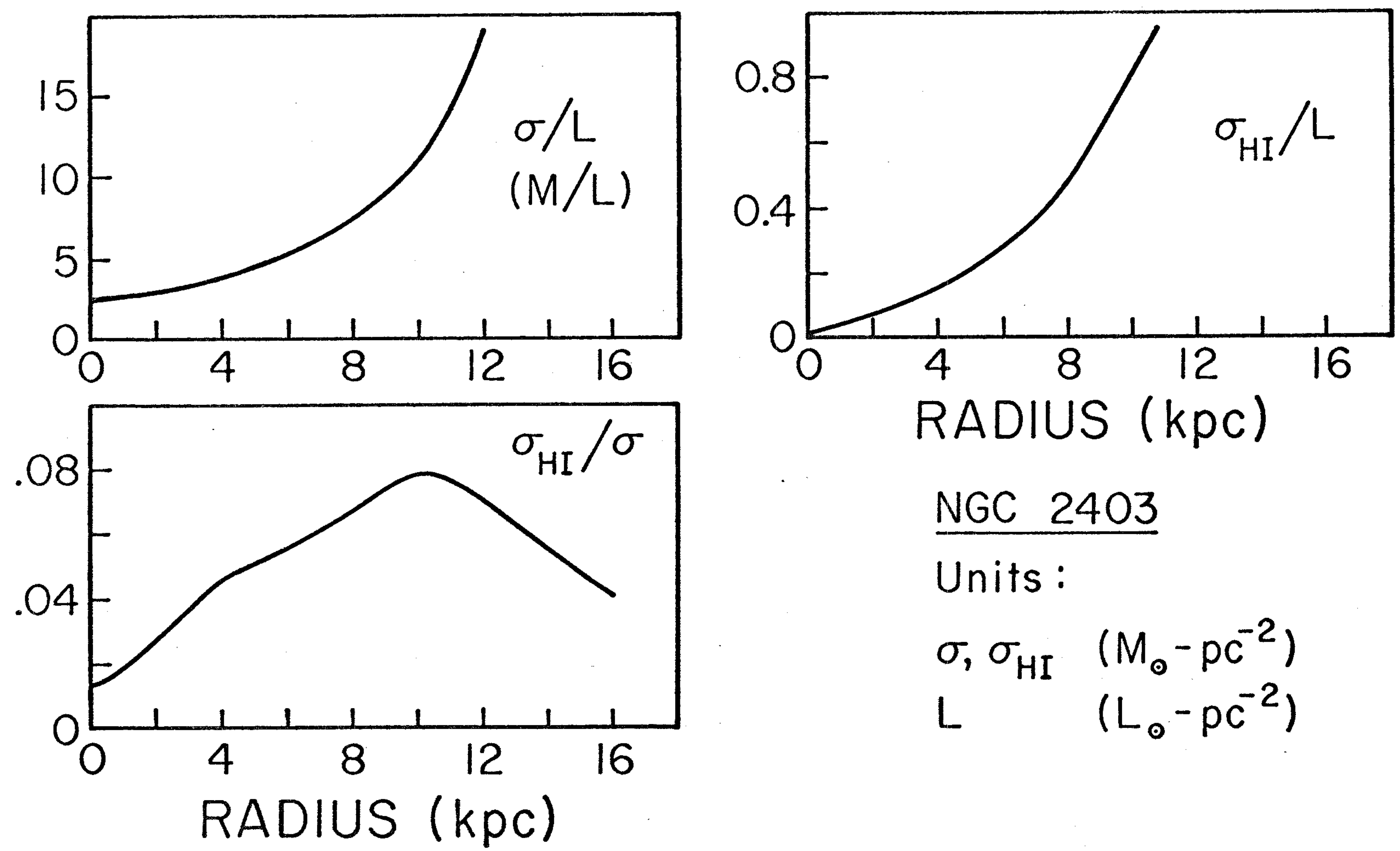

Figure 39. Surface mass and luminosity density ratios for NGC2403. The luminosity is hypothesized to be exponential with radius.

underluminous material in the outer regions of the galaxy. The present study has confirmed the very small mass contribution of HI, and molecular hydrogen is expected to be even less abundant. A frequently mentioned constituent of high M/L regions is dwarf stars (see for example Spinrad 1966). This explanation requires the stellar luminosity function to be very steep at the faint end. Verification of this suggestion requires sensitive photometry of the outer reaches of the object, the currently available work being somewhat inconclusive. De Vaucouleurs' M33 U and V photometry extends to only 2 kpc along the major axis and twice this amount along the minor axis. He states that the object appears redder near the center and bluer in the outlying regions, but this simply reflects the presence of the Population I spiral arms. The region of highest M/L, at 8 kpc, is substantially beyond the visible arm regions.

What is required is a reversion to a predominantly older population at these larger radii. In the non-linear density-wave theory, the effective gas compression at the spiral shocks decreases at large radius (Roberts and Yuan 1970). If we assume high gas densities are required for the formation of Population I material, this decrease would explain the lack of very luminous matter in these outer regions. The correlation, mentioned previously, between the number of HII regions in a galaxy and its total HI content is not violated with this assumption since the hydrogen surface density is falling rapidly at the radii in question and is concomitant with a thickening of the HI layer. A resulting implication is that the dwarf stellar material ($M \sim 0.2\ M_{\odot}$) can be formed in regions of low overall gas density. Clarification of this problem is dependent on photometry of the outermost regions of the affected galaxies. If an extensive dwarf population proves inadmissible, more esoteric solutions, such as the presence of "black holes" (Truran and Cameron 1970), must be considered.

Of the other quantities shown in Figure 39, perhaps the most interesting is the surface density ratio σ_{HI}/σ. This shows a fractional HI minimum near the center (which would be even more pronounced for an object like M101) and in the very outer regions. The former is a consequence of the strong central mass concentration; the latter is attributable to the flat rotation curve.

4. Summary

In the course of this work we have discussed in detail the HI distributions and velocity fields for three objects. For the case of NGC2403, we have considered how this object may be related to other Sc-Scd galaxies studied with comparably high resolution. It would seem useful and appropriate to briefly list the more important results of the present study.

A. HI Distributions

1. Overall confinement of the HI to the optical dimensions given by Holmberg (1958), and to the disks of the objects.
2. Good positional agreement of HI concentrations and HII regions.
3. Existence of unresolved HI peaks for all objects, indicating a "lumpy" distribution in the regions of intense optical emission.

B. Velocity Field

1. For NGC2403, a rapidly-rising rotation curve followed by an extended region of constant circular velocity. A slight (≤ 15 km-s^{-1}) discrepancy, probably not real, exists between observed HI and HII velocities.
2. For NGC4236, an extensive region of solid-body rotation coincident with the bar is seen. The bar has a low mass density. The rate of decrease of the curve beyond the turnover point is inconsistent with theoretical models. IC10 shows a radial velocity field consistent with rotation.
3. Peculiar motions in NGC2403 are in the direction and location predicted by the density-wave theory of spiral structure. We utilize non-linear effects

to account for the large observed amplitudes.

4. The flat rotation curve of NGC2403, seen in other late-type spirals, implies a mass density dropping as slowly as r^{-2}. Uncertain total masses result, and for this reason it is felt that only bounded masses (limited by the last point on the measured rotation curve) should be quoted. The flat curve also requires high mass to light ratios in the outer galactic regions, as well as a decreasing fractional HI content.

C. Integral Properties

1. A two-dimensional classification scheme is favored: along the Hubble sequence from Sb - Sc - Sd - Irr we confirm an increase in M_{HI}/M (using bounded masses), and σ_{HI}. Within the Sc-Scd class, we find a mass sequence correlated with van den Bergh luminosity class (and therefore luminosity) for which M_{HI}/M is constant and approximately equal to 9%. The bounded masses are confined to the radius at which σ_{HI} has dropped to 2×10^{20} cm^{-2} (r_s), very nearly the Holmberg radius.
2. The luminosity for IC10 seems anomalously high, suggesting that Galactic absorption has been overestimated.

5. Suggestions for Future Work

It is obvious that HI studies with improved spatial and velocity resolution will be required to further elucidate such problems as the two-component gas model, the arm-interarm HI contrast, and the density-wave theory of spiral structure. There exist, however, several avenues of investigation not requiring the extensive observing and reduction times associated with the high resolution studies. A very sensitive, moderately broad-beam study of the outer regions of one of the Sc objects could fix the very uncertain behavior of the mass distributions there. Additionally, galactic evolution is best studied by considering integral properties of large numbers of galaxies. Very low resolution studies, which yield M_{HI} and V_{max}, may be used to determine these properties if the close correlation of r_s and Holmberg radius established here can be extended to other objects. In particular, very few galaxies of early type have been observed.

Galactic surveys, of the type just described, are heavily dependent on good distance determinations. Furthermore, apparent magnitudes are required for determining luminosity ratios. Much of the scatter in the survey data (e.g. Gouguenheim 1969) is no doubt due to errors in these optically-derived parameters. Additional useful optical investigations would include sensitive multicolor photometry of the outer regions of galaxies and Hα studies of those areas in which continuum sources are seen or HI appears to be missing (e.g. central regions of spirals and the "hole" in IC10). Radio continuum measurements at several frequencies could also be used to establish whether such emission is thermal.

APPENDIX

Derivation of Interferometer Response

In this section the general response of a multiplying correlation interferometer is derived. In Figure A1 is shown a block diagram of the essential elements of a single-conversion superhetrodyne interferometer such as was used for the work covered by this thesis. The second diagram, a simplification of the first, reduces all elements to filtering, multiplying or delaying operations. Since receiver gains simply enter as multiplicative constants, we will, for convenience, assume them to be one. This includes such things as cable attenuations, unequal antenna areas, etc. Furthermore, all phase shifts and time delays, both geometric and instrumental, are combined into the two delays τ_1 and τ_2. These "delays" represent the delay differences between the two branches of the instrument and can be either positive or negative. Note that τ_1 occurs before the mixing operation.

We denote the voltages at the antenna terminals by y. Before the signals reach the mixer, the voltages in the two branches are

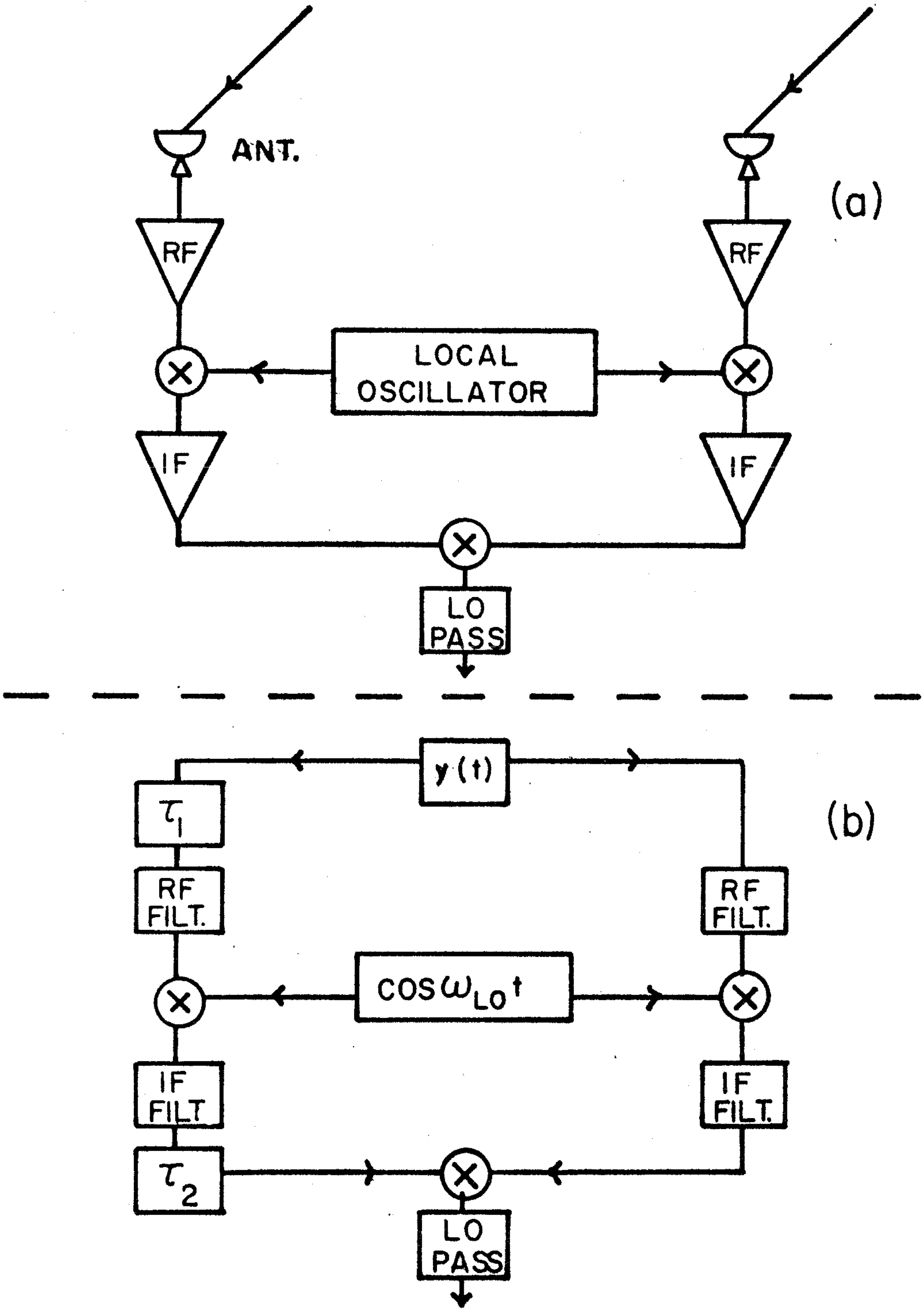

Figure A1. (a) Basic elements of multiplying interferometer. (b) Elements reduced to delays, filters and multipliers.

$$y'(t + \tau_1) = y(t + \tau_1)*g(t + \tau_1)$$

and $$y'(t) = y(t)*g(t), \qquad (A.1)$$

where $g(t)$ is the Fourier transform of the RF bandpass[1]. In this derivation, we have assumed plane-parallel wavefronts; i.e. the radiation is from a point source. Generalization to an extended object is made in Chapter 1. Note that since we require voltages

---

[1] Throughout this Appendix, as well as elsewhere in this thesis, the symbol $*$ denotes convolution. Fourier transforms are indicated by F.T. Transform pairs have capital letters substituted for lower-case and vice versa.

The convolution in expression (A.1) arises from the fact that, gain considerations aside, the RF amplifier acts as a frequency filter. In the frequency domain

$$Y'(\omega) = Y(\omega)G(\omega),$$

where $G(\omega)$ is the voltage frequency bandpass of the RF section. We define the transform relations as

$$Y(\omega) = \int_{-\infty}^{\infty} y(t)e^{i\omega t}\, dt$$

and $$y(t) = \int_{-\infty}^{\infty} Y(\omega)e^{-i\omega t}\, d\omega$$

Then by the convolution theorem

$$y'(t) = y(t)*g(t).$$

to be real, $g(t)$ is real and $G(\omega)$ is hermitian; i.e. $G(-\omega)=G^{*}(\omega)$. These remarks similarly apply to the IF section.

After mixing by the local oscillator, we have

$$y'(t + \tau_1)\cos\omega_{LO}t$$

and

$$y'(t)\cos\omega_{LO}t. \tag{A.2}$$

The IF amplifiers and associated delaying cables introduce a further bandpass function $F(\omega)$ and additional delay τ_2. At the inputs to the multiplier, the signals are

$$y'(t + \tau)\cos\omega_{LO}(t + \tau_2) \ast f(t + \tau)$$

and

$$y'(t)\cos\omega_{LO}t \ast f(t), \tag{A.3}$$

where we have defined $\tau = \tau_1 + \tau_2$. Rearranging slightly, the voltages of (A.3) become

$$\cos\omega_{LO}\tau_1 y'(t + \tau)\cos\omega_{LO}(t + \tau) \ast f(t + \tau)$$

$$+ \sin\omega_{LO}\tau_1 y'(t + \tau)\sin\omega_{LO}(t + \tau) \ast f(t + \tau)$$

and

$$y'(t)\cos\omega_{LO}y \ast f(t). \tag{A.4}$$

While seemingly complicating the formalism, these rearrangements have allowed the signals to be written either as functions of t or $t + \tau$. Therefore multiplication and integration of these two voltages is an operation of the form

$$\int_{T_1}^{T_2} v(t)x(t + \tau)dt.$$

As the integration time $T_2 - T_1$ increases, this integral approaches the (unnormalized) covariance of v and x. The actual integration time is ~12 seconds. Even with 100 kHz narrow-band filters, the typical correlation time is $\sim 10^{-6}$ seconds. Therefore it is entirely reasonable to take the interferometer output $R(\tau_1,\tau_2)$ as proportional to the convolution[2] formed by multiplying the signals of (A.4)

---

[2] We use the terms covariance and convolution interchangeably. They are defined somewhat differently, however. Strictly speaking, the convolution of h and g is

$$R(\tau) = \int_{-\infty}^{\infty} h(t)g(\tau - t)dt.$$

The usual convolution theorem then yields

$$R(\tau) = \text{F.T.} \left[H(\omega)G(\omega) \right] .$$

For the present analysis, we require the analagous relation for the covariance

$$R(\tau) = \int_{-\infty}^{\infty} h(t)g(t + \tau)dt,$$

for which it is easily shown

and integrating over infinite time. With the definitions

$$a(t) = y'(t)\cos\omega_{LO}t * f(t)$$

$$b(t) = y'(t)\sin\omega_{LO}t * f(t), \tag{A.5}$$

we have

$$R(\tau_1,\tau_2) \propto \cos\omega_{LO}\tau_1 (a*a) + \sin\omega_{LO}\tau_1 (b*a). \tag{A.6}$$

Clearly the first term is proportional to the autocorrelation function of a(t) which, by the convolution theorem, is simply the Fourier transform of the power spectrum of a(t). Calculation of the power spectrum is elementary; reference to Figure A2 will illustrate the procedure.

We begin with the spectrum $P(\omega)$ of the voltage entering the antenna, $y(t)$. Because $y(t)$ is real, $\text{F.T.}\left[y(t)\right]$ is hermitian. Thus $P(\omega)$ is real, positive and even (a). The RF bandpass function multiplies $P(\omega)$ producing a new spectrum $P'(\omega) = P(\omega)\left|G(\omega)\right|^2$ (b). Heterodyning by the mixer shifts both sides of $P'(\omega)$ toward the origin by the amount

---

$$R(\tau) = \text{F.T.}\left[H^*(\omega)G(\omega)\right]$$

where h and g are real and superscript * denotes complex conjugate. Note that for h=g, the covariance becomes the autocorrelation function, and the above expression is simply the Wiener-Khinchine theorem.

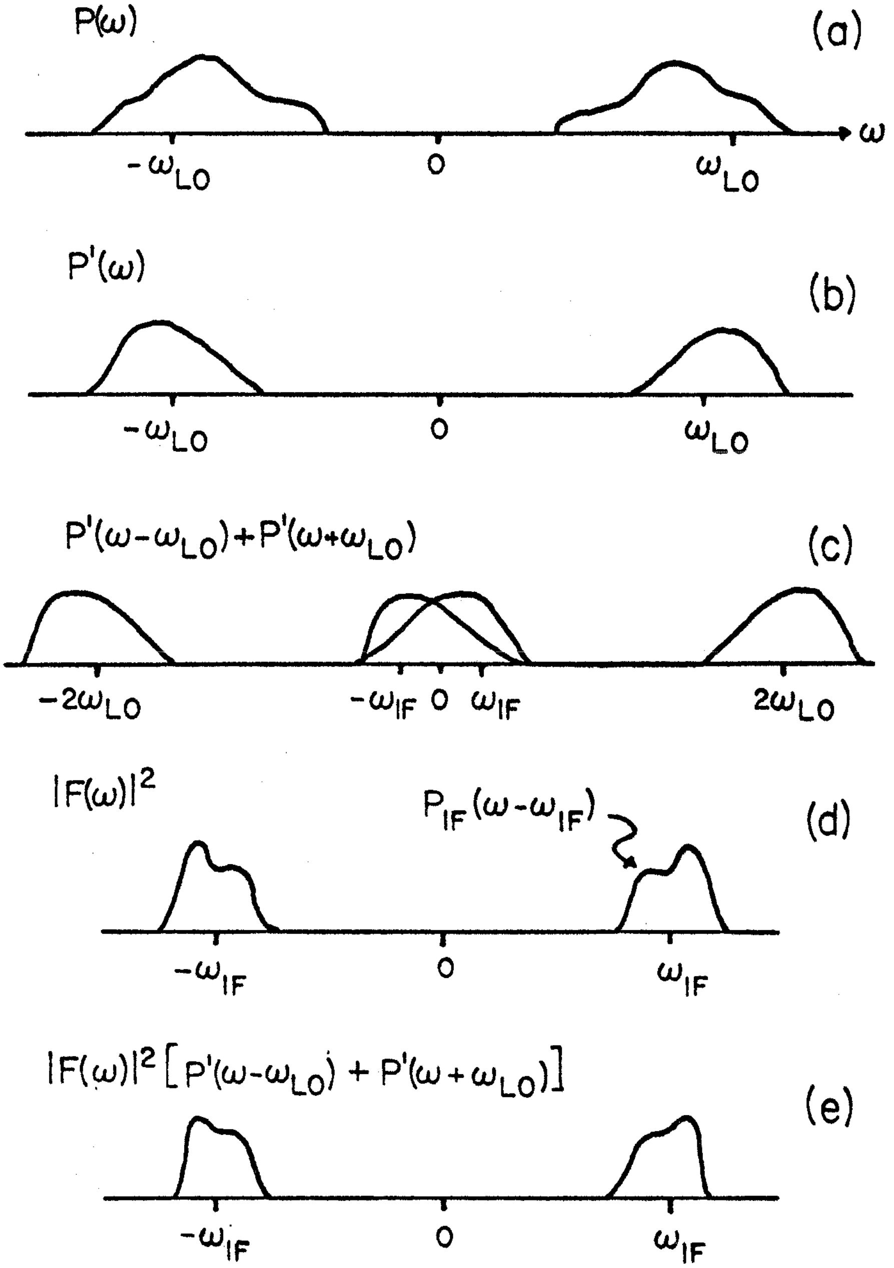

Figure A2. Schematic representation of various power spectra in a superhetrodyne receiver. (a) Entering power spectrum. (b) Spectrum after filtering by RF amplifier. (c) After mixing at frequency ω_{LO}. (d) IF amplifier power response. (e) Spectrum after filtering through IF section.

ω_{LO} (c). Note that the responses at $\pm 2\omega_{LO}$ are outside the response of the following IF section. Finally the IF filter bandlimits the spectrum at $\pm\omega_{IF}$ with multiplication by $|F(\omega)|^2$ (d) producing the power spectrum S_1 (e). The autocorrelation function of a(t) is the transform of this spectrum. For clarity, we define the signal and image frequencies as

$$\omega_s = \omega_{LO} + \omega_{IF}$$

$$\omega_i = \omega_{LO} - \omega_{IF} \; . \qquad (A.7)$$

The spectrum can then be rewritten as

$$S_1 = \frac{P_{IF}(\omega)}{4} \left[P'(\omega_i - \omega) + P'(\omega_s + \omega) \right] * \delta(\omega - \omega_{IF})$$

$$+ \frac{P_{IF}(-\omega)}{4} \left[P'(\omega_i + \omega) + P'(\omega_s - \omega) \right] * \delta(\omega + \omega_{IF}) , \qquad (A.8)$$

where we have introduced $P_{IF}(\omega)$ as the positive frequency IF bandpass centered about $\omega=0$ instead of $\omega=\omega_{IF}$. Remember that (A.8) simply represents the spectrum shown in (e); it is an even function. Defining

$$W(\omega) = P_{IF}(\omega) \left[P'(\omega_i - \omega) + P'(\omega_s + \omega) \right] , \qquad (A.9)$$

(A.8) takes on the simpler form

$$S_1 = \frac{W(\omega)}{4} * \delta(\omega-\omega_{IF}) + \frac{W(-\omega)}{4} * \delta(\omega+\omega_{IF}). \qquad (A.10)$$

Taking the Fourier transform of S_1 is more enlightening if we break up $W(\omega)$ into the sum of an even (W_e) and an odd (W_o) function. It is easily shown that

$$\begin{aligned} F.T.\{S_1\} &= a*a \\ &= \tfrac{1}{2}\{(F.T.W_e)^2-(F.T.W_o)^2\}^{\frac{1}{2}}\cos(\omega_{IF}\tau-\phi(\tau)), \end{aligned} \qquad (A.11)$$

where

$$\tan\phi(\tau) = i\,\frac{F.T.W_o}{F.T.W_e}. \qquad (A.12)$$

Note that all transforms are functions of $\tau=\tau_1+\tau_2$. The importance of $\phi(\tau)$ depends on the asymmetry of the power spectrum after passing through the IF strip. Clearly, choice of ω_{IF} to be the centroid of the spectrum will minimize the value of W_o and therefore ϕ. For the usual illustrative case of symmetric bandpasses, $\phi=0$.

The second term of the response equation (A.6) can be evaluated using the convolution theorem. Using a procedure similar to the above, one finds

$$\begin{aligned} F.T.(b*a) = S_2 = &\frac{P_{IF}(\omega)}{4i}\Big[P'(\omega_s+\omega)-P'(\omega_i-\omega)\Big]*\delta(\omega-\omega_{IF}) \\ &\frac{-P_{IF}(\omega)}{4i}\Big[P'(\omega_s-\omega)-P'(\omega_i+\omega)\Big]*\delta(\omega+\omega_{IF}). \end{aligned} \qquad (A.13)$$

Defining

$$Z(\omega) = P_{IF}(\omega)\{P'(\omega_s+\omega)-P'(\omega_i-\omega)\}, \tag{A.14}$$

we find

$$F.T.\{S_2\} = \tfrac{1}{2}\{(F.T.Z_e)^2-(F.T.Z_o)^2\}^{\frac{1}{2}}\sin(\omega_{IF}\tau-\theta(\tau)), \tag{A.15}$$

where as before

$$\tan\theta(\tau) = i\,\frac{F.T.Z_o}{F.T.Z_e}\ . \tag{A.16}$$

We insert the expressions for the convolutions into (A.6) to get the general interferometer response

$$\begin{aligned}R(\tau_1,\tau_2) &= \frac{G}{2}\{(F.T.W_e)^2-(F.T.W_o)^2\}^{\frac{1}{2}}\cos\omega_{LO}\tau_1\cos(\omega_{IF}\tau-\phi(\tau))\\ &+\frac{G}{2}\{(F.T.Z_e)^2-(F.T.Z_o)^2\}^{\frac{1}{2}}\sin\omega_{LO}\tau_1\sin(\omega_{IF}\tau-\theta(\tau)),\end{aligned} \tag{A.17}$$

The proportionality constant G represents the system gain. This constant is easily determined in practice by observation of sources of known intensity.

As a practical matter, the bandpass functions are very nearly symmetric. With this assumption, the response becomes

$$\begin{aligned}R(\tau_1,\tau_2) &= \frac{G}{2}\,F.T.\{P_{IF}(P'_{\omega_s}+P'_{\omega_i})\}\cos\omega_{LO}\tau_1\cos\omega_{IF}\tau\\ &+\frac{G}{2}\,F.T.\{P_{IF}(P'_{\omega_s}-P'_{\omega_i})\}\sin\omega_{LO}\tau_1\sin\omega_{IF}\tau,\end{aligned} \tag{A.18}$$

where P'_{ω_s} and P'_{ω_i} are the RF power spectra at the signal and image frequencies. There are two special cases for which the above expression simplifies further. In the first of these, double-sideband operation, it is assumed that the source power spectrum is the same at both the signal and image frequencies. Then $P'_{\omega_s} = P'_{\omega_i}$ and

$$R(\tau_1,\tau_2) = G\ \text{F.T.}\{P_{IF}P'_{\omega_s}\}\cos\omega_{LO}\tau_1\cos\omega_{IF}\tau. \qquad (A.19)$$

Note the separation of the terms at the two frequencies ω_{LO} and ω_{IF}. Pictorially the response is the familiar "sausage" pattern shown in Figure A3. Recall that τ_1 comprises delays occurring before mixing, including the time-dependent geometric delay. It is standard practice in double-sideband work to continually adjust τ_2 so that $(\tau_1+\tau_2)=0$. When this condition obtains, the interferometer is responding to the total power of the source, and the time-dependent fringes $(\cos\omega_{LO}\tau_1)$ have their maximum amplitude. The phase of these fringes is evidently unaffected by the variation of τ_2, and this is one of the principal advantages of double-sideband operation. It might be remarked that it is the fact that the mixing operation is correlated with time in the two branches of the interferometer that accounts for the different effects of delays before and after the mixer (τ_1 and τ_2 respectively). Finally, to the extent that P'_{ω_s} is flat, the "sausage" pattern envelope is simply the Fourier transform of the IF bandpass.

The second special case involves supression of the power in either the signal or image sideband (single-sideband operation). This circumstance obtains naturally in spectral line work, such as discussed in this thesis. It is common, however, to ensure response to only one of the sidebands by using an RF pre-filter to guarantee attenuation of the other, and to suppress response to continuum sources. If we choose to pass only the "signal" sideband, then $P'_{\omega_i}=0$, and (A.18) becomes

$$R(\tau_1,\tau_2) = \frac{G}{2}\,\mathrm{F.T.}\{P_{IF}P'_{\omega_s}\}\cos(\omega_{LO}\tau_1-\omega_{IF}\tau). \qquad (A.20)$$

If τ_1 alone were to vary with time, we would expect fringes at a frequency proportional to $(\omega_{LO}+\omega_{IF})$. Their amplitude would gradually be diminished because of modulation by the bandpass envelope $\mathrm{F.T.}\{P_{IF}P'_{\omega_s}\}$, a function of $(\tau_1+\tau_2)$. As in double-sideband work, we adjust τ_2 so that $(\tau_1+\tau_2)=0$ and therefore keep the envelope at its maximum, or total power point. However, changing τ_2 alters the phase of the fringes by $\omega_{IF}\Delta\tau_2$ radians and it is thus mandatory to record the values of τ_2 in order to recover the original, or source, phase. The single-sideband response is also shown in Figure A.3.

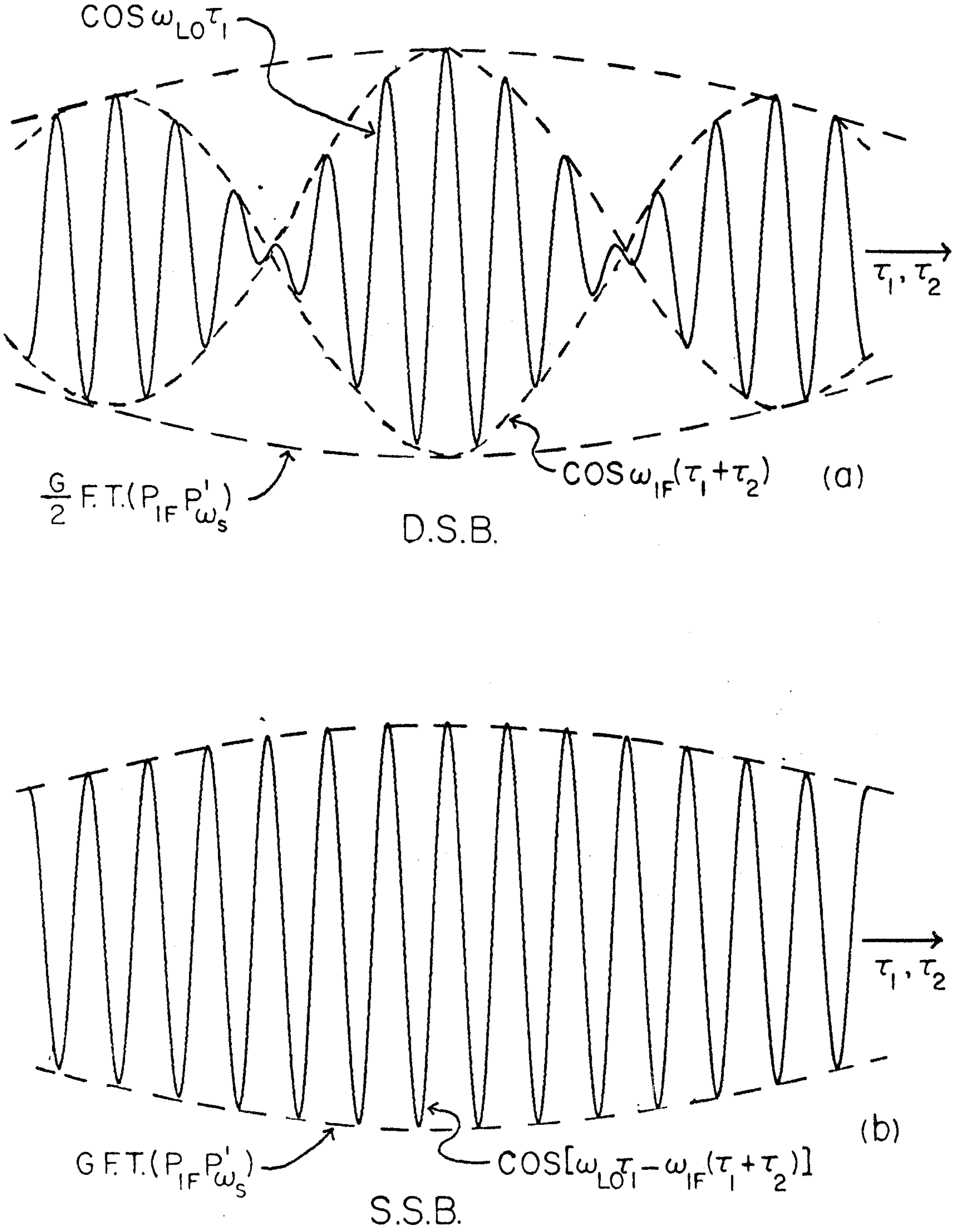

Figure A3. Double (a) and single (b) sideband point source responses assuming symmetric passbands.

REFERENCES

Arp, H. C. 1964, *The Galaxy and the Magellanic Clouds*, IAU Symposium No. 20 (Canberra: Australian Academy of Science), p. 219.

Baade, W. 1931, *A.N.*, **243**, 303.

Baldwin, J. E., Warner, P. J., and Wright, M. C. H. 1971, *M.N.R.A.S.* (in press).

Beale, J. S., and Davies, R. D. 1969, *Nature*, **221**, 531.

Bergh, S. van den. 1959, *Pub. David Dunlap Obs.*, **II**, No. 5, 147.

_______. 1960, *Ap.J.*, **131**, 215.

Biraud, Y. 1968, *Astr. and Ap.*, **1**, 124.

Bottinelli, L., Gouguenheim, L., Heidmann, J., and Heidmann, N. 1968, *Ann. d'Ap.*, **31**, 205.

Boulesteix, J., and Monnet, G. 1970, *Astr. and Ap.*, **9**, 350.

Brandt, J. C. 1960, *Ap.J.*, **131**, 293.

Brandt, J. C., and Scheer, L. S. 1965, *A.J.*, **70**, 471.

Bridle, A. H., and Kesteven, M. J. L. 1970, *A.J.*, **75**, 902.

Brundage, W. D., and Kraus, J. D. 1966, *Science*, **153**, 411.

Burbidge, E. M., and Burbidge, G. R. 1971, in *Stars and Stellar Systems*, Vol. **9**, ed. A. and M. Sandage (Chicago: University of Chicago Press), in preparation.

Burbidge, E. M., Burbidge, G. R., and Prendergast, K. H. 1959, *Ap.J.*, **130**, 739.

_______. 1960, *Ap.J.*, **132**, 654.

_______. 1962a, *Ap.J.*, **136**, 119.

_______. 1962b, *Ap.J.*, **136**, 704.

Burke, B. F., Turner, K. C., and Tuve, M. A. 1964, *Annual Report of the Director, 1962-1963, Dept. of Terrestrial Magnetism* (Washington, D.C.: Carnegie

Institution of Washington), p. 341.

Burns, W. R., and Roberts, M. S. 1971, *Ap.J.*, **166**, 265.

Burton, W. B. 1971, *Astr. and Ap.*, **10**, 76.

Carranza, G., Courtes, G., Georgelin, Y., Monnet, G., and Pourcelot, A. 1968, *Ann. d'Ap.*, **31**, 63.

Clark, B. G. 1965, *Ap.J.*, **142**, 1398.

Cooper, B. F. C., Epstein, E. E., Goldstein, S. J., Jelley, J. V., and Kaftan-Kassim, M. A. 1960, *A.J.*, **65**, 486.

Courtes, G. 1960, *Ann. d'Ap.*, **23**, 115.

Danver, C. G. 1942, *Ann. Obs. Lund.*, No. 10, p. 1.

Davenport, W. B., Jr., and Root, W. L. 1958, *Random Signals and Noise* (New York: McGraw-Hill).

Davies, R. D., and Gottesman, S. T. 1970, *M.N.R.A.S.*, **149**, 237.

De Jong, M. L. 1966, *Ap.J.*, **144**, 555.

Deharveng, J. M., and Pellet, A. 1970, *Astr. and Ap.*, **7**, 210.

Demoulin, M.-H., and Chan, Y. W. T. 1969, *Ap.J.*, **156**, 501.

Dixon, R. S., and Kraus, J. D. 1968, *A.J.*, **73**, 381.

Epstein, E. E. 1964a, *A.J.*, **69**, 490.

________. 1964b, *A.J.*, **69**, 521.

Field, G. B. 1958, *Proc. Inst. Radio Eng.*, **46**, 240.

Fomalont, E. B. 1967, *Pub. Owens Valley Rad. Obs.*, **1**, No. 3.

Fomalont, E. B., and Moffet, A. T. 1971, *A.J.*, **76**, 5.

Fomalont, E. B., Wyndham, J. D., and Bartlett, J. F. 1967, *A.J.*, **72**, 445.

Freeman, K. C. 1965, *M.N.R.A.S.*, **130**, 183.

________. 1970, *Ap.J.*, **160**, 811.

Gordon, K. J. 1971, *Ap.J.*, **169**, 235.

Gottesman, S. T., and Davies, R. D. 1970, *M.N.R.A.S.*, **149**, 263.

Gottesman, S. T., Davies, R. D., and Reddish, V. C. 1966, *M.N.R.A.S.*, **133**, 359.

Gouguenheim, L. 1969, *Astr. and Ap.*, **3**, 281.

Greenstein, J. L., and Minkowski, R. 1953, *Ap.J.*, **118**, 1.

Guelin, M., and Weliachew, L. 1969, *Astr. and Ap.*, **1**, 10.

Heeschen, D. S., and Wade, C. M. 1964, *A.J.*, **69**, 277.

Heidmann, J. 1961, *B.A.N.*, **15**, 314.

Heidmann, N. 1969, *Astrophys. Lett.*, **3**, 153.

Hindman, J. V. 1967, *Austr. J. Phys.*, **20**, 147.

Hodge, P. W. 1967, *A.J.*, **72**, 129.

________. 1969, *Ap.J.*, **155**, 417.

Hogbom, J. 1969, Rep. U.R.S.I. 16th Gen. Assembly, Ottawa, Aug.

Holmberg, E. 1958, *Medd. Lund Astr. Obs.*, Ser. II, No. 136.

Hubble, E. 1926, *Mt. Wilson Contrib.*, 324.

________. 1934, *Ap.J.*, **79**, 8.

________. 1936, *The Realm of the Nebulae* (New Haven: Yale University Press), p. 147.

Hughes, M. P. 1969, private communication.

Hughes, M. P., Thompson, A. R., and Colvin, R. S. 1971, *Ap. J. Supp.*, **23** (No. 200).

Hughes, V. A., and Routledge, D. 1970, *A.J.*, **75**, 1148.

Hulst, H. C. van de. 1945, *Ned. T. Natuurk.*, **11**, 201.

Humason, M. L., Mayall, N. U., and Sandage, A. R. 1956, *A.J.*, **61**, 97.

Johnson, H. M. 1959, *Pub. A.S.P.*, **71**, 425.

Kellermann, K. I., Pauliny-Toth, I. I. K., and Williams, P. J. S. 1969, *Ap.J.*, **157**, 1.

Kerr, F. J. 1962, *M.N.R.A.S.*, **123**, 327.

Kerr, F. J., and Westerhout, G. 1965, in *Stars and Stellar Systems*, Vol. **5**, ed. A. Blaauw and M. Schmidt (Chicago: University of Chicago Press), p. 167.

Landau, H. J., and Pollak, H. O. 1961, *Bell Sys. Tech. Journal*, **40**, 65.

Lewis, B. M. 1968, *Proc. A.S.A.*, **1**, 104.

Lin, C. C. 1970, *The Spiral Structure of Our Galaxy*, IAU Symposium No. 38 (New York: Springer-Verlag), p.377.

Lin, C. C., Yuan, C., and Shu, F. H. 1969, *Ap.J.*, **155**, 721.

Mathewson, D. S., and Healey, J. R. 1964, *The Galaxy and the Magellanic Clouds*, IAU Symposium No. 20 (Canberra: Australian Academy of Science), p. 245.

Mayall, N. U. 1935, *Pub. A.S.P.*, **47**, 317.

———. 1941, *Pub. A.S.P.*, **53**, 122.

McGee, R. X., and Milton, J. A. 1966, *Austr. J. Phys.*, **19**, 343.

Moffet, A. T. 1962, *Ap.J. Supp.*, **7**, 93 (No. 67).

Monnet, G. 1971, *Astr. and Ap.*, **12**, 379.

Muller, C. A., and Westerhout, G. 1957, *B.A.N.*, **13**, 151.

Munch, G. 1960, *Ap.J.*, **131**, 250.

Oort, J. H. 1964, *The Galaxy and the Magellanic Clouds*, IAU Symposium No. 20 (Canberra: Australian Academy of Science), p. 1.

———. 1965a, *Trans. IAU XII A* (New York: Academic Press), p. 789.

———. 1965b, in *Stars and Stellar Systems*, Vol. **5**, ed. A. Blaauw and M. Schmidt (Chicago: University of Chicago Press), p. 455.

———. 1968, in *Galaxies and the Universe*, ed. L. Woltjer (New York: Columbia University Press), p. 1.

Page, T. 1962, *Ap.J.*, **136**, 685.

Perek, L. 1962, *Adv. Astron. Astrophys.*, **1**, 165.

Pike, E. M., and Drake, F. D. 1964, *Ap.J.*, **139**, 545.

Pikel'ner, S. B. 1968, *Ann. Rev. Astr. Ap.*, **6**, 165.

Pooley, G. G. 1969, *M.N.R.A.S.*, **144**, 101.

Purcell, E. M., and Field, G. B. 1956, *Ap.J.*, **124**, 542.

Quirk, W. J. 1971, *Ap.J.*, (in press).

Read, R. B. 1963, *Ap.J.*, **138**, 1.

Riegel, K. W. 1966, Ph. D. Thesis, University of Maryland.

Roberts, M. S. 1962a, *A.J.*, **67**, 437.

________. 1962b, *A.J.*, **67**, 431.

________. 1963, *Ann. Rev. Astr. Ap.*, **1**, 149.

________. 1966a, Ap.J., **144**, 639.

________. 1966b, in *Stars and Stellar Systems*, Vol. **9**, ed. A. and M. Sandage (Chicago: University of Chicago Press), in preparation.

________. 1966c, *Phys. Rev. Letts.*, **17**, 1203.

________. 1967, *Radio Astronomy and the Galactic System*, IAU Symposium No. 31 (New York: Academic Press), p. 189.

________. 1969, *A.J.*, **74**, 859.

________. 1970, *External Galaxies and Quasi-Stellar Objects*, IAU Symposium No. 44 (in press).

Roberts, W. W. 1969, *Ap.J.*, **158**, 123.

Roberts, W. W., and Yuan, C. 1970, *Ap.J.*, **161**, 887.

Rogstad, D. H. 1970, private communication.

________. 1971, *Astr. and Ap.*, **13**, 108.

Rogstad, D. H., and Shostak, G. S. 1971, *Astr. and Ap.*, **13**, 99.

Rubin, V. C., and Ford, W. K. 1970, *Ap.J.*, **159**, 379.

Sandage, A. 1961, *Hubble Atlas of Galaxies* (Washington, D.C.: Carnegie Institution of Washington).

Schmidt, M. 1965, in *Stars and Stellar System,* Vol. **5**, ed. A. Blaauw and M. Schmidt (Chicago: University of Chicago Press), p. 513.

Seielstad, G. A., and Whiteoak, J. B. 1965, *Ap.J.*, **142**, 616.

Shapley, H., and Ames, A. 1932, *Annals Astron. Obs. Harvard College*, **88**, No. 2.

Shklovsky, I. S. 1949, *A.J.* (U.S.S.R.), **26**, 10.

Shobbrook, R. R., and Robinson, B. J. 1967, *Austr. J. Phys.*, **20**, 131.

Shu, F. H., Stachnik, R. V., and Yost, J. C. 1971, *Ap.J.*, **166**, 465.

Slepian, D., and Pollak, H. O. 1961, *Bell Sys. Tech. Journal*, **40**, 43.

Spinrad, H. 1966, *Pub. A.S.P.*, **78**, 367.

Stebbins, J. and Kron, G. E. 1957, *Ap.J.*, **126**, 226.

Tammann, G. A., and Sandage, A. R. 1968, *Ap.J.*, **151**, 825.

________. 1971, in preparation.

Truran, J. W., and Cameron, A. G. W. 1970, *Nature*, **225**, 5234, 710.

Van Damme, K. J. 1966, *Austr. J. Phys.*, **19**, 687.

Vaucouleurs, G. de. 1958, *Ap.J.*, **128**, 465.

________. 1959, *Ap.J.*, **130**, 728.

________. 1960, *Ap.J.*, **131**, 574.

________. 1961, *Ap.J.*, **133**, 405.

________. 1964, *The Galaxy and the Magellanic Clouds*, IAU Symposium No. 20 (Canberra: Australian Academy of Science), p. 88.

________. 1970, *The Spiral Structure of Our Galaxy*, IAU Symposium No. 38 (New York: Springer-Verlag), p. 18.

Vaucouleurs, G. de, and Ables, H. 1965, *Pub. A.S.P.*, **77**, 272.

Vaucouleurs, G. de, and Vaucouleurs, A. de. 1963a, *Ap.J.*, **137**, 363.

________. 1963b, *A.J.*, **68**, 278.

________. 1964, *Reference Catalogue of Bright Galaxies* (Austin: University of Texas Press).

Veron, P., and Sauvayre, A. 1965, *Ann. d'Ap.*, **28**, 698.

Volders, L., and Hogbom, J. A. 1961, *B.A.N.*, **15**, 307.

Volders, L., and Hulst, H. C. van de. 1959, *Paris Symposium on Radio Astronomy*, IAU Symposium No. 9 (Stanford: Stanford University Press), p. 423.

Wade, C. M. 1970, *Ap.J.*, **162**, 381.

Weaver, H. F., and Williams, D. R. W. 1971, in preparation.

Weiler, K. W. 1969, Ph. D. Thesis, California Institute of Technology.

Weinreb, S. 1963, *M.I.T. Research Laboratory of Electronics Technical Report No. 412.*

Wright, M. C. H. 1971, *Ap.J.*, **166**, 455.

Wright, W. 1971, private communication.

Zwicky, F. 1964, *List of Supernovae Discovered Since 1885*, California Institute of Technology.